Multi-frequency Radio Continuum Observations of Nearby Spiral Galaxies : NGC 2997 and NGC 4565

A Thesis submitted for the degree of

Master of Science

(Partly by Papers and Partly by Research)

(In Physics)

to

UNIVERSITY OF PUNE

by

KODILKAR JITENDRA PRALHAD

Giant Metrewave Radio Telescope, khodad

National Center for Radio Astrophysics,

TIFR

Pune - 411007

November, 2005

Declaration

CERTIFIED that the work incorporated in this thesis entitled "Multi-frequency radio continuum observations of Nearby Spiral Galaxies : NGC 2997 and NGC 4565" submitted by Kodilkar J.P. was carried out by the candidate under my supervision. Such material as has been obtained from other sources has been duly acknowledged in the Thesis.

Kodilkar J.P.
Candidate

Sr. Prof. S. Ananthakrishnan
Thesis Supervisor

Place : Pune
Date : November 24th, 2005

ACKNOWLEDGEMENT

I feel that from the learning of interferometry techniques to observation and interpretation of data of nearby galaxies was quite a bit of a marathon for me which I could not have accomplished without the strong encouragement, kind support and guidance of Prof. S. Ananthakrishnan. Apart from our work, I learnt quite a lot from my guide, including how to write a scientific report in proper English. During this course of work, from the AIPS analysis to the final results, I got valuable guidance from Dr. Nimisha Kantharia who also supervised my work as a co-guide. I thank Prof. D.J.Sakia for his kind co-operation and guidance for giving me notes related to the spiral galaxies from the beginning of my course work. I would like to express my gratitud to Prof. Gopal- krishna who also checked the total intensity maps during his visits to the GMRT, and I learnt many useful things on the analysis during our discussions.

I would like to express my special gratitude to the Dean Prof. A.Pramesh Rao for his kind support during the course work. I also thank my reporting officer Shri. Suresh Sabhapati under whom I am executing my job at the GMRT. He always encouraged and supported all my aqctivities in my service period so that I could dedicate my service to the institute at my best level. I would like to thank Prof. Vasant Kulkarni who provided extensive computer facility to me and my colleagues. I thank Dr. Ramana Athreya who supervised our control-room work, I appreciate his kind support during my work-load of the thesis and my job. I must thank Shri. T.L.Venkata Subramani for allowing some of the observations for this dissertation during the Engineering test time.

It gives me immense pleasure to thank Dr. Sanjay Bhatanagar who is an inspiration for me and my colleagues in the field of software as well as in radio astronomy. I sincerely thank the Centre Director Prof. R.Nityananda; the *Synthesis Imaging School (June,2004)* conducted by him helped quite a lot for making further progress in my work. I thank the Chief Scientist Prof. Y. Gupta for his kind support during the course work. I would like to thank Sandeep Sirothia, Drs. Ishwar Chandra, Dipanjan Mitra and B.C. Joshi with whom I could discuss my doubts related to many aspects of radio astronomy.

My special thanks to all the NCRA graduate students, Chiranjib, Neeraj, Ayesha, Jayanta Roy, Nirupam and Anand. With them, I could freely discuss all aspects relating to my work and thesis. I would like to thank all my control-room colleagues (S/Shri. Aba, Mangesh, Sanjay, Jayprakash, Manish, Santaji, Deepak, Sachin and Ms.Manisha) for their kind co-operation. They helped me in so many different ways during all these years, especially during the leave period for my M.Sc. semester-examination. I would like to thank all my tea-table friends for creating such a cheerful environment in the GMRT.

Finally I am deeply indebted to my wife, Pallavi and daughter, Amruta for their understanding and tremendous support; I dedicate this report to them and my parents.

Abstract

This thesis is mainly organized in two parts. In the first half of the thesis, we have studied a radio interferometer, Fourier synthesis imaging and understanding of the interferometry techniques in practice by using the GMRT for continuum observations. We have mainly adressed the observational details using the GMRT, describing the instrument from a radio continuum observation point of view, data reduction procedure followed using the AIPS and the problems that occurred while imaging the low-surface brightness distribution of NGC 2997 and NGC 4565.
The assumptions made for Fourier inversion to get the brightness distribution in image domain from the sampled visibilities in spatial frequency domain are no longer valid at low frequencies; due to the bigger beam size the mapping field cannot be approximated as a 2-D tangent plane. Also, the number of strong confusing sources in a field are more, which limits the sensitivity of an image due to its incoherent side-lobe response. Therefore, while making the wide-field images of NGC 2997 and NGC 4565 at low frequencies, we have discussed the non-coplanarity problem, overview of possible solutions to this problem, and the implemented method to reduce the effect. Also, we have studied the CLEAN and MEM deconvolution algorithms and their implementation in AIPS by mapping NGC 4565 at 610 MHz with a resolution of 12 arcsec.

In the second part, we have presented the results of multi-frequency radio continuum observations of two nearby spiral galaxies NGC 2997 and NGC 4565 using the GMRT at three frequencies. This is the first time that NGC 2997 is being observed at low-frequencies i.e. 325, 610 and 1280 MHz. In the case of NGC 4565, higher resolution observations have been made at these frequencies for the first time. NGC 2997 and NGC 4565 are normal galaxies; in this work, we have described briefly, the theory related to spiral galaxies, radio emission in such galaxies and their radio continuum structure.

The maps of NGC 2997 made with the resolutions from $45''$ to $4''$ revealed many radio continuum features. We found that a central region of $0.5'$ shows a flat spectrum at low-frequencies. The radio continuum emission from the two spiral arms were detected clearly and the structure of the spiral arms show Sc classification. A gap is seen in all the total intensity maps of NGC 2997 in the north-western side of the southern arm. This gap is also seen in the VLA total intensity and polarized intensity maps at λ20 cm, λ18 cm, λ6 cm, and λ3 cm. (Han, 1999; H.Men & Han, 2005). Also, bifurcation feature of the southern-arm towards west into the third arm is seen in our total intensity maps.

We obtained the total intensity maps of NGC 4565 at each observing frequency with low-resolution (45 arcsec) as well as high-resolution (20 arcsec). Both the high resolution and low resolution maps of NGC 4565 at 325 MHz and 610 MHz show a

dip along the major axis − near the north-west side of the nucleus. The spectral index distribution between 325 MHz and 610 MHz along the major-axis using high resolution maps shows that dip has a flat spectrum value $\alpha \approx -0.5$.
The distribution of radio emission in the 325 MHz low-resolution map shows a prominent deviation from the principal plane at the north-west end of the galaxy. This kind of warp has also been observed at 1410 MHz of WSRT (E. Hummel et al., 1984).
The radio dimensions (FWHM) of NGC 4565 using the high resolution maps are found to be close to the radio dimensions (FWHM) measured at 1414 MHz (Broeils et al., 1985). Our high resolution maps at all the observed frequencies resolved the central extended source into three components reliably, for the first time.

We fitted a composite (thermal free-free plus synchrotron) as well as a single power law model to the total emission flux densities of NGC 2997 and NGC 4565 in the range of 10.5 GHz to 325 MHz. The best-fit value obtained for NGC 2997 from the single power-law model is $\alpha = -0.98 \pm 0.06$. In the case of NGC 4565, the composite spectra model is best fitted with the nonthermal spectral index $\alpha_{nt} = -1.19 \pm 0.16$. The derived thermal fraction for NGC 2997 at 1272, 616, and 332 MHz is 10.33%, 6.08% and 3.58%, repectively, of the observed total flux density value. The thermal fraction of 10.33% at 1272 MHz is found to be consistent with the upper limit set for the thermal fraction of normal spiral galaxies at 1.4 GHz (Condon, 1992). The derived thermal fraction value for NGC 2997 is found to be equal (of about 40 mJy) in all our three observing bands.
By fitting the composite spectral model to the NGC 4565 radio spectrum, we derived the thermal and nonthermal flux density, thermal fraction, and the ratio of thermal to synchrotron flux density at each frequency. The thermal fraction for NGC 4565 at 1.4 GHz was found to be around 0.14.

Assuming that the flux densities observed with the GMRT are of non-thermal origin, the derived non-thermal luminosities for NGC 2997 and NGC 4565 were used to estimate the supernovae rate (yr^{-1}), the average star-formation rate ($SFR(M \gtrsim 5M_{\odot})$ and the production rate of the Lyman continuum photons (s^{-1}). The radio supernova rate in NGC 4565 estimated by us is $0.016\, yr^{-1}$ which is close to the values for our Galaxy. Our data suggest that the radio supernova rate (ν_{SN}) in NGC 2997 is a factor of three to four times higher than that of our Galaxy. The estimated Lyman continuum photon production rate in NGC 4565 ($1.36 \times 10^{53}\, s^{-1}$) is 30% less than that of our Galaxy ($2 \times 10^{53}\, s^{-1}$). The derived star-formation rate in NGC 2997 and NGC 4565 suggest that these are normal galaxies with intermediate star-formation (SF) levels.

Contents

List of Figures

List of Tables

Chapter 1

Introduction

The Giant Metrewave Radio Telescope (GMRT) is the largest facility in the world for radio astronomical observation at a range of low frequencies from 150 MHz to 1.4 GHz. This versatile instrument has been set up 80 km north of Pune near Khodad village by the National Centre for Radio Astrophysics of the Tata Institute of Fundamental Research, India. The GMRT is being used on a regular basis for a variety of observations like continuum observation of galactic & extra-galactic objects which includes sun, supernova remnants, galactic center, HII regions, nearby galaxies and clusters of galaxies, spectral line observations to study the HI, OH lines at various redshifts & radio recombination lines and pulsar observations using incoherent and phased array mode.

The GMRT (Swarup et al., 1991, Ananthakrishnan and Rao, 2002) operates as an earth rotation aperture synthesis radio telescope consisting of thirty 45m diameter parabolic dishes spread in the shape of a 'Y', with fourteen antennas placed randomly in an area of size 1km $\times$ km known as *the central square*, and the remaining five to six antennas in the North-East, the North-West and the South direction, each of length $\sim$ 14km.

Due to the arc-second resolution from the long arms, adequate sensitivity to diffuse emission due to the closely spaced central square antennas and the multi-band observation capabilities at low frequencies, GMRT is a very powerful instrument to investigate various phenomena related to normal and active galaxies. Since, at the low frequency, non thermal synchrotron emission from the relativistic electrons becomes dominant than the thermal free-free emission from the ionized hydrogen regions in normal galaxies, GMRT observations can highlight many problems related to the study of large scale structure of radio emission from these galaxies. A combined spectral information obtained from the multi-frequency radio continuum observation can be useful for studing the total emission spectra, identification of the thermal and non-thermal contribution to the radio emission from the different regions of the galaxy, investigation of the physical mechanism responsible for the generation, propagation and the confinement of the cosmic ray electrons in the galaxy and the existence of radio haloes.

We have selected two nearby spiral galaxies NGC 2997 and NGC 4565 which are normal spiral galaxies (Condon J.J. 1987), one being face-on and the other, edge-on, respectively, for our study. At meter wavelengths, the radio emission from these

galaxies is relatively weak and has low surface brightness distribution; hence the statistical properties of radio emission as well as high resolution information are poorly known. We have done multi-frequency radio continuum observation of NGC 2997 and NGC 4565 using the GMRT at 325 MHz, 610 MHz and 1280 MHz. Before one can produce good quality maps of these objects, it is necessary to know the performance characteristic and the basic principles underlying the working of any radio telescope. Hence, we outline, firstly, the principles and practices of radio synthesis imaging in order to understand the difficulties associated with mapping at low frequencies. (Notes on Low Frequency Radio Astronomy in the NCRA, and the NRAO summer schools are very useful for this purpose. The principles of aperture synthesis and interferometry techniques are extensively dealt with, by Thompson, Swenson & Moran (1986)). Later, we summarise our observations. Subsequent chapters deal with the details.

1.1 Fourier synthesis imaging

A radio interferometer measures the spatial coherence function of the electric field due to the brightness distribution of the source in the sky. The spatial coherence function $V_\nu(r_1, r_2) = \langle E_\nu(r_1) E^*_\nu(r_2) \rangle$ is the simplest property of the quasi monochromatic components $E_\nu(r)$ of electric field at frequency ν and position r, which shows the correlation of the field at two different locations in the observing plane. The radio interferometer consists of two antennas with a correlator and an integrator, where the antennas convert the electric field into voltage signals and the correlator multiplies the two voltage signals after putting delays in the signal path so that the same portion of a plane wavefront of radiation field coming from the object can be measured. The final time averaged data output of the correlator is a complex quantity known as visibility.

Assuming the source is far enough away from the observing plane so that the incoming wavefront from the cosmic source can be considered as a plane wavefront, the signals received by the two antennas of the interferometer after correcting the delays are within the signal coherence time $\Delta\nu^{-1}$, and the radiation emanating from the different points on the source is incoherent. Under these assumptions, the van Cittert-Zernike theorem states that the spatial coherence of two points illuminated by a quasi-monochromatic source of incoherent radiation is related to the sky brightness as follows,

$$\mathbf{V}_\nu(r_1, r_2) = \int I_\nu(s)\ e^{\frac{-2\pi\, i\, \nu}{c}\, s\cdot(r_1 - r_2)} d\Omega \tag{1.1}$$

Here, the integral is taken over a source, s is a unit vector in the direction of the source, I(s) is the intensity, and $d\Omega$ is an element of solid angle.

As shown in the equation 1.1 the spatial coherence function depends only on the separation vector $r_1 - r_2$ and not on the absolute location. In practice, this vector spacing is called the baseline b which is nothing but the relative difference between the two antenna locations in the observing plane normal to the source direction. The length of the baseline can be measured in terms of the wavelength λ by introducing a special co-ordinate system (u, v, w), where u is towards east, v is towards north

and w is along the direction of phase tracking center s_0 with respect to which delays $\tau_g = b \cdot s_0/c$ are updated (see fig 1.1). The component of baseline vector is given by $r_1 - r_2 = c(u, v, w)/\nu$. If we consider a source of a small angular size lying on a tangent plane to a celestial sphere ($l^2 + m^2 + n^2 = 1$) at s_0, where l & m are direction cosines with respect to u & v axes, then the vector $s = s_0 + \sigma$ can be used to specify the direction to any point on the source, where $s_0 \cdot \sigma = 0$. In such a co-ordinate system, $s_0 = (0, 0, 1)$ and the components of s are $(l, m, 1)$. With these approximations, the eq.1.1 can be expressed in the following form.

Figure 1.1: Two element interferometer

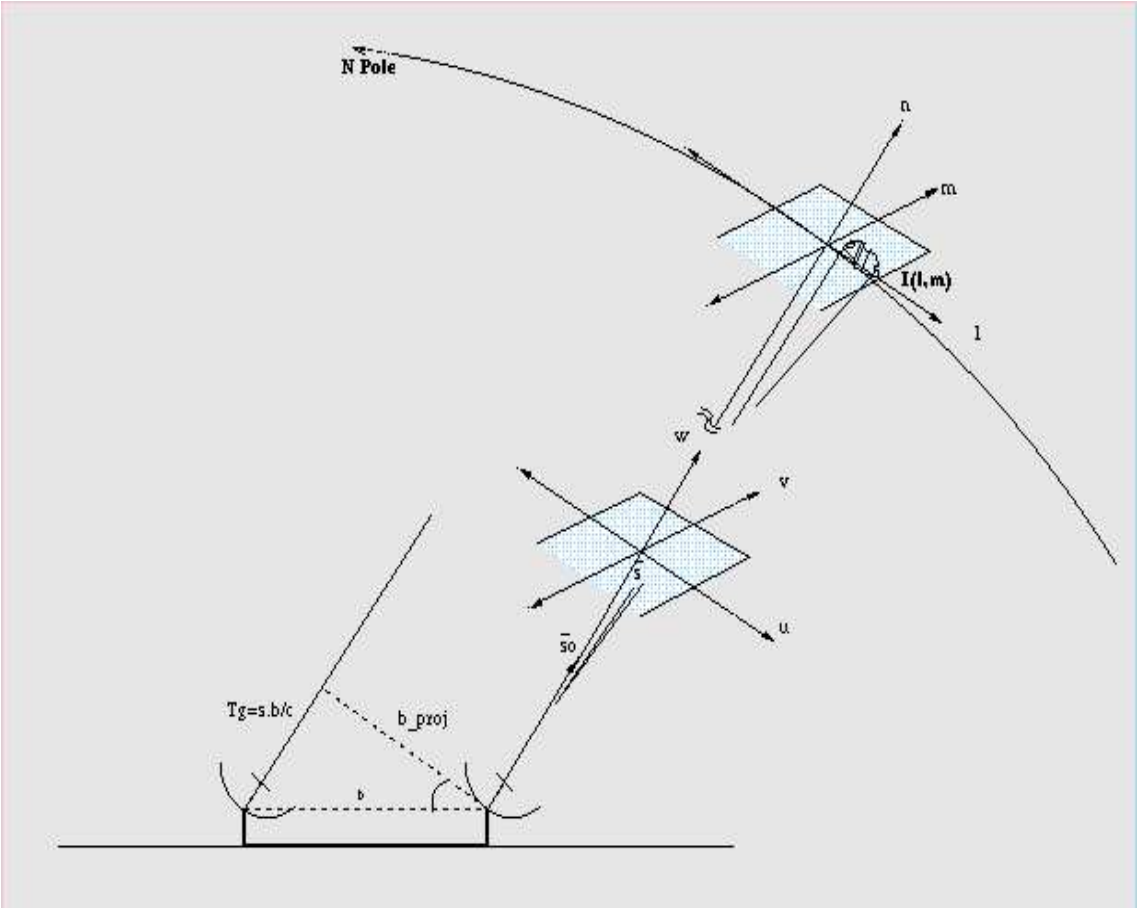

$$V_\nu(u, v, w) = e^{-2\pi i w} \int\int I_\nu(l, m)\, e^{-2\pi i(ul+vm)}\, dl\, dm \tag{1.2}$$

The above equation can be converted into a 2-D Fourier transform equation by absorbing the factor $e^{-2\pi w}$ into the left hand side term $V(u, v, w)$, then the equation 1.2 is independent of w-term.

$$V_\nu(u, v) = \int\int I_\nu(l, m)\, e^{-2\pi i(ul+vm)}\, dl\, dm \tag{1.3}$$

Thus, for a smaller field of view, the spatial coherence function measured instantaneously by a baseline is a Fourier component of the sky brightness distribution. The spatial frequencies u & v used to express the distances in wavelength depend on the hour angle of the source, so as the earth rotates, the projected separation between the antennas changes as viewed from the source. Therefore, we can use a finite number of antennas, forming the collection of two element intereromters, to measure the spatial coherence function (also known as the *visibility function*) at different u, v points at different times. Over a finite duration, using the earth's diurnal rotation, the visibility measurements made by tracking the source with this array of antennas sample the maximum (u, v) aperture plane tracing out portions of ellipses (called uv-coverage) , depending upon the declination of the source and the orientation of the antennas.
As the spectra of celestial objects for continuum radio observations do not vary, the use of *earth rotation* ensures a maximum number of Fourier components of the source brightness distribution over the required period to get a better uv-coverage, so that an image of good quality can be produced by *Fourier inversion* of the visibilities. This is known as the *earth rotation aperture synthesis*. As the variables u and v in Fourier space are conjugate variables of l and m which are used to describe the sky brightness distribution in the (l, m) plane, the image obtained by the Fourier inversion has the spatial resolution which varies inversely with the maximum baseline length for the measured visibility.
Since the spatial frequency plane (u, v) is not fully sampled by the finite number of antennas in an aperture synthesis array, the sampling function $S(u, v)$ which describes the set of measured visibilities, is zero for the unmeasured part of the (u, v) plane. Thus, the observed visibilities can be considered as the true visibilities multiplied by the sampling function; also, these visibilities are corrupted due to the receiver noise. Hence, by the *Fourier convolution theorem* the image obtained by Fourier inversion of the sampled visibility function is not the true image, but the convolution of the true image with the inverse Fourier transform of the sampling function.

$$I^d = \mathbf{F}^{-1}[V\,S] = I^{true} \star \mathbf{F}^{-1}[S(u, v)]$$

The resultant image I^d in radio astronomy is called the *dirty image*, and the Fourier transform of the sampling function is called the *dirty beam* or *synthesized beam* which constitutes a compact core and an increasing number of weak sibelobes.

1.1.1 Mapping

An image formation of the sky from the visibilities given by an interferometric array is an offline procedure called mapping. The observed visibilities by an interferometer are not the true visibilities corresponding to the Fourier transform of brightness distribution of the cosmic source, but these are affected due to disturbances across the signal path like the refraction of the signals at the low frequencies by the earth's ionosphere, receiver's complicated chain of electronic systems where the gains of array elements can be different and may vary with time due to instrumental & ionospheric effects. To correct these gain variations which are complex quantities, a strong point source or known source is observed at the phase center which is close to the target source, and the values of true visibilities (measured previously within some accuracy

) are known for such a *phase calibrator*. Since the ionosphere generally does not vary across the calibrator and the target source, the instrumental gain corrections determined from the true visibilities and the observed visibilities on the calibrator sources are applied to the target source. Similarly, the absolute flux of the target source can be determined by observing a point source of well known flux.

An image of the source can be obtained by inverse Fourier transforming the calibrated visibilities with the appropriate weight. The Fast Fourier Transform method used for this purpose requires the visibility data points at regular interval. For this purpose, the observed visibilities are interpolated on a regularly spaced grid. The *dirty image* obtained by Fourier inversion of the visibilities is sensitivity limited due to various reasons like deficiencies in sampling of (u, v) aperture plane by the synthesis array, inability to provide accurate calibrated data, and aliasing from the interpolation of visibility data on a regularly spaced rectangular grid.

The deconvolution to estimate the true sky brightness distribution involves locating the sources in the primary field, deconvolve them with the dirty beam and convolving them back with the Gaussian equivalent to synthesized beam to get rid of the sidelobes of strong confusing sources which sometimes obscure the weak and extended target sources.

Even after the ordinary calibration using the external calibrator sources, the visibilities on the target source has residual phase errors induced due to instrumental effects and ionospheric electron content fluctuation, which may vary rapidly with time or direction, degrading the quality of a final image. In the case of good signal to noise ratio, the self-calibration improves the model of the source iteratively by comparing the observed visibilities with the model visibilities obtained from an image guess of the object. In order to compute a set of antenna based amplitude and phase correction as a function of time, self-calibration uses the model visibility data to correct the observed visibilities so that they will be consistent with the iterative model.

The AIPS (*Astronomical Image Processing system*) is a portable software package by *National Radio Astronomy Observatory*, mainly used for the reduction and analysis of Radio Astronomy data.[1] AIPS is a vast collection of many independent programs which can display, edit and calibrate the radio interferometric data in the (u, v) plane, as well as perform all kinds of imaging tasks like the image construction by Fourier inversion, deconvolution and self-calibration. It has a variety of analytical tools and graphical displays which can be used for the analysis of the two and three dimensional radio astronomical images.

One of the **basic aims** of this thesis is to study the principle of a radio interferometer and understand the interferometry techniques in practice by using the GMRT for continuum observations, and learn the practical details of data reduction and mapping with the GMRT data using the AIPS.

We have tried to understand and study the frequency dependent properties and problems related to it while mapping at low frequencies like the size of the primary field of view, ionospheric effects on the visibility phases, and man made radio frequency interference in the band. The assumptions made for the Fourier inversion in the equa-

[1]More information on AIPS is available on Webpage "http://www.cv.nrao.edu/aips".

tion (1.3) are no longer valid at low frequencies due to the bigger beam size where the mapping field cannot be approximated as a 2-D tangent plane, and the number of strong confusing sources in the field are more, which limits the sensitivity of the map due to its sidelobes. Since ionospheric effects like refraction corrupt the visibility phases at low frequencies, an extensive application of self-calibration method is required to remove such effects. Further, radial smearing of the brightness in the image is prominent at low frequencies due to the averaging of larger bandwidth.
This thesis addresses the practical details of data reduction, calibration method and analysis used for the total intensity mapping. We have tried to explain the various tasks used in AIPS, their basic algorithms and strategies used for mapping objects with good fidelity, which involves Fourier inversion of the visibilities with appropriate weighting. We use image reconstruction methods like MEM and CLEAN and self-calibration to improve the dynamic range of the images. We have produced low resolution as well as high resolution maps of the objects at each frequency in order to study compact and diffuse emission. The array configuration for GMRT is made in 'Y' shape to maximize the UV-coverage, where the baselines are non-coplanar. In the case of wide field mapping, the non-coplanarity of the baselines results in phase errors due to the manifestation of the w-term (eq.1.2) which distorts the resultant image. Problems of this kind have been solved by 3-D imaging. All the low frequency specific problems given above are discussed and the required implementation to cope with it has been given in subsequent chapters.

1.2 Nearby galaxies : NGC 2997, NGC 4565

The local group of galaxies and the galaxies which are part of Virgo cluster (about 15-18 Mpc from us), or the galaxies which are not beyond 40 Mpc (systematic velocities less than 3000 km/sec) are considered as "Nearby" galaxies (Nearby galaxies catalog : Tully R.B.,1988). NGC 2997 and NGC 4565 are nearby galaxies which are $\sim$ 10 Mpc to 12 Mpc distance away from us.
A galaxy is a collection of stars, gas and dust along with associated starlight, magnetic fields and cosmic rays. This section and the subsequent sections give a brief introduction related to normal spiral galaxies, and focus the discussion on objectives of the radio continuum study of NGC 2997 and NGC 4565 using the GMRT.

1.2.1 Classification and morphological basic properties :

Edwin Hubble (1936) classified the galaxies into three main groups based on their visual appearance : ellipticals, spirals, and irregulars.
The ellipticals are smooth and are designated according to their apparent flattening [10 (1 − Minor-axis/Major-axis], round ellipticals are E0s and the flattest ellipticals are E7s. Ellipticals have much more random star motion than orderly rotational motion, a little dust and gas left between the stars, and mostly contain old type of stars.
The spirals are flat, as the name suggests, with a spiral pattern in their disk. Spiral galaxies harbouring bar structure at their central part are called "barred spirals"

(classified as "SB"), while normal spirals are simply classified as "SA" or "S", and mixed type are classified as "SAB or S(B)". On the basis of how loose their spiral arms are, spiral galaxies (normal and barred) are further subclassified into "a","b" and "c". The group of spiral galaxies classified as "Sa or SBa" have large bulges (at their centre) and have very tightly wound spiral arms; those which have prominent bulges and pronounced arms are classified "Sb or SBb", and those which are dominated by loosely wound spiral arms and small nuclear bulge are known as "Sc or SBc". Spiral structures with almost no bulge or core and very loose spiral arms are classified in "d" category. Spiral galaxies have more orderly, rotational motion than random motion, i.e. star orbits are closely confined to a narrow range of angles and fairly circular, along with lots of gas and dust between the stars; therefore new star formation occurs in these regions.

The group of Irregular galaxies in Hubble scheme have no definite structure. When undergoing a heavy interaction, or collision, with a massive neighbour, disk galaxies may be distorted very peculiarly, and then are often classified as irregular e.g. Messier irregular- M82. In irregular galaxies, the stars are bunched and randomly distributed throughout the galaxy. Most irregulars are small and faint.

The classification sequence from ellipticals to spirals represented in *tuning fork* diagram by Hubble was an evolutionary sequence according to him, with the top prong representing regular/normal spirals and bottom prong representing barred spirals ; but the present knowledge shows that it is not necessarily an evolutionary sequence since each type of galaxy has very old stars. Hubble expected evolutionary bridge of "S0" class galaxies between ellipticals to spirals which was added later by Allan Sandage, who expanded Hubble's work. The "S0" class of galaxies also called *lenticulars*, which are similar to spiral galaxies in shape and color, having large bulges, weak disks but no spiral structure. These are placed at the point in the tuning fork diagram where it brances off to the regular spiral or barred spiral pattern. The lenticular galaxies do not have gas and dust for some reason, e.g. S0 galaxies :NGC 1201 and M84.

The *dwarf galaxies* are numerically larger in the universe, the most common type is elliptical in shape and has little gas, known as dwarf elliptical (dE). The dwarf ellipticals lack a bright nuclear region. The other principal type of dwarf galaxies are the dwarf irregular (dIrr). The galaxies which do not fall into any of the classes mentioned above are known as *peculiar galaxies*.

Brightness limited samples of observed galaxies shows that 77% are spirals, 20% are ellipticals and 3% are irregular. A survey of the region of space out to 9.1 Mpc shows that only 33% of the galaxies in this volume are spirals, 13% are ellipticals, and 54% are irregulars. The basic properties of galaxies are given in the table (1.1).

All disk galaxies have a very different appearance, depending on their inclination angle toward the line of sight. If we view the disk galaxies from their edge (or "edge-on"), or from near their equatorial plane, they appear thin, flat, linear and elongated patches often with dusty structures along their equators (e.g. NGC 4565). The disk galaxies seen almost from their poles so that we can see their disks called "face-on" (e.g. NGC 2997).

Morphology of spiral galaxy :

External spiral galaxies in the universe show the same features as the Milky way. Spiral galaxies consist of mainly three spatially and dynamically distinct components: disk, bulge and haloes. There are two visible prime constituents of galaxies : stars, and interstellar medium consisting of dust & gas. The schematic diagrams of "face-on" and "edge-on" normal spiral galaxies are shown in fig.1.2

Disk : Spiral galaxies have flattened disk, often shows conspicious spiral structure with central ellipsoidal bulge and/or luminous bar structure at the central part of the disk. The structure-wise classification of spiral galaxies in "normal" and "barred" spirals is considered as the consequence of gravitational interactions with neighbouring galaxies, the interactions with neighbours cause inhomogeneties and unsymmetries of gravitaional field within the disk, which tends to compress the gas in some regions. If the density of the gas in these regions exceeds a certain critical value (which depends on parameters such as temperature), star formation can take place, resulting in the formation of red diffuse nebulae and blue clusters of hot young stars which slowly change their color to yellow at the end of their age when they completely consume the hydrogen fuel inside the core.

A lot of interstellar matter (reddish diffuse emission nebulae or as dark dusty clouds) and most of the young massive star clusters are arranged in spiral arms, having orderly rotational motion (in the same direction) within the disk. As per Hubble's sequence, "a" type of spirals have tightly wound spiral arms, and "c" type have loosely wound

Table 1.1: Basic properties of galaxies

	Elliptical (E)	Spiral (SA/SB)	Irregular(Irr)
1. Morphological Structure	Round or elliptical shapes Spherical(E0) to highly flattened(E7)	Flattened disk with spiral spiral structure.Divided into barred(SB) and unbarred(S).	No symmetrical or regular structure.
2. Population content	Type II and Old type I star. Very little dust & gas, so no new star-formation. Random star motion.	Type I in arms, II and old I overall. Copious amount of dust and gas between star New star formation occurs in spiral arm.More orderly star motion.	Type I and some type II. Higher proportionality of dust and gas than spirals.
3. Diameter(kpc)	1 to 200	5 to 50	1 to 10
4. Spectral type	K	A,F,G,K	A to F
5. Mass ($M_\odot$)	10^5 to 10^{13} $M_\odot$	10^9 to 10^{11} $M_\odot$	10^8 to10^{10} $M_\odot$
6. Luminosity ($L_\odot$)	3×10^5 to 10^{11}	10^8 to 2×10^{10}	10^7 to 10^8
7. Location	Mostly in clusters.	Mostly in Field.	Field
8. examples	M32,M110 satellite galaxies of Andromeda, M87-huge elliptical at the center of Virgo cluster.	Andromeda galaxy (M31-Sb), M81(Sb), NGC 3351 (SBb), and NGC 2997 (Sc).	LMC,SMC : satellite of Milky way, M82, IC5152- a dwarf irregular galaxy in local group.

Figure 1.2: Rough schematics of normal spiral galaxies

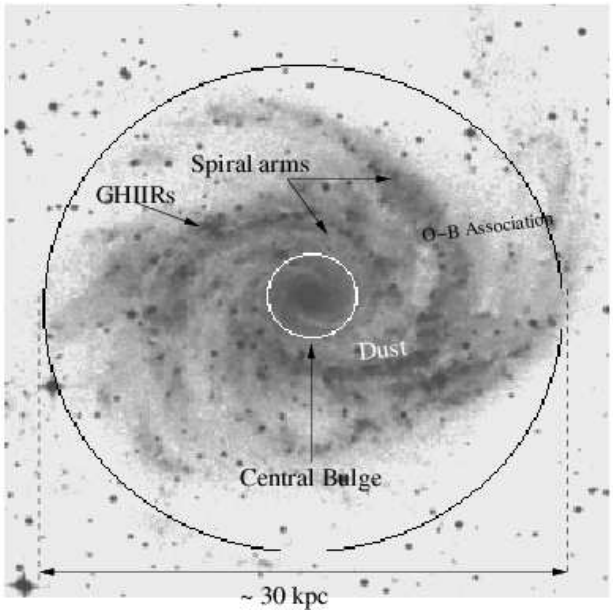

fig 1a. Face-on appearance

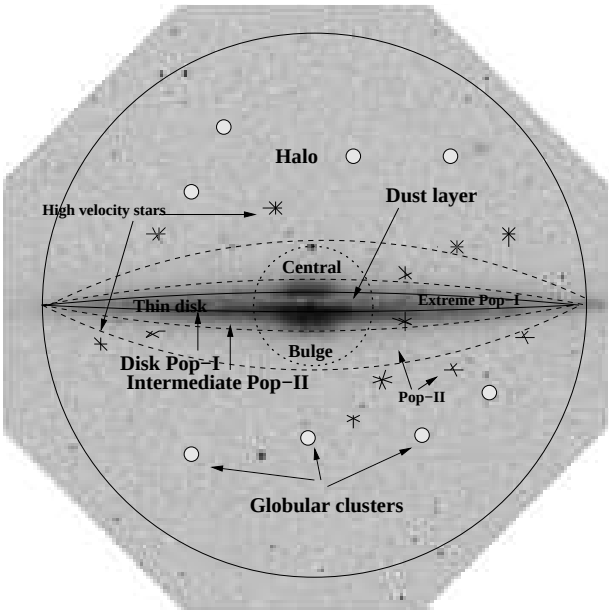

fig 1b. Edge-on appearance

spiral arms. Therefore, conventionally, the "a" class of spiral galaxies are known as *early-type*, and the "c" class of spiral galaxies are considered as *late-type* of galaxies.
spiral structure : The correlated elliptical orbits of stars along with the matter compress the gas, dust and stars, where the spiral density wave gets created in greater gravity. The density enhancement in spiral arms triggers the star formation, creation of O & B type young massive stars, and HII regions which enhance the spiral outline. The magnetic field gets compressed in high-density regions which shows its appearance in radio continuum emission, and hence supports the spiral density wave theory. The shock-waves created by supernovae, when the massive stars die, keeps the spiral-arms visible.
Bulge : An ellipsoidal bulge component at the center of the disk consisting of an old stellar population (known as Pop-II stars) without interstellar matter. The near-infrared image of our Galaxy shows the central nucleus surrounded by a stellar condensation with a 1.5 kpc bulge radius and ∼0.7 kpc height, and containt very little gas and dust. The spiral arms emerge from this condensation.
Population of stars : Walter Baade(1944) classified the stars into two basic groups: Pop-I stars are brightest young blue, metal-rich stars, and the Pop-II old, red-giants, metal-poor stars. Stars occur both in clusters as well as isolated field; the field stars follow the same distribution as the star clusters. The different stellar populations in the Milky way differ in location, kinematics, age and metallicity.
Population I : Pop-I stars have a wide range of ages from ∼0.1 to 10 billion years, which are confined to a flat rotating disk system within radius of ∼ 20 kpc. These tend to be rich in heavier elements (Fe,Si,etc.). The oldest Pop-I stars are found at 1 kpc above the disk plane (thick disk), and follow slightly elliptical orbits, the metalic-

ity is ~ 0.3 times that of the sun. The metalicity of 0.5 to 1 times sun in middle-aged stars (G,K & M dwarfs) forms the thin disk, and they are found at a scale height of 350 pc above the disk plane. The abundance of metals 1-2 times than sun in young stars are found in spiral arms with a scale height 200 pc above the disk plane, and youngest stars (O-stars) less than 100 million year in age (Metalicity 1-2.5 times than sun) are found in spirals arms at ~ 100 pc above the disk plane. Young stars located at less than 350 pc above the disk plane follows the circular or near-circular orbit.
Population II : Pop-II are red-dim stars, 10 to 12 billion years old, found in spheroidal component (halo, bulge) of the galaxy. Pop-II stars in haloes ($\sim$3-5 kpc radius) have spherical distributions, and follow very elliptical, uncorrelated orbits. They tend to be much poorer in heavy elements than the disk stars. The stars having abundance of metals less than 0.1 times that of the sun, are found in the outer stellar halo. The metal abundance rises as one goes inward toward the Galactic center; the metal content rises 1-3 times that of the sun in the bulge.
Globular cluster : Globular star clusters, large but quite compact group of some 100,000 to several million stars. These large clusters have about the same mass as the smallest galaxies, and are among the oldest objects in the galaxies. Often, they form conspicuous systems, and occur in galaxies of every type and size. Since globular clusters are the oldest known objects in the Galaxy, it seems likely that the Milky Way formed $\sim 1.2 \times 10^{10}$ years ago.
Interstellar Medium (ISM): The ISM comprises only 1 to 3% of the total mass

Table 1.2: Phases of the Galactic ISM : Multi-wavelength observation

ISM Component	Observing technique	Approx. Temp.(K)	Density (atoms/cm^3)	Description
Molecular medium(MM)	CO, Sio emission etc.	30-60	300 to 10^4	Star-forming clouds.
Cold neutral medium (CNM)	HI-absorption against background continuum sources	100	100	Associated with the molecular gas existing in compact cloud. Regions of star-formation.
Warm neutral medium (WNM)	HI line emission(21cm)	3000	1	Radially most extended component in galaxy disk.
Warm ionized medium(WIM)	Optical emission lines: H_α, [NII],[OIII]. thermal radio emission, recombination lines obs	10^4	0.3	Dominant gas phase in HII regions, the more extended part of the WIM outside HII regions is called - diffuse ionized gas (DIG).
Hot ionized medium(HIM)	X-ray imaging,and spectroscopy	10^6	0.01	Pockets of gas heated by supernova shock-waves.

of a Galaxy ($\sim 10^{11} M_\odot$). About 99% of the material of ISM is gas, and the remaining is dust. The ISM has mainly two reservoirs of gas and dust: atomic gas - mainly HI atoms which can be seen in the 21 cm line, and molecular gas - mainly H_2 molecules which are traced by CO molecules (since H2 is difficult to detect). The multi-wavelength observation data of ISM shows the different phases of the Galactic ISM via various radiation mechanisms, in both line and continuum emission. A brief

Table 1.3: Basic data

	NGC 2997	NGC 4565
Optical Center	9h45m39.4s -31d11′28″	12h36m20.8s +25d59′16″
Morphological type	SA(s)c	SA(s)b
Optical Major & Minor axis(arcmin)	8.9 x 6.8	15.9 x 1.85
Distance ($H_0 = 75 km\, s^{-1} Mpc^{-1}$)	12 Mpc	10.2 Mpc
Magnitude(Visual Brightness)	10.06	10.42
Inclination angle (deg.)	40	86
Heliocentric radial velocity (km/s)	1087 ± 4	1282 ± 1

Ref. NED Database

description of ISM phases given in table 1.2 is based on the description given by Michael Dahlem(1997).
The more general view on Galactic ISM given by Dahlem(1997), includes three more components in addition to five gas phases described in table 1.2 : interstellar dust, comsic rays(CRs), and magnetic fields.
Dust : Our galaxy contains $\sim 10^7 M_\odot$ of dust (Temperature ∼20k), and mostly found concentrated in a very thin layer (100 pc thick) in the galactic plane. The absorption features seen in distant stars shows that ∼200 nm due to $C_8H_8N_2$ or graphite, 3.08 micron absorption features are due to ice particles, and 9.7 micron absoprtion features are due to sillicates. The dust grain reprocesses this absorbed radiation/ionizing stellar UV-radiation, and emits it in the far infrared (FIR).
Cosmic rays & magnetic fields : The relativistic particles, i.e. protons, electrons and atomic nuclei are called as Cosmic-rays (CRs), which forms an ionized plasma of highly energetic particles. The supernovae (SNe) and supernova remnants (SNRs) are the two prime sources of cosmic rays. When the SNRs interact with the ambient ISM, strong magnetic fields are created in it, and together with the CRs, these fields can spread over the large distances, creating large-scale B-fields. The Galactic field strength B is $\sim$ 3-6 μG. Synchrotron radiation from ultra-relativistic electrons dominates the radio continuum emission from most of the normal galaxies which is easily obeservable below $\nu \sim 30$ GHz. The ISM in the haloes of a spiral galaxy has complex nature similar to ISM in the disk. The morphology of the haloes and its existence mostly depend on the local level of star formation in the underlying disk. The energy sources creating and maintaining gaseous haloes are massive stars, their winds, and subsequent SNe in the galaxy disks.

1.2.2 Basic data

Basic data on NGC 2997 and NGC 4565 are given table 1.3.
NGC 2997 : This is a grand design type, *face-on* SA(c), southern spiral galaxy in Antilla, which is inclined at 40 degrees to our line of sight. The optical map and data show that a small bright nucleus exists with hot spots, and two tightly wound spiral arms originate from the bright nucleus which extends to cover the outer disk, see fig

1.2. The central red core has older stars and is in a quiescent phase (no emission-line activity). Many HII regions exist in the high-surface-brightness luminous arms.
NGC 2997 is an example of a "hot spot" galaxy (Meaburn & Terrett 1982) with a number of UV luminous knots near the center, which are massive star clusters, Maoz et al.(1996) further investigated the central region of NGC 2997 using HST, and concluded that, the clusters in the center of NGC 2997 will eventually evolve into objects resembling globular clusters. S.S. Larsen & T. Richtler 1999 found massive clusters also outside the center.
NGC 4565 : NGC 4565 is large, and considerably bright almost edge on galaxy (inclination: 86d) at a distance of 10.2 Mpc in Coma Berenices. This galaxy is of the same Hubble type as our Galaxy (Sb). In the optical map, there is a prominent dust lane near the bulge which is running across the entire length of the galaxy. The extent of easily visible optical emission along its major axis is about 20% more on the NW than the SE side. This galaxy shows nuclear bulge which supports the evidence of a spheroidal component.

1.2.3 Normal Vs active galaxies

The galaxies which do not contain a supermassive black-hole (10^6-$10^9 M_\odot$) or the large scale radio structure associated with bright nuclei, like haloes, jets or lobes are considered as *normal galaxies*. Syfert galaxies, radio galaxies, and QSOs (Quasi-Stellar Objects) fall in the category of *active galaxies*. The normal galaxies have luminosities less than or equal to ten times the luminosity of Milky Way ($L_{MW} = 2 \times 10^{10}\ L_{sun}$), whereas the active galaxies can have luminosities from the range of 0.5-50 L_{MW} for syfert and radio galaxies, and for the quasars, it has even higher luminosities ranging from 100-5000 times than that of the Milky Way luminosity. At 1.4 GHz, normal galaxies range in power from $L \lesssim 10^{18} h^{-2} W/Hz$ to $L \sim 10^{23} h^{-2} W/Hz$, where $h \equiv H_0/(100 km\, s^{-1} Mpc^{-1})$. Luminosity of both the normal galaxies, NGC 2997 and NGC 4565, at 1.49 GHz is around $\sim 8 \times 10^{21} W/Hz$ (Condon J.J, 1987).
Syfert galaxies are very hot ($> 10^8$ K), rapidly rotating disks ($\sim$1000 km/s), show very bright compact nuclei; nearly all emission comes from the compact central region ($<$ 1 lyr across). These are 10^4 times brighter than the center of our galaxy. Syfert galaxies look much same as the normal galaxies in the optical band, but they emit more energy in IR and radio parts of the spectrum. Radio galaxies are very bright in radio regime, show most emission from a very small core ($\lesssim$ 1 pc) with haloes and jets or extended lobes asscoiated with it, whoes emission extends up to hundreds of kpc, eg. M87, Cygnus and NGC 6251. QSOs are galaxies with extremely luminous emission and are the most distant objects in the universe. They look like stars and within a region of only $\sim$ 1pc size, they are 100 to 5000 times luminous than the milky way. Qusars (quasi-stellar radio sources) are a subset of QSOs which are strong radio emitters.
Galaxies showing simillar properties like Hubble type, total mass and maximum rotation etc., may be completely different in various other parameters, such as current star formation rate (SFR). The SFR for the galaxies can vary from zero to few tens $M_\odot yr^{-1}$. The galaxies not having current star formation are found to have old stel-

lar population only, whereas, galaxies having the higher rate of star formation are referred to as *starburst* galaxies, which have *Pop-I* type of star (Hot, young massive O & A type). The higher star formation rate of the order of $\gtrsim 50 M_{\odot} yr^{-1}$ in starburst galaxies (e.g. M82) cannot be maintained over a Hubble time, implying that it must be a transient phenomenon. The galaxies which have intermediate level of star formation are called as *normal galaxies* (Dahlem,1997). Our Galaxy and M31 are normal galaxies, the SFR of the Milky Way is of the order of $\simeq 3 M_{\odot} yr^{-1}$. The gas consumption in normal galaxies is too low to exhaust the gas supply in less than the Hubble time, which leads to the coexistence of different stellar populations, with a range of different ages and hence colors.

1.3 Radio emission from normal galaxies

The radio sources powered by monsters in active galactic nuclei (AGNs) are different from the *normal galaxies* on the basis of radio morphology, FIR spectral index $\alpha(25\mu m, 60\mu m) < 1.5$ and FIR/radio flux density ratios (Condon, 1992). Hence, the FIR- and radio-selected samples of *normal galaxies* (Condon & Broderick 1986,1991) also favor luminous starbursts galaxies and contain a large proprtion of disturbed, peculiar, and interacting systems.

Excellent review given by Condon J.J.(1992) describes the aspects of radio emission

Figure 1.3: The observed radio/FIR spectrum of M82 (Klein et al. 1988, Carlstrom & Kronberg 1991, Condon, 1992)

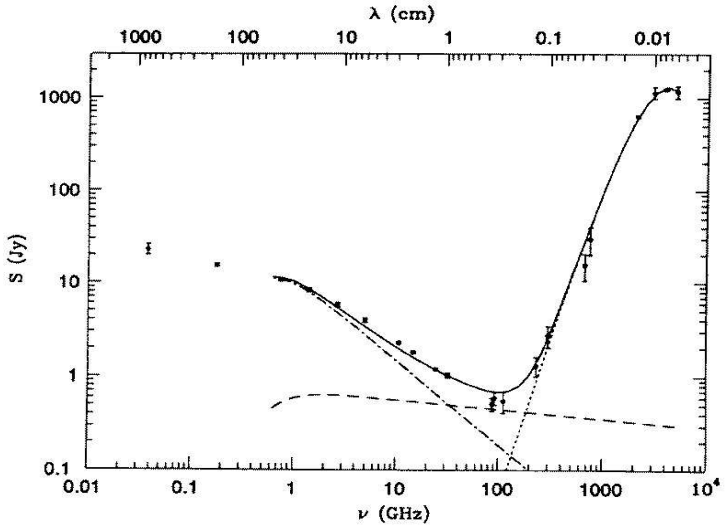

from normal galaxies and relates its study to recent star-formation activity in normal galaxies. A brief description in this section, and next subsequent sub-sections is given in view of the understanding of the radio continuum emission from the normal galaxies, which is mainly followed from the same review.

Most of the radio emission from normal galaxies is synchrotron radiation by the relativisitc electrons, and free-free thermal emission from the HII regions. The SNRs

of type-I and Type-Ib supernovae produced by the massive stars ($M \gtrsim 8M_{\odot}$), are thought to accelerate the relativistic electrons, and the uv-radiations from these massive stars also ionizes the surrounding neutral hydrogen regions, causing thermal free-free emission, the intensity of which depends on the production rate of Lyman continuum photons or uv photons. Such massive stars live $\lesssim 3 \times 10^7$ yrs, and the probable life time of the relativistic electrons is $\lesssim 10^8$ yrs and hence the radio emission from normal galaxies is not overwhelmed by stellar population older than about 10^8yr, tracing very recent star-formation activity in normal galaxies.
The thermal re-radiation from dust (T $\sim$ 45 K) is prominent in FIR regime, above 200 GHz. The free-free emission component is largest only in the range of 30 GHz to 200 GHz frequency range, shows flat-spectrum ($\alpha \sim +0.1$, where the spectral index α is defined by $S \propto \nu^{\alpha}$, S being the flux density and ν frequency). The free-free emission is usually weaker than the steep-spectrum ($\alpha \sim +0.8$) synchrotron emission below 30 GHz, and becomes opaque near $\nu \sim 1$ GHz, reducing both the free-free and synchrotron flux densities. Hence, isolating the free-free component and measuring its flux densities is difficult. The depicted radio/FIR spectrum of M82 in figure 1.3 is from J.J. Condon's review (1992) which shows the sum (solid-line) of synchrotron (dot-dash line), free-free (dashed-line), and dust (dotted-line) components.
The observed synchrotron radiation is from the older relativistic electrons ($\gtrsim 10^7$yr), that have propogated significant distance ($\gtrsim 1$ kpc) from their short-lived ($\sim 10^5$yr) and now defunct parent SNRs. Therefore, the original sources of relativistic electrons may have disappeared or their spatial distribution could have been smoothed beyond recognition, which makes it difficult to study the observed synchrotron spectra and the brightness distribution.
Unlike optical wavelength, the radio and FIR wavelengths are not obscured by dust, and hence most transperent to starburst; therefore, the observed flux densites are accurately proportional to intrinsic luminosities of the region. The FIR luminosity measures the bolometric luminosity produced by fairly massive ($M \gtrsim 5M_{sun}$) young stars, and the radio continuum account for $< 10^{-4}$ bolometric luminosity of normal galaxy. The ubiquitous correlation found between the global FIR and radio luminosities of normal galaxies suggest the one parameter model specifying the FIR and radio luminosities in terms of recent *star-formation rate*, which can describe most normal galaxies.

1.3.1 Thermal emission

In the classical theory, the free electrons radiate electromagnetic energy during the acceleration when it is influenced by the proton and gets deflected, which corresponds to the transition between different kinetic energies or different velocities. The interaction is termed a *free-free* transition since the electron is free or unbound, before and after the interaction with stationary protons (greater mass than electron). The interstellar gas mostly contain hydrogen atoms, the free electrons are found in this medium, as they are getting detached from atoms due to collision of atoms at the very highest temperature or through the action of UV or X-rays emitted by the hot young stars.

The free-free absorption coefficient $\kappa(\nu)$ of HII region is well approximated by :

$$\frac{\kappa(\nu)}{pc^{-1}} \sim 3.3 \times 10^{-7} \left(\frac{n_e}{cm^{-3}}\right)^2 \left(\frac{T_e}{10^4 K}\right)^{-1.35} \left(\frac{\nu}{GHz}\right)^{-2.1} \tag{1.4}$$

Where, n_e is the electron density, T_e is the electron temperature, and ν is the radio frequency expressed in the units indicated in above equation. The optical depth/opacity τ is given by integral of $\kappa(\nu)$ over the abosorbing path $\tau = \int \kappa(\nu) dl$, and is generally expressed in *emission measure* EM=$\int n_e^2 dl$ ($cm^{-6}pc$).
The observed brightness temperature (T_b) of ionized hydrogen cloud is :

$$T_b = T_e(1 - e^{-\tau})$$

At high frequencies (10 cm), the optical depth is $\tau \ll 1$, so that above equation gets reduced to $T_b = T_e\tau$, and assuming the uniform brightness over a source of extent Ω_s, the flux density S is defined as :

$$S = \frac{2kT_b\nu^2}{c^2}\Omega_s \tag{1.5}$$

Where, k=Boltzmann's const, Ω_s is the angular extent of source, T_b is source electron temperature.
Since, $S \propto T_b\nu^2$, $T_b \approx T_e\tau$ at high frequencies, and $\tau \propto \nu^{-2.1}$, the flux density $S \propto \nu^{-0.1}$. Thus, it follows that the flux density should be nearly constant at high frequency. Whereas, at low frequencies, the optical depth is large compared to unity, and therefore $T_b = T_e$, and hence the flux density $S \propto \nu^2$. As the flux density (S) is directly proportional to ν^2 like thermal black-body radiator, hence, at low frequencies it is termed as *thermal emission*. At sufficiently high frequencies ($\tau \ll 1$), the thermal spectral luminosity L_T of an HII region photoionized by hot stars is proportional to the production rate N_{UV} (per second) of Lyman continuum photons and varies only weakly with T_e, see the details in Condon's review (1992).
If the total flux density of galaxy is entirely due to steep spectrum ($\alpha \sim 0.8$) −synchrotron radiation and flat spectrum ($\alpha \sim 0.1$)−thermal emission from photoionized gas, then the relative contributions of these two forms of radiation should be distinguishable from the observed radio spectrum of the total emission. Klein & Emerson (1981) measured the integrated flux densities for small sample of nearby galaxies at 10.7 GHz, they determined the thermal flux density (S_T) by extrapolating the steepest power-law fit for flux densities measured at lower frequencies to 10.7 GHz, and subtracted it from the observed flux densities to remove the dominant non-thermal component. They set the upper limits for thermal fraction $S_T/S \lesssim 0.4$ at 10.7 GHz. Simillar results were obtained by Gioia et al.(1982) using the data of large samples of normal spiral galaxies at 10.7 GHz with 408 MHz and 4.9 GHz known flux densities.
The observed ratios of $S_{1.4GHz}/F(H_\alpha)$ for normal disk galaxies (Kennicutt,1983), and FIR/radio correlation study for normal galaxies (Condon & Yin,1990) provides an independent constraint on the average thermal fraction of normal galaxies, which puts the upper limit for thermal fraction $\langle S_T/S \rangle \lesssim 0.1$ at $\nu \sim 1.4$GHz. The estimated global thermal fraction for most normal galaxies at higher frequencies (opacity $\tau \ll 1$)

approximated by (Condon & Yin,1990) is :

$$\frac{S}{S_T} \sim 1 + 10 \left(\frac{\nu}{GHz}\right)^{0.1-\alpha} \tag{1.6}$$

Where $\alpha \sim 0.8$ is a typical nonthermal spectral index, S is total flux density and S_T is thermal component.
Radio brightness-tempearature spectra of normal galaxies containing mixed thermal and nonthermal sources depend upon the free-free abosorption coefficient $k(\nu)$. In the limit $(1-e^{-\tau}) \rightarrow 1$ at GHz frequencies, the maximum brightness temperatures of normal galaxies are $T_b \lesssim 10^5$K for $\nu \gtrsim 1$GHz. At low frequencies, many normal spiral galaxies with only moderate surface brightness temperature appear to be flattened slightly in the range 0.1-1 GHz because of the free-free absorption by very cool ($T_e <$ 1000 K) ionized gas filling a farily large fraction of radio emitting volume (Israel& Manoney,1990). Brightness of disk emission at $\sim$ 1.4 GHz vary considerably for normal galaxies ($0.1 < T_b \lesssim 10$ K, van der kruit,1978), the median face-on disk surface brightness of nearby spiral galaxies is $\langle T_b \rangle = 0.75 \pm 0.25$K at $\nu = 1.4$GHz (Hummel,1981).

1.3.2 Synchrotron emission

The frequency of maximum radiation (power per unit bandwidth) from the relativistic electrons with energy E moving at pitch angle θ in the magnetic field of strength B is given by critical frequency :

$$\left(\frac{\nu_c}{GHz}\right) \sim 0.016 \left(\frac{B\,sin(\theta)}{\mu G}\right) \left(\frac{E}{GeV}\right)^2 \tag{1.7}$$

For a typical spiral disk field strength $B \sim 5\mu G$, synchrotron emission in the frequency range of 0.1-10 GHz (100:1) is generated by electrons in the energy range 1-10 GeV (10:1). In practice there are always a large number of electrons participating in the radiation; and their energies; so their frequencies of maximum emission are rather spread out.
Kiepenheuer (1950) suggested that the electrons are in fact the electron components of cosmic rays and that the radiation occurs during their interaction with interstellar magnetic fields. An energy distribution characteristic of primary cosmic rays would appear to be appropriate for an ensemble of relativistic electrons with isotropic velocity distribution. It is assumed that the number of electrons is inversely proportional to a certain power γ of their energy, hence their energy spectrum is described by $N(E) = (const.)E^{-\gamma}$, where $N(E)$ is number of electrons as function of energy, E is energy of electron, and γ is energy-spectrum index. It can be shown that synchrotron emission coefficient due to such an assemblage of relativistic electron is :

$$\epsilon \propto \nu^{-(\gamma-1)/2} (B\,sin(\phi))^{(\gamma+1)/2}, \tag{1.8}$$

where ϕ is the angle between the magnetic field and the line of sight to the observer. The radiation from the relativistic electron of energy E is confined to a beam of

width $\Delta\phi \propto m_e c^2/E \ll 1$ radian parallel to the direction of instantaneous velocity of electron. The detector will detect pulses from those electrons whose velocity vectors nearly cross the detector's line of sight, therefore only the component of magnetic field pependicular to the electron path contributes to the observed radiation. Thus, eq.(1.8) indicates that the observed brightness of source depends on the direction of any ordered field component, even though the electrons are moving isotropically. If the z-component of magnetic field (perpendicular to equitorial plane of galaxy) is significant in the haloes of disk galaxies, synchrotron haloes may appear brightest in the edge-on system, and faintest in the face-on system.

For comsic-rays the approximate value for energy spectral index $\gamma = 2.4$, accordingly, a radio source with such cosmic-ray distribution should have a flux density variation with frequency $S \propto \nu^{-(2.4-1)/2} \propto \nu^{-0.7}$, and the brightness temperature of a region of synchrotron emission is proportional to $\nu^{-2.7}$. Therefore, the brightness temperature increases more rapidly with wavelengths than in the case of thermal emission of an ionized medium. Synchrotron self-absorption is only important for sources with brightness temperature $T_b > m_e c^2/k \sim 10^{10}$ K, which is never attained by normal galaxies. The spectral index of the nonthermal emission from a normal galaxy is usually $\alpha \sim 0.8$ at GHz frequencies, implying $\gamma = 2.6$ GeV energies.

Magnetic field : The total magnetic field strength in a galaxy can be estimated from the nonthermal radio emission under the assumption of energy equipartition ($U_m = U_p$) between the magnetic energy density (U_m) and the relativistic particle energy density (U_p). The total intensity of synchrotron emission gives the strength of total magnetic field. The median face-on brightness temperature ($T_b = S_N c^2/(2k\nu^2\Omega)$, where S_N is the nonthermal emission flux density) is $\sim$ 1 K at $\nu = 1.5\,GHz$, so most normal spiral disks are characterized by field strengths in the range $5 - 10\,\mu G$ (Sofue et al, 1986, Hummel et al, 1988). The intrinsic degree of linear polarization for optically thin synchrotron radiation from a power-law distribution of relativistic electrons in a vacuum is $\Pi = (\gamma + 1)/(\gamma + 7/3)$. However, the observed polarization vector suffers Faraday rotation and depolarization (i.e. a decrease of the degree of linear polarization when compared to the intrisic one) along the line of sight, and due to random orientations of the magnetic field vectors within the beam of the telescope. The intrinsic position angle of E is perpendicular to the projection of B onto the sky, the observed postion angle can be corrected for Faraday rotation, which is approximately proportional to λ^2 multiplied by the rotation measure $RM \equiv \int n_e B_\parallel dl$, where $B_\parallel$ is the magnetifc field component parallel to the line of sight.

Disk magnetic fields are generally more regular in areas of low star formation (the outer disk and interarm regions) and more turbulent where the star formation rate is high (spiral arms with large HII regions or molecular clouds, and near the nucleus). High resolution maps made at two or more short wavelength ($\lambda \lesssim 20$cm) show that large-scale disk magnetic fields of spiral galaxies normally run almost parallel to the spiral arms. In the case of edge-on system, like NGC 891 (Allen & Sukumar, 1991) magnetic field has been found to be mainly parallel to the disk, but the field lines in the extended radio halo NGC 4631 (Hummel, 1991a) point radially outward.

Cosmic-ray sources : The type II and type Ib SNRs of short-lived (3×10^7 yrs), massive ($M \gtrsim 8M_\odot$) stars are considered as the compact synchrotron sources and the

leading accelerators of cosmic rays, since the power source appears to be supenova shock− that propagates into the dense circumstellar wind or HII region produced by the supergiant progenitor star before it exploded. Cosmic rays in our Galaxy have total energy 10^{55} erg, and average age 2×10^{7}yr, therefore their source must accelerate cosmic rays at an average power level 2×10^{40} erg/sec. As the type Ib supernovae are much less in late-type of normal galaxies, and lying above the equatorial plane, they are less considered for the acceleration of relativistic particles. There is no radio emission detected from type Ia supernovae. Discrete SNRs themselves contribute only a small fraction for the non-thermal total flux density from M31 and other nearby galaxies.
Most nonthermal emission from the normal galaxies is smooth, and appears at large scale length because of the cosmic-ray transport, so it is difficult to find out the spatial distribution of their sources. From the radio maps of many normal galaxy disks (Bicay & Helou, 1990), it is clear that, due to the cosmic rays propogation, non-thermal radio scale lengths are usually greater than both the optical scale lengths of old disk stars, and the FIR scale lengths tracing the recent stars. Hence, the radio scale lengths can not be used to differentiate between the old and young stellar populations.

1.3.3 The Radio-FIR correlation

The dusty HII regions absorb the uv-radiation or star-light from the massive young stars, and re-radiate in infrared frequencies which is basically thermal emission. The supernova remnants produced by these massive young stars are supposed to accelerate the relativistic electron causing the non-thermal synchrotron emission. *FIR* measures the majority of flux reradiated by dust in normal galaxies. The flux densities at $\lambda = 60\mu$m and $\lambda = 100\mu$m from the IRAS survey can be used to calculate the quantity *FIR*, which is the total flux between $\lambda \sim 40\mu$m and $\lambda \sim 100\mu$m, and given by :

$$\left(\frac{FIR}{W\,m^{-2}}\right) = 0.336\left(\frac{2.58S_{60\mu m} + S_{100\mu m}}{Jy}\right) \tag{1.9}$$

Helou et al(1985) defined the parameter q as a logarithmic measure of the FIR/radio flux density ratio. Following Condon at al(1991) q is given by :

$$q = log\left(\frac{0.336 \times [2.58S_{60\mu m} + S_{100\mu m}]}{Jy}\right) - log\left(\frac{S_\nu}{Jy}\right) \tag{1.10}$$

Where $\nu \sim 1.4$GHz is assumed unless specified. The distribution of q was found to be quite narrow (rms scatter $\sigma_q \lesssim 0.2$) about the median $\langle q\rangle \sim 2.3$ at 1.4 GHz among the spiral galaxies in Virgo (Helou et al 1985), extragalactic FIR sources selected at $\lambda = 60\mu m$ (Condon & Broderick 1986,1991) and radio flux limited samples of normal galaxies (Condon & Broderick,1988, Condon et al 1991b) .
The q parameter for NGC 2997 and NGC 4565 is 2.29 and 2.37 respectively at 1.49 GHz (Using 1.49 GHz flux densities from Condon (1987), and flux densities of NGC 2997 (A.J.Fitt et al,1992) and NGC 4565 (R.J.Wainscoat et al, 1987) at 60 μm & 100 μm).

The observed FIR/radio correlation is not precisely linear, especially in optically selected samples containing very low-luminosity galaxies. Galaxies with low FIR luminosities have even lower radio luminosities than expected. Such a nonlinearity would occur if either the FIR or radio luminosity is not directly proportional to the *star-formation rate*. Various corrections were tried (see Condon's review, 1992) to linearize the FIR/radio ratio by either subtracting the cool "cirrus" component of dust ($T \sim 20K$) from the FIR luminosity of each galaxy, which is not related to star-formation activity, or by making the corrections for cosmic rays losess (by diffusion or convection) which causes the low radio-luminosity of galaxies. For two well defined samples of normal galaxies, 1.49 GHz observervation of optically selected samples of spiral galaxies brighter than $B_T = +12$ and the IRAS Revised Bright galaxy sample with $S_{60\mu m} \gtrsim 5.24$ Jy, Condon et al(1991a) found that none of the corrections described above can simultaneously linearize the FIR/radio correlation. The galaxies needing the largest corrections generally have the lowest radio and infrared luminosities but normal blue luminosities, suggesting that their current star-formation rates may be lower than the average over the last $\sim 10^9$ yr.
Devereux & Young (1990) used the F(H_α)/FIR ratio to suggest that the dust contributing to FIR is heated primarily by stars with $M \gtrsim 6M_\odot$, at least in galaxies with $L_{FIR} > 10^9 L_\odot$. Both L_{FIR} and production rate of cosmic rays thus appear to be linearly proportional to the recent star-formation rate of massive stars in normal galaxies.

1.3.4 Nonthermal luminosity and the supernova rate

Various models have been tried to relate the supernova rate and the nonthermal luminosity of galaxies including starbursts and syfert galaxies by Biermann(1976), Ulvestad(1982) and Gehrz(1983), where it needs either the higher supernova rate than observed or increase in nonthermal energy per supernova (factor of 10 higher). Ulvestad(1982) suggested that instead of stars, radio sources in most syfert galaxies are powered by AGNs. Heckman et al (1983) also argued that monsters in AGNs, not starbursts, power strong nuclear sources in spiral galaxies since the average radio spectral index $\langle\alpha\rangle \sim 0.45$ of Galactic SNRs is significantly less than average spectral index $\langle\alpha\rangle \sim 0.75$ of spiral galaxies.
Almost all the observed nonthermal synchrotron emission in spiral galaxies comes from the relativistic electrons which are thought to be accelerated by supernova remnants, but 90% of this emission must be produced long after the individual short-lived parent SNRs have faded out, and the electrons have diffused throughout the galaxy(Pooley 1969,Ilovaisky & Lequeux,1972). Therefore, assuming the observed Galactic relation between nonthermal luminosity (L_N) and supernova rate (ν_{SN}), Condon & Yin (1990) equation implies :

$$\left(\frac{L_N}{10^{22}W/Hz}\right) \sim 13\left(\frac{\nu}{GHz}\right)^{-\alpha}\left(\frac{\nu_{SN}}{yr^{-1}}\right) \tag{1.11}$$

. The equation 1.11 probably applies to most normal galaxies.

1.3.5 Radio emission from normal galaxies and SFR

The average formation rate of stars (SFR) more massive than $5M_\odot$ is given by the initial mass function $IMF\Psi(M) \propto M^{-5/2}$, truncated at upper mass limit $M_U \sim 100M_\odot$

$$\left[\frac{SFR(M \gtrsim 5M_\odot)}{M_\odot yr^{-1}}\right] \equiv \int_{5M_\odot}^{M_U} M\Psi(M)dM \tag{1.12}$$

All stars more massive than $8M_\odot$ become supernovae, so the radio supernova rate ν_{SN} can be determined directly by the SFR, hence we can determine non-thermal luminosity L_N using the eq(1.11), which is given by

$$\left(\frac{L_N}{WHz^{-1}}\right) \sim 5.3 \times 10^{21} \left(\frac{\nu}{GHz}\right)^{-0.8} \left[\frac{SFR(M \gtrsim 5M_\odot)}{M_\odot yr^{-1}}\right] \tag{1.13}$$

If Lyman continuum photon absorption by dust is very less, the radio thermal fraction can be estimated from stellar models for an assumed electron temperature $T_e \sim 10^4$K. The results of Kennicutt (1983) implies that, $L(H_\alpha)$ is proportional the SFR($M \geqslant 5M_\odot$). From the H_α optical line flux and using the approximate known value for the ratio of line fluxes of $F(H_\alpha)/F(H_\beta)$ (see review by J.J. Condon,1992), we can calculate the H_β line flux and the thermal fraction (S_T). Hence, the relation betweeen thermal luminosity L_T and star-formation rate is :

$$\left(\frac{L_T}{WHz^{-1}}\right) \sim 5.5 \times 10^{20} \left(\frac{\nu}{GHz}\right)^{-0.1} \left[\frac{SFR(M \gtrsim 5M_\odot)}{M_\odot yr^{-1}}\right] \tag{1.14}$$

The average observed value of thermal fraction S_T/S from equation (1.6) agrees well with the ratio of equations 1.13 and 1.14.

Most of the luminosity in the band measured by FIR is from dust heated by stars more massive than $M \sim 5M_\odot$ (Devereux & Young 1990,Xu 1990). The L_{FIR} luminosity from a time independent IMF is given by $L_{FIR} \sim 0.66 \int_{5M_\odot}^{M_U} \Psi(M)L(M)\tau(M)dM$, where $\tau(M)$ is the lifetime of a star with mass M, and L(M) is its average bolometric luminosity. The total energy $L(M)\tau(M)$ emitted by a massive star during its main-sequence life (Maeder 1987) can be approximated by $L_\tau \sim 10^{9.6}(M/M_\odot)^{3/2}L_\odot$yr. If the IMF slope is $\gamma \sim 2.5$ for $M \gtrsim 5M_\odot$, then each logarithmic stellar mass range contributes equally to L_{FIR},

$$\left(\frac{L_{FIR}}{L_\odot}\right) \sim 1.1 \times 10^{10} \left[\frac{SFR(M \gtrsim 5M_\odot)}{M_\odot yr^{-1}}\right] \tag{1.15}$$

. Thus, both radio ($L_T + L_N$) luminosity and FIR luminosity are proportional to the star-formation rate $SFR(M \gtrsim 5M_\odot)$. Since SFR is the only one free parameter, only one observable parameter (e.g. radio luminosity) per galaxy is sufficient to calculate other model parameters. The FIR/radio ratio at $\nu \sim 1.4$ GHz predicted by equation 1.13,1.14 and 1.15 is $q \sim 2.4$, which is consistent with the observed $\langle q \rangle \sim 2.3$ for moderately luminous ($L_{FIR} \gtrsim 10^9 L_\odot$) galaxies (Condon et al 1991a). Therefore, this simple model suggests that the FIR and radio luminosities depend on $SFR(M \gtrsim 5M_\odot)$ only, whereas other factors, such as magnetic field strength does not play such a significant role.

1.4 Radio continuum structure of spiral galaxies

Galactic radio emission from two well known radio contour maps at 3.5 m by Mills, and at 22 cm by Wasterhout reveal two main components of Galactic radio emission. At meter wavelength, where non-thermal emission predominates, the map shows a relatively narrow ridge component following the Galactic equator with thickness (500 pc) and a wide extended weak component over the whole sky, the intensity of which slowly diminishes away from the Galactic plane. Whereas, at decimeter wavelength, the extended component does not appear and the ridge appears even narrower (200 pc) with its apparent temperature being 20°K, which is much less than the several tens of thousands of degrees observed on 3.5 m.

At decimeter wavelength thermal component comes from a disk of ionized interstellar hydrogen whose brightness temperature varies as ν^{-2}, while the brightness temperature of the nonthermal component varies as $\nu^{-2.7}$. The density of ionized hydrogen varies greatly from the center to the periphery of the galactic disk, and its excitation temperature is estimated at 10,000°K. The brightness temperature of nonthermal component at decimeter wavelength is below 10,000°K, hence ionized gas appears in emission above the nonthermal compoent. On meter-wavelengths, the brightness temperature of the nonthermal radiation is of the order of 10,000°K, which is the same as the excitation temperature of ionized hydrogen, so, at this wavelength ionized hydrogen and nonthermal component from relativistic electrons contribute equally to the total emission of the galactic ridge. The situation on decameter wavelengths is quite the opposite, the brightness temperature of the nonthermal component reaching ∼100,000°K, and the nearby ionized hydrogen appears to be everywhere in absorption and not in emission.

Van der kruit (1973) separated the radio emission from a sample of spiral galaxies observed at 1.415 GHz with WSRT into nuclear, spiral arm, and base disk component. The base disk compnent contains most of the flux density which is largely nonthermal and extended over the whole optical map.

1. The disk radio emission : In order to separate any nuclear component from the possibly present disk emission, the half-power beamwidth of the radio telescope should be less than about one-fifth of the galaxy Holmberg diameter. It has been known that emission from detectable radio disk component roughly coincident with the optical disk, and the brightness of the radio disk generally decreases with increasing distance from the center of galaxy. In several cases (e.g. NGC 253,4556,891 and 55), the position of the centroid of the disk brightness does not seem to correspond to the position of the galaxy. The mean radio disk brightness does not seem to correlate with any of the usual integral properties of spiral galaxies such as total mass or luminosity (Van der kruit, 1973c). The range of brightness of disk emission varies considerably from 0.1 K to 10 K at 1415 MHz; the plot of monochromatic luminosity of the nucleus against the average brightness temperature of the disk (Van der kruit, 1973c, Ekers 1975) shows apparent relation between the power of the nuclear radio source and the average brightness temperature of the disk, suggesting significant contribution by the nucleus to the relativistic particles in the disk.

The spiral galaxies with relatively bright disk emission like M51, NGC 6946 , NGC

4736 and NGC 891 shows the change in spectral index that somewhat steepens with radius. van der Kruit attribute this variation of spectral index to radially varying contribution of thermal emission from HII regions, and concluded that there is no evidence at least over the brighter part of the disk that the spectral index of the nonthermal radio emission changes with radius. The spiral galaxies with faint disk emissions like M31 and M81, shows radial profile which is characterized by minimum at 4 and 2 kpc and broad maximum at 9 and 5 kpc respectively, with an exponential fall-off beyond the broad maximum in outer regions for both the galaxies. For M31 the HII regions peak radialy at about 9 kpc where it is strongly concentrated in ring but exhibits nonthermal emission at 408 MHz and 1417 MHz (pooley, 1969). The radial distribution of HII regions and nonthermal emission probably behaves similarly for our Galaxy. The spectral index of M81 (Segalovitz, 1977b) is rather uniform starting in the inner minimum to outer regions, the radio spectrum is clearly nonthermal, the same characteristic follows from the work by Berkhuijsen (1977) on M31.

origin of disk radio emission : On the basis of the general similarity of the radio continuum extent in external spiral galaxies with that of the extreme Pop I (in particular the HII regions), Lequeux(1971) suggested that the supernovae of type-II associated with this young population are the prime source of cosmic rays. But, the detailed analysis of M51 and NGC 6946 by van der Kruit (1977) shows that the nonthermal emission is in the radial direction distributed similarly as the total stellar component and certainly different from the HII regions. The central regions of many spiral galaxies are often relatively devoid of HII regions, whereas the nonthermal continuum disks appear to increase maxima located on or near the nuclei of the galaxies. Also, it is the general property of spiral galaxies that the HI gas falls off much slower than the radio continuum brightness, so the nonthermal emission certainly does not correlate with the extreme Pop-I. van der Kruit et al. noted that the radial distributions of nonthermal emission and optical light are also simillar to those derived statistically for supernovae in galaxies. They concluded that it is then reasonable to consider supernovae, their associated remnants and/or pulsars as important sources of cosmic rays. Galactic γ-ray observation (Dodds et al, 1975;Stecker, 1977) also gives evidence that the distribution of relativistic electrons closely follows that of the total stellar mass of supernovae.

2. Spiral structure : High resolution aperture synthesis observation of M51 at $\lambda \sim$ 49, 21, and 6 cm wavelength presneted by Mathewson et al. (1972) shows two ridges of radio emission that followed the two spiral arms quite accurately. The resolution of the telescope and intrinsic sharpness of the ridges enabled them to show that these ridges coincide accurately with the dust lanes that are visible on the optical photographs at the inner edges of the arms. In a galaxy with trailing spiral structure and a rotation of the pattern slower than the material, shocks will develop at the inner edge of the spiral potential well. At these positions where star formation is supposed to be triggered and which are outlined in optical pictures by thin dust lanes, the gas compression is accompanied by a strong enhancement in magnetic field strength, because the frozen-in magnetic field is compressed with the gas. For the synchrotron mechanism the volume emissivity is proportional to $KB^{1-\alpha}$, where K is the number density of electrons, B the magnetic field strength, and α the spectral index of the

radio emission. Therefore, in a simplified approach the enhancement in brightness temperature of the radio continuum emission will be a factor $(\rho_1/\rho_0)^{2-\alpha}$, where ρ_1/ρ_0 is the relative density contrast in the compression regions. Mathewson et al. have shown that with $\alpha \sim 0.7$ this can reproduce the observed distribution.

A high resolution (15 arcsec) total intensity map of M51 at λ20 cm by N.Neininger (1996) is given in fig.1.4-a. This map is retrieved from the NED data-base and overlaid on the optical image from the Palmor Observatory Sky Survey (POSSI). Radio contours are plotted with the rms σ=0.2 mJy/beam for the clarity. Contours levels are (-5, -3, 3, 5, 6, 7, 9, 10, 15, 20, 25, 30, 35, 40)$\times$ σ. M51 radio map shows two principal grand design spiral arms.

A very crude estimate of the amount of compression (van der Kruit,1973c) based on the notion that at the position of the compression regions there is an enhancement of the general disk emission, and this enhancement is directly related to the density contrast and hence the shock strength. Assuming that the thermal contribution of HII regions to the total flux density is small at 1.415 GHz the overall spectra of the total flux density are strongly nonthermal, the rough estimate of the flux density of the base disk was found, and using the longer baselines where the base disk has a very low fringe visibility, while the small-scale compression region do not, the total flux density of spiral arms were measured. Depending on the relative flux densities of spiral structure and base disk, the twelve galaxies were simply devided into three groups with weak (e.g. M33,NGC 2403), intermediate (e.g. M31,M81,M101) and strong (e.g. M51,NGC2903) compression (van der Kruit & Allen,1976).

3. Central radio source : The extended source at the Galactic center is nonther-

Figure 1.4: The VLA radio contour maps of nearby spiral galaxies at λ20 cm.

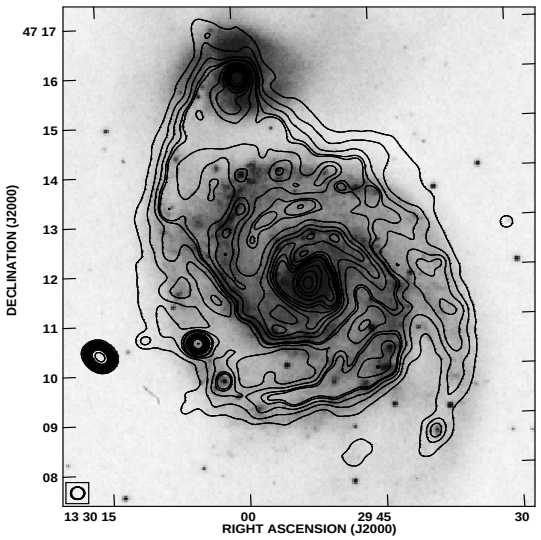

fig.a Face-on : M51-SAbc (N.Neininger,1996)

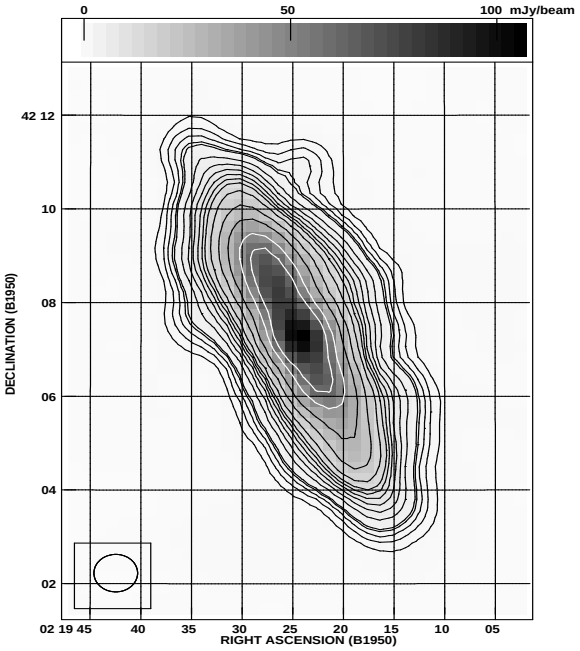

fig.b Edge-on : NGC 891-SAb (Condon et.al,1996)

mal, as its flux density varies as the -0.7 power of the frequency, i.e. it is much more intense at meter wavelengths than on shorter wavelength. At very long wavelengths (15.2 m), part of the compact central source shows in absorption, which is similar to the characteristic shown by interstellar ionized hydrogen in galactic regions, therefore it is found to be thermal. The nuclei of normal galaxies contribute generally less than 20% to the total flux density of the galaxy (van der kruit, 1973c). The nucleus of M31 is similar to our galaxy in linear scale ($\sim 8pc$), but the radio output is an order of magnitude lower, and the spectrum is nonthermal. M81 shows a small-diameter radio source at the nucleus, about twice as bright as in our Galaxy with spectral index value $\alpha = 0.3$. M51 has a nuclear source that is an order of magnitude brighter than the Galactic center. Thus, among the nuclei of the bright, nearby galaxies there is a large diversity in radio properties.

The properties of nuclei have been studied with increasingly better resolution and/or large samples by Lequeux (1971), van der Kruit (1972,73) and Ekers (1974,75); several conclusions follow from these samples stated by van der Kruit & allen(1976) that the nuclei of Seyfert galaxies emit two to three orders of magnitudes more energy at radio wavelengths than does the average normal galaxy nucleus. There is no good correlation between the luminosity of the nucleus and the Hubble type or the presence or abscence of a bar, whereas the radio emission appears correlated with 10μ infrared emission. In the case of interacting galaxies, it appears that the total radio luminosity as well as that fraction of it associated with the nucleus are normal compared to spiral galaxies in general.

4. HII regions : The radio emission from HII regions in Galactic plane are prominent at centimeter-wavelength, but these objects are small and faint when compared to the general extended nonthermal emission found in most galaxies. The high angular resolution (of the order of 10") and the higher sensitivity (of the order of $\lesssim 1$ mJy) is necessary to measure radio emission from HII regions in most distant galaxies. The giant HII complexes in M101 at a distance of 7 Mpc have linear sizes around $\sim$ 1kpc and emit about $50 \times 10^{17} WHz^{-1}sr^{-1}$ at centimeter wavelengths; these values are considerably larger than those corresponding to the largest HII regions in our Galaxy (W51), in M33(NGC 604) and in the LMC (30Dor) which is of the order of $0.1 - 0.3$ kpc in size and $3 \times 10^{17} WHz^{-1}sr^{-1}$ in power. The presence of large amounts of dust internal to the HII regions in M33 and the giant complexes in M101 is indicated from a comparison of the optical and radio results (Israel & van der Kruit,1974;Israel,1975). A sub-arcsecond-resolution VLA imaging of four nearby spiral galxies : IC342, Maffei 11, NGC2903, and NGC6946 (Chao-Wei Tasi et al) shows that roughly 60% of the compact sources appear to be HII regions with flat or positive spectral indices ($\alpha \gtrsim -0.1$). The HII regions with rising spectra are optically thick at centimeter wavelengths, and thus fairly dense ($10^4 cm^{-3}$) and presumably very young.

5. Supernova remnants : Galactic SNRs are classified in four different types namely, the shell-type, filled centre (Crab nebula), composite, and barrel shaped. About 80% of the known Galactic SNRs are of the shell type e.g. Tycho's SNR, SN1006 etc. David Matonick & Robert Fesen (1997) presented the results of an optical search for supernova remenants in the spiral galaxies NGC 5204, NGC 5585, NGC 6946, NGC 81, and M101, using the criterion that emission nebulae with [SII]/$H_\alpha \gtrsim 0.45$

are identified as SNRs, they found plenty of SNRs in each galaxy ranging from three to few tens. Kong, A.K.H et al(ApJL,2003) have detected a spatially resolved SNR in the center of Andromeda Galaxy in radio, X-ray, and optical wavelengths.

6. Z Extent of the radio emission and radio haloes This sub-section mainly describes the distribution of radio emission perpendicular to the plane of the galaxies. The broad component of radio emission (z-distribtuion) as compared to that of the HI or optical light from the disk is refered to as *halo* or *thick-disk* in the case of more descriptive manner. It is difficult to morphologically disentangle emission from galaxy disks and haloes. For the sake of discussion, van der kruit et al (1976) distinguish the halo from a thick disk if the axial ratio of the faintest reliable radio contours exceeds 0.5; which may be affected by the sensitivity of the observation. The present observations of the Milky Way and other external edge-on galaxies (Micheal Dahlem, 1997) shows various phases of ISM in their thin disks, and outside of thin disks i.e. in haloes, which can be detected by various ISM tracers (refer table 1.2) like HI, H_α, and molecular lines, as well as radio continuum and soft X-ray emission. The current theoretical models of the ISM take into account that gaseous haloes are the natural extensions of disk ISMs and are heated by the winds and ionizing radiation of massive stars, and by the shock waves of supernovae and their remnants. The existence, the shape and the properties of gaseous haloes depend on the level of energy input into the disk ISM per unit surface area by the star-formation related processes. The detailed review on gaseous haloes of late-type spiral galaxies is given by Dahlem(1997). Normal galaxies are categorized in three types with respect to their star-formation (SF) and halo properties. NGC 891, NGC 5775 and NGC 2820 are the normal galaxies having higher star-formation rate than the Milky Way, with no central starburst. The radio continuum haloes have been detected in these systems. Allen, Baldwin & Sancisi (1977) observed NGC 891 (Distance$\sim$ 13 Mpc) at 6, 21 and 49 cm, and made maps with identical beam shapes. They separated the emission into two components; at 6 cm one component has thickness of less than 0.5 kpc, similar to the HI which might be thermal, while a second nonthermal disk has a thickness of about 4kpc. These components are in agreement with the 408 MHz result of Baldwin & Pooley (1973). The radio spectra generally seems to be steeper than those closer to the plane, emission was traced out to about 6 kpc above the plane which shows existence of radio halo in NGC 891. The VLA total intensity map of NGC 891 at λ20 cm (Condon J.J. et al., 1996) is shown in fig.1.4-b, the radio contours are plotted with the same level as drawn for M51 map in fig.1.4-a.

NGC 3044, NGC 4565 and NGC 5907 are the galaxies with intermediate SF levels which shows disk-halo interaction only in a few locations where the local SFR is high. These galaxies have SFRs and SN rates similar to those of our Galaxy. Only marginal signs of emission from gaseous haloes have been detected in these systems. In NGC 4565 and NGC 5907 Hummel et al.(1984) could find only marginal indications of the existence of radio halo emission at 610 MHz and 1410 MHz. Although NGC 891 does show some halo emission at 10.7 GHz, Dumke et al (1995) could not detect the haloes from galaxies NGC 4565, NGC 5907 & NGC 7331, all of which have intermediate levels of SF. NGC 4565 shows only a few tiny dust filaments oriented perpendicular to the disk and a tentative detection of soft X-ray emission close to the disk was reported

by Vogler et al(1996). Galaxies with low SF rates and SN rates like NGC 4244 do no show any signs of haloes.
Based on halo morphology, there are three types of outflows driven by SF processes: central outflow cones, extended halos, and mixtures of both (Dahlem,1997). These three correlate with the distribution of high-level SF in the galaxy disks. Cones are observed above circumnuclear starbursts (e.g. M82, NGC 3079); the width of the base of the cone depends on the diameter of the starburst region. Extended haloes are found above widespread SF in galaxy disks (e.g. NGC 891), and mixed activity shows a superposition of the two types of outflows (e.g. NGC 4666). Early-type of spirals (S0 to S_{ab}) contain very little gas and/or dynamically hot (velocity dispersion of their ISM is high), hence the gas condensation into cold dense clouds is suppressed. Whereas, the gas disks of late-type spirals (S_b to S_{dm}) are more relaxed, enabling the condensation of gas into giant molecular clouds, where massive star formation take place. Thus, only S_b or later, host giant extragalactic HII regions (GEHRs), (Kennicutt 1984,1989). As mentioned above, the distribution of these GEHRs can vary (starburst vs widespread SF). Individual GEHRs appear to be able to drive disk-halo interactions: Two of the examples are that suggested by the correlation of the sites of radio knots with gaps and filaments in the radio halo of M82 (Reuter et al.1994) and the association of the most powerful SF region and the brightest radio continuum spur in the halo of NGC 4631 (Golla & Hummel 1994). This suggests that high-level SF in GEHRs creates over-pressurized hot ionized gas through the conversion of kinetic energy (from stellar winds and SNe) into heat (via shocks). The gas then convects out of the thin disk along the steepest pressure gradient i.e. perpendicular to the disk.
Allen et al.(1977) suggested the model for interpretation of the observed z-distribution of the radio emission in NGC 891, in which electrons diffuse out of the disk. A steepening of the radio spectral index above the thin disk indicates energy losess. This effect plus a fall-off of magnetic field strength with z would indicate a propogation time of 4×10^7 yrs or more for the electrons to reach a height of 4 kpc above the plane. The study of containment of cosmic rays given in the review by van der kruit (1978) concluded : (i) Whenever a spiral galaxy has a strong radio disk and its orientation is sufficiently edge-on there appear to be z-extensions up to at least 2 kpc accompanied by a steepening of the spectrum with Z; also, in these brighter systems the electrons are not contained in the disk, but diffuse into the halo. (ii) The radio spectra that steepen with z cannot be due to thermal emission. (iii) Relativistic electrons diffuse out of the disks after travelling not very far ($\sim$ 1 kpc in about 10^7 yrs.) from their place of origin.

1.5 NGC 2997, NGC 4565 radio continuum observations : A brief review

NGC 2997 :

The optical parameters of NGC 2997 are given in table 1.3. NGC 2997 is a southern late-type spiral galaxy (Sc) with no obvious interacting companion (Milliard & Marcelin 1981). Optical map shows two dominant symmetric spiral arms, the southern arm bifurcates towards the south-west side into the third arm (Block et al,1994). The galaxy has an inclination angle of 40°, and a mean pitch angle of 13.7° for the spiral arms (Milliard & Marcelin 1981; Garcia-Gomes & Athanassoula 1993). The first published radio continuum observation of NGC 2997 is from 1.49 GHz atlas of spiral galaxies by J.J. Condon (1987), which was made at low resolution ($\theta \sim 0.8'$) using the VLA in its most compact D and C/D configuration. This map shows poorly resolved structure for spiral arms. The measured total flux density over obvious contour is 290 mJy, and the luminosity of galaxy is $8.39 \times 10^{21} W Hz^{-1}$ (Hubble distance based on $H_0 = 50 km\, s^{-1}$).
J.L. Han et al. (1999) made multi-band radio observations of NGC 2997, including total power mapping at λ20 cm with VLA in its BnC array, sensitive polarization observations at λ13 cm with the Australia Telescope Compact Array (ATCA) in five antenna configurations, and images at λ6 cm and λ3 cm with the VLA in its CnD array. Their maps shows relatively strong total intensity in arm regions. At inner edge of the arms, strong linear polarization is observed at λ6 cm, a regular magnetic field estimated in this region is around 8 μG.
Hui Men and J. L. Han (2005) did the spectral index study of NGC 2997 using the VLA at 1435.1 MHz and 1652.4 MHz; the total intensity maps at these frequencies with higher resolution could distinguish two dominant spiral arms. The spectral index maps shows that the optical arms and the central part of the galaxy have flatter spectra. They found space-averaged thermal electron density $\langle n_e \rangle \sim 0.049\, cm^{-3}$ from the measured thermal emission of about 35% of the total emission at λ3 cm.

NGC 4565 :

This is an almost edge-on (inclination angle $i = 86°$) Sb galaxy at a distance of 10.2 Mpc. The basic parameters of NGC 4565 are given in the table 1.3.
E.Hummel et al(1984) observed three edge-on spiral galaxies NGC 4244, 4565, and 5907 using the Westerbork Synthesis Radio Telescope (WSRT) at 610 MHz and 1410 MHz. They did not find any radio continuum emission from NGC 4244. However, the results of NGC 4565 and NGC 5907 showed that they have weak central sources at 1410 MHz and thick disks are found in both galaxies, with FWHP $\lesssim$ 1.5 and 0.8 kpc respectively, which is approximately constant along the major axis, and no emission is detected at large z-distances. For $z \gtrsim 3$ kpc the limits are $\lesssim$ 0.02K or $\lesssim$ 1% of disk emissivity. They made a general conclusion by comparing the radio continuum observations with other galaxies that the radio disks are thick ($\sim$ 1 kpc) and the emissivity at large-z distances is utmost a few percent of the emissivity in the plane.

Broeils and Sancisi (1985) observed NGC 4565 at 1.414 GHz with higher resolution (13" ×30") using WSRT. Their map shows presence of an unresolved source of 1.3±0.3 mJy, and moderate bright disk with a possible two component structure, i.e. thin disk ($\Delta z < 1.3$kpc) and a thick disk ($\Delta z \simeq 2.5$kpc) containing ∼60% of the total flux density. The measured radio dimensions (FWHP) are 17.8kpc × 1.8kpc. Bright thin component is confined to the plane of galaxy and the faint thick component up to ∼ 3kpc.
S. Sukumar & R.J. Allen (1991) observed the distribution of radio continuum intensity and linear polarization of NGC 891 and NGC 4565 with VLA at λ20 cm and λ6 cm using D and D, B, BnD array configurations. They observed brightness distribution of total intensity noticeably thinner than that of NGC 891. The polarization emission from NGC 4565 appears only on the southeast side of the nucleus, whereas it is almost absent towards northwest side. The line segment of their map shows that the magnetic field in NGC 4565 is generally parallel to the plane.
The edge-on galaxies NGC 891, 3628, 4565, 4631, 5907, and 7331 have been observed at 10.55 GHz using the Effelsberg 100m telescope of MPIfR (M. Dumke et al., 1995). Total intensity map of NGC 4565 at 10.55 GHz (2.8cm) also shows a weak central source and fainter maximum – north-west component along the major axis. This maximum also appeared on the λ20 cm map of Sukumar & Allen (1991).
Richard J.Rand et al.(1992) found that NGC 4565 is a weak H_α emitter, and shows no evidence for the chimney mode in its disk, and suggested that there may not be O, B stars necessary to create superbubbles and chimneys and power a significant halo. The distribution of neutral hydrogen is 20% more on the northwest side than on the southeast side (W.K. Huchtmeier et al.,1980), and HI extends to about twice the optical dimension. The WSRT map of NGC 4565 (Sancisi, 1976) shows evidence of bending at its outer edge. Such kinds of warps were found in a few other galaxies (M83, M33 and Milky way). A generally accepted explanation is that warps result from gravitaional interactions with nearby companions.

1.6 Significance of low frequency observations

A high resolution low frequency radio continuum study of normal and active galaxies is one of the goals of GMRT (G.Swarup et al., 1991) which can provide insights into several phenomenon related to non-thermal and thermal emission from galaxies such as relation between radio emission and recent star formation. A study of radial distribution of non-thermal emission across the disk, the thin and thick components in the case of edge-on spiral galaxies can address the basic question of cosmic ray physics concerning the origin, propagation, and the existence of radio haloes. Also, high resolution radio continuum maps at low frequencies are useful to study the compact nuclear bursts, HII complex regions, and the detection of radio supernovae & SNRs in external galaxies.
As mentioned before, NGC 2997 has been studied well for total intensity mapping, spectral indices, and polarized emission above λ20 cm by J.L.Han et al. (1999) and Hui Men & J.L.Han (2005). But low frequency data of NGC 2997 below λ20 cm is

not available yet. Since the steep spectrum of synchrotron radiation is dominant at low frequencies, the GMRT observations at meter-wavelength with high angular resolution and high sensitivity can reveal many significant features of NGC 2997 due to its face-on appearance ($i = 40°$), such as smooth synchrotron emission from the disk and its confinement, morphological structure of spiral arms, nucleus, and detection of the compact HII regions, supernovae and SNRs residing in the spiral arms.
Although all nearby edge-on starburst galaxies have gaseous haloes (Dahlem et al., 1998), radio haloes are rare among normal galaxies (Hummel et al., 1991b). It is hard to find a weak extended emission from haloes which become too faint at high frequencies (GHz). Further, there is difficulty in disentangling emission between the galaxy disk and halo. Therefore, an edge-on candidate like NGC 4565 ($i \sim 86°$) which has a favourable inclination geometry was also chosen for our study.
E.Hummel et al.(1984) observed NGC 4565 at 610 MHz and 1410 MHz using the WSRT with a synthesized beam (arcsec) $\sim 57 \times 130$ and 25×57, respectively. They found a weak central source with a radio power of log(P) =19.3 and $\lesssim$18.4 $W\,Hz^{-1}$ respectively; their maps could distinguish between the thin and thick disk components of the galaxy. A.H. Broeils & R.Sancisi (1985) observed NGC 4565 at 1414 MHz with high resolution (13" × 30") and detected emission from the thick disk up to $\simeq$ 2.5 kpc. Therefore, it was considered useful to search for radio halo in NGC 4565 at lower frequencies. The statistical properties of these objects like radio-luminosity, radio-optical correlation, and distribution of spectral indices are still poorly known at low-frequencies; therefore we are aiming to study these properties as well.
In addition, GMRT multi-frequency radio continuum observation of NGC 2997 and NGC 4565 are of interest for the following reasons :
1.Total emission spectral study : The power-law nature of nonthermal synchrotron emission shows that the steep spectra ($\alpha \sim -0.8$) overwhelms the free-free emission (or bremsstrahlung; flat spectra $\alpha \sim -0.1$) below 30 GHz; the thermal free-free emission component almost becomes opaque below 1 GHz. It is also larger towards higher frequencies (30-200 GHz), but the flux measurements at higher frequencies are relatively poor and rather uncertain to measure the thermal fraction (refer fig.1.3). If the integrated flux from a galaxy is considered, the thermal and nonthermal components can be separated by considering the synchrotron spectral index as a free parameter and fitting the composite spectra (thermal free-free plus synchrotron emission) to the observed integrated flux densities over a large range of frequencies (N. Duric et al.1988). Therefore, we can fit the two component or power-law model to the total flux density radio spectrum of NGC 2997 and NGC 4565 to determine the relative contribution of the thermal and nonthermal flux density, and its subsequent possible studies to determine star-formation rate, measurement of the thermal electron density, and the supernova rate etc. (refer section : 1.3.4, 1.3.5).
The radio spectrum of the integrated flux densities including GMRT low frequency measurements can be checked to see whether the spectrum is steeper or gives any indication of a break in the spectrum reported by Hernett (1984).
2. Spectral index distribution study : The spectral index distribution $\alpha_{\nu_1\nu_2}(l,m)$ between the maps $S_{\nu_1}(l,m)$ and $S_{\nu_2}(l,m)$ at two frequencies ν_1 and ν_2 can be dervied by assuming the power-law : $S_\nu \propto \nu^\alpha$, where α is the spectral index. Spatial isola-

tion of the brightest HII regions (GEHRs)in radio maps is easier to achieve than the global spectral separation of the thermal and nonthermal components because the radio emission from HII regions are more compact than the smooth synchrotron disk and spiral arm emission regions. V. Firpo et al.(2005) detected two Giant HII regions close to the spiral arms of NGC 2997 using high resolution spectra ($\lambda 3726 - 7136\, A^{\circ}$), and suggested that a powerful starburst is the source of ionizing energy. Hence, the spectral index distribution study of NGC 2997 is useful for identification of such Giant HII regions, and also useful to locate some regions of intense nonthermal emission which could be the local site for generating the relativistic electrons in the disk of galaxy.
In the case of edge-on spirals, the thick radio disks and haloes can be explained by models where the relativistic electrons originate in the thin layer and diffuse into a more extended region (Bulanov et al., 1976; Strong,1977,1978). Broadly, thin disks are known to have thermal emission, and thick disks have nonthermal emission in edge-on galaxies. The spectral index distribution along the major axis and minor axis can resolve the thin-thick components of disk morphology.

1.7 The contents of this thesis

We have organized this thesis mainly in two parts; the first part deals with the observationl details using the GMRT and data reduction procedure followed using the AIPS for the total intensity mapping of NGC 2997 and NGC 4565. The first part also includes basic theory of Fourier synthesis imaging, imaging in practice, image reconstruction method used in the AIPS, and the mapping problems occuring at low-frequencies like non-coplanarity of baselines, and strong back-ground sources in the large field of primary beam. The second part mainly describes multi-band radio continuum observationl results via total intensity maps obtained over a variety spatial scale resolution for the selected samples of normal spiral galaxies. To study the radio continuum emission from normal spiral galaxies at meter-wavelength, we have given the introductory theory of spiral galaxies, their morphological properties, and introduced our objects with basic optical parameters. For the interpretation of the obtained total intensity maps, we revised briefly the theory related to radio emission from normal galaxies and radio continuum structure of spiral galaxies.

The first section of this chapter gives introduction of Fourier synthesis imaging and mapping steps to be followed in AIPS to obtain total intensity maps. Second section introduces the morphological basic properties of spiral galaxies, basic data for the selected samples, and the criteria being considered for normal galaxies vs active galaxies. In section 1.3, we have discussed the theory related to radio continuum emission from normal galaxies which is mainly based on the review by Condon J.J (1992); section 1.4 describes the radio continuum structure of spiral galaxies. In section 1.5, we have given a brief review on the radio continuum observation of NGC 2997 and NGC 4565 using other telescopes. We have justified our aim and significance of low-frequency observation of NGC 2997 and NGC 4565 using the GMRT in

section 1.6.

Chapter-2 deals with the observational details and data reduction procedure followed for the continuum data sets acquired for this thesis. Section 2.1 describes the GMRT from the continuum observational point of view where we have given information about the feeds, receiver system, possible correlator configuration modes and the data acquisition system currently being used. Section 2.2 is about the observational procedure used for the selected samples of spiral galaxies. The reduction procedure used for the low-frequency GMRT continuum data differ in some aspects than the standard reduction procedure described in AIPS cookbook; the section 2.3 describes this procedure with the details in order to get high dynamic range maps.

In Chapter-3, we have mainly emphasized the imaging procedure followed using the AIPS to map low surface brightness objects like NGC 2997 and NGC 4565. Section 3.1 discusses the imaging aspects in practice which gives the details of various controlling parameteters in order to get the high sensitivity of an image. A study of CLEAN and MEM deconvolution algorithms, its implementation in AIPS, and these methods used in practice to map NGC 4565 at 610 MHz is described in section 3.2. The section 3.3 discusses the issues related to the sensitivity of an image. An FX type spectral channel correlator of the GMRT gives an output of 128 channels for each polarization of each side-band in indian-polar mode. To form the continuum data base, all channels have to be collapsed. In image domain, the radial- and azimuthal-smearing of the source brightness distribution far from the phase center can occur due to the averaging of visibilites in the frequency and time domain. In section 3.4, we have explained the details to avoid these effects (bandwidth smearing and time smearing). A number of strong background sources in the primary field of view is larger at meter-wavelength which limits the dynamic range of the map by adding noise due to its incoherent sum of sidelobe response. In order to detect a weak and extended emission feature in the image, the confusion "noise" due to background must be reduced. In section 3.5 we have discussed these issues. The array configuration at the GMRT has significant component parallel to the earth's axis in order to maximize the *uv* coverage, due to the non-coplanarity of baselines sources away from the phase center gives phase errors which can severely distort the image. In section 3.6, we have discussed possible solutions and the implemented method to reduce this effect, called *w-term* correction. The sky brightness distribution I(l,m) across a field of view is multiplied by the primary beam response of array element; hence this result in reduction of the apparent brightness of sources depending on their positions in the primary field of view. Section 3.7 discusses the corrective measures taken to recover the actual brightness of sources withn a field of view.

Chapter-4 presents the results deduced from our multi-band observations of NGC 2997 and NGC 4565 using the GMRT via total intensity maps, spectral index distribution maps and total emission curve study. Section 4.1 summarizes radio continuum structure of both the objects based on total intensity maps obtained with variety of spatial scale resolution by applying suitable taper in spatial frequency domain and

weighting function used in the image domain. We have studied the radio continuum emission spectra for both the galaxies, and spectral index distribution maps between 325-610, 610-1280 and 325-1280 MHz for NGC 2997 in section 4.2. In section 4.3, we have tabulated observed flux densities and positions for the background sources found in a primary field of view at each of the observing frequencies.

In the last chapter, we have summarized our observational results with the derived conclusions for the selected samples for normal spiral galaxies. Also, this chapter focuses on the direction for further work related to normal spiral galaxies described in this thesis.

Chapter 2

Observing with the GMRT and Data Reduction

In radio astronomy, receiving and processing of the astronomical data is as much important as the interpretation of the data. This chapter summaries the radio continuum observations of two nearby galaxies NGC 2997 and NGC 4565 using the GMRT and the data reduction procedure followed for the continuum data sets acquired for this dissertation.

The major scientific goals and designing aspects of the GMRT are given with in detail by Swarup et al. (1991), and Ananthakrishnan & Rao (2002). The first section of this chapter gives a brief introduction of GMRT from the continuum observation point of view [1], where the information has been given about the feeds, receiver system, possible correlator configuration modes and the data acquisition system currently being used. The second section is about the observational procedure used for the nearby galaxy observation. In this section, the observing setup and the observing procedure have been described, and the pre-requisite information about the target sources has been given.

Due to the large field of view, non-coplanar baselines and frequent radio frequency interference in low frequency observations, the reduction procedure used for the low frequency continuum data differ in some aspects than the standard reduction procedure described in AIPS cookbook. The section three describes data reduction procedure which includes the bandpass and gain calibration methods and the 3-D Fourier inversion for the mapping of NGC 2997 and NGC 4565. Also, the self-calibration method applied to compensate the ionospheric effects on the visibility phases is given in section 2.3.4. Since the ionospheric effects may dominate over the tropospheric effects at L-band, we applied the same data reduction procedure for P-band to L-band continuum data. The last sub-section gives the summary of the problems faced while reducing the data for analysis.

[1] Please also see http://www.gmrt.ncra.tifr.res.in/gmrt_hpage/users/doc/doc.html

2.1 Instrument

2.1.1 The array

The GMRT is located at a latitude of 19°06′N and a longitude of 74°03′E which is ∼80 km North of Pune, India. The site chosen is about 10° away from the magnetic equator (Swarup, 1990) where the ionospheric disturbance is comparatively less, and having wide coverage of the southern and northern sky range of declination from −54° to +90°. Also, the site is protected from man made radio noise due to the surrounding hills between the site and the densely populated areas.
The GMRT array consist of thirty alt-azimuth mounted parabolic dishes each of 45m diameter, of which fourteen antennas are placed randomly in a compact central square array of 1km × 1 km size, the rest of antennas being sparsely configured in 'Y' shape having each five antennas in the North-East, South arms, and six antennas in the North-West arm. The configuration of central square gives a large number of baselines to maximize the UV-coverage near the origin of (u, v) plane which is important in order to improve the sensitivity for a large scale emission from the extended source and the arm antennas form the baselines up to ∼ 25km long to achieve the sensitivity at a high resolution. The central square provides the UV-coverage of 1 km with the shortest spacing of about ∼ 80 m by the C05, C06 and C09 antennas from the central square.

2.1.2 The antenna and Feeds

The frequency bands available for the GMRT observation are 1000-1450 MHz, 610 MHz, 325 MHz, 235 MHz and 150 MHz. The five feeds for these frequency ranges are mounted on four orthogonal faces of cube shaped turret at the prime focus of the parabolic dish, where the desired feed can be focused by rotating the turret. The reflecting surface is formed of thin stainless steel wire mesh of three sizes 10 mm, 15 mm and 20 mm, which are stretched over the inner region to the outer edge of the parabolic surface on a stainless steel wire rope backup structure. This design is known as the SMART(*Stretched Mesh Attached to Rope Trusses*) design (Swarup et al.1991). The antennas of GMRT array have an elevation coverage from 17°30′ to 90° and azimuth coverage of ±270° and it's tracking accuracy for a given source position is within ∼1'.
Except the L-band (1000-1450 MHz) feed, the two orthogonal linearly polarized signals received by the other feeds are converted to the right handed and left handed circularly polarized signals using polarizers (The L-band is kept linearly polarized to achieve a lower system temperature). The L-band feed is a corrugated horn having four sub-band each of 120 MHz bandwidth and one of them is selectable at a time with the band centers 1060 MHz, 1170 MHz, 1280 MHz and 1390 MHz, otherwise bypass mode is feasible so that any frequency is selectable in the range of 1000 MHz to 1450 MHz. The feed bandwidth for all the frequency ranges other than the L-band is around 40 MHz. The 610/235 MHz feed is dual concentric coaxial cavity; both the feeds are mounted on same turret face and one can use either one of them or both

but having only one polarization for each frequency. The 325 MHz feed is a half wave dipole over a ground plane with a beam forming ring (Kildal feed) and 151 MHz feed has two orthogonally placed pairs of dipoles above a plane reflector. The Front-End electronics is placed on the turret. The FE consists of two low noise amplifiers, one for each polarization, followed by the noise injection facility where the calibrated noise can be injected to calibrate the receiver system. A band selector switch in the common-box after the front-end electronics box can be used to set the desired band; the common-box also contains the solar attenuator switch, FE-termination, and facility for swapping the polarization signal.

2.1.3 Receiver System

At the antenna base two orthogonally polarized signals are down converted to 32 MHz wide IF bands centered at 70 MHz by using the local oscillator (referred to as I^{st} LO), which is tunable in a range of 100 MHz to 1700 MHz. The two IF signals are then converted to 130 MHz and 175 MHz using the II^{nd} LO so that the polarization information does not intermingle with each other. In order to keep the relative phase information between the electric field vectors incident on different antennas, all the thirty oscillators at the antenna base are phase synchronized to a master oscillator located in the Central Electronics building. At the IF stage, provision for limiting the RF-bandwidth to 6 MHz, 16 MHz and 32 MHz is given with the facility of IF-attenuators and the automatic level control (ALC) switch to control the gain of IF system. The IF signals are brought to the central receiver room via the optical fiber and converted back to two 70 MHz bands (one for each polarization) by using the III^{rd} LO, and provided as inputs to the baseband system. The baseband system splits each polarization band in to *upper and lower sidebands* and down converts the signals to baseband frequency by using the IV^{th} LO which is tunable in steps of 100 Hz within the range of 50 MHz to 90 MHz. Thus, by choosing the I^{st} LO and IV^{th} LO, user can select the center frequency of the observing RF band which is equal to I^{st} LO $\pm$ IV^{th} LO. The base-band system gives four final outputs, two side bands for each polarization signal where the bandwidth for these signals can be set in the range of 62.5 KHz to 16 MHz in binary steps with the adjustable gain ranging from 0 to 24 dB. Also, the ALC switches are incorporated here.

2.1.4 Digital Back-end for Interferometry

The GMRT correlator is an FX (*Fourier transform* F *before Multiplication* X) type spectral correlator which separately processes the upper and lower sideband signals coming from the base-band system by using two identical USB and LSB (Upper/Lower Side Band) correlator systems. Each USB/LSB correlator digitizes the 60 analog input voltage signals (2 pol. $\times$ 30 ant.) using the six bit ADC cards which sample the data at 32 MHz rate in order to get the input signal of maximum 16 MHz bandwidth. The given input signal for the ADC card from the base-band system is a Gaussian random signal of 0 dBm power which has minimum distortion. Function wise, the GMRT correlator has three main basic blocks, Delay-DPC (Delay

and Data Preparation Card) unit, FFT (Fast Fourier Transform) unit and MAC unit (The Multiplier and Accumulator).

a. Delay-DPC : The Delay-DPC unit takes the four inputs (2 pol.$\times$ 2 sidebands) from the ADCs for a given antenna, where it rounds off six bit quantized signal to four bit and sends it to the multiplexer. The multiplexer is used to map any of it's four inputs to it's four outputs for various operation mode of the correlator (Anish Roshi, 2000). The cosmic signal received by antennas suffers from different propagation and instrumental delays due to the relative locations of the antennas, and the different optical fiber lengths between the antennas and the correlator (called the geometric delay and fixed delay respectively). The Delay-DPC unit compensates these delays by writing the multiplexer outputs to the memory based integral delay compensation circuit (dual port RAM), but while reading the data, the location of the read pointer is kept such that the offset between the write pointer and the read pointer is equivalent to the required delay. The delay-DPC again samples the given data from the ADCs by writing the data into the memory with Nyquist sampling rate ($32/2^{\mathrm{n}}$ MHz, where n=0 to 7) which is twice the bandwidth selected for the base-band ouput signals. Hence the delay compensation can be done only in *integral multiple of the sampling interval*. Since the geometrical delay changes with the source *hour angle*, the delay unit updates this differential delay periodically (referred to as *delay tracking*).

b. FFT : From the Delay-Dpc unit, the FFT unit takes two integral delay compensated data streams (restricted to N samples -512 points) by multiplying with the data weighting function known as standard *window function*. Even after compensating the integral delays, the output of the correlator may have two types of residual phase errors ($\gamma(\tau_g) = |\nu| cos[2\pi\,(\nu_{LO}\tau_g - \nu_{BB}\Delta\tau) + \phi_\nu]$, $\Delta\tau = \tau_g - \tau_i$), one is $(2\pi\nu_{LO}\tau_g)$ due to the delay compensation done at the base-band frequency rather than the RF-frequency where the geometrical delay (τ_g) suffers, and the other is $(2\pi\nu_{BB}\Delta\tau)$ due to the compensated delay (τ_i) in multiples of sampling interval which is not exactly equal to the required geometric delay (τ_g). The phase $2\pi\nu_{LO}\tau_g$ is a function of time and is constant across the band (independent of ν_{BB}); hence this time varying phase is subtracted in the FFT sub-unit (called *fringe stopping or fringe rotation*) by digitally multiplying the integral delay compensated time series samples with the sinusoid ($e^{-j\phi_{LO}}$) of appropriate instantaneous frequency generated in a digitally implemented oscillator, known as a *Number Controlled Oscillator* (NCO).

The FFT unit has two sets of FFT engines to handle the two *fringe stopped* data streams of 512 points. Each engine Fourier transforms the 512 data points for every FFT cycle of 16 μsec (512$\times$ 1/32MHz= 1 FFT cycle) to give the 256 spectral channels. The residual phase error $2\pi\nu_{BB}\Delta\tau$ depends on the ν_{BB}, and for the broad band signal it linearly increases with the channel number producing a phase gradient across the spectrum. The phase ramp present across the spectrum obtained by FFT is equivalent to the delay ($\tau = d\phi/d\omega$) less than one sampling interval ($1/f_s$) called fractional delay. Hence, in order to correct this fractional delay a phase gradient (with Opposite sign) is applied to the spectrum given at the FFT output, which is called fractional sampling time corrections ($FSTC$).

c. MAC : For each sideband of the correlator there are 528 MACs (Three racks with

176 MAC units each) in order to compute the $30 \times (30+1)/2 = 465$ self and cross products from the 30 antennas. A single MAC unit has 256 accumulators which take the data from the two FFT units in a time multiplexed fashion i.e. it accepts four data streams (2 pol. from 2 antennas). Each MAC unit has only 256 accumulators; hence it can produce either 256 complex numbers for one polarization or 128 complex numbers each for two polarization using the same unit by averaging the two adjacent channels of FFT output from the same polarization, and accumulate for one Short Term Cycle of 128 ms duration (*1 STA cycle = 8096 FFT cycle*$\times 16\mu sec$).
The measurement of the four stokes parameters in all the 256 channels of FFT outputs for each sideband of all the antennas using the limited number of MACs available in each sideband of the correlator is not possible. Therefore, configuration-wise, there are three modes of operation of the GMRT correlator where one can measure the visibility including self correlations either from all the 4 stokes parameters but for only one sideband (Upper or Lower) or measure a limited number of stokes parameter with the full-band information. The three modes of operation are mentioned below from a user point of view.
i. *Non-Polar Mode* : In this mode, it is possible to observe only one of the two polarization RR or LL with the full-band information (16MHz $\times$ 2 sidebands) having 256 channels per sideband to improve the spectral resolution but with half the sensitivity.
ii. *Indian-Polar Mode* : This mode is used for the measurement of the total intensity (*stoke I*) on non polarized source. The measurement of both the polarization information (RR and LL) per sideband is possible, but with the averaging of the two adjacent channels of the same polarization giving only limited resolution of 128 channels per polarization per sideband. Thus, using both the USB and LSB correlator (16MHz $\times$ 2 sidebands) full sensitivity can be obtained.
iii. *Polar mode* : It is possible to measure all the four stokes parameters (RR,LL,RL and LL) using only either upper or lower sideband signal (only one of 16 MHz bandwidth) which passes through both the sidebands of the correlator. In this mode, each MAC unit gives a pair of RR,RL or LL,LR having 128 spectral channels for each stoke, which is achieved by averaging the two adjacent channels from the same stoke parameter per baseline. This gives only half the sensitivity.
Currently, only the Indian-Polar mode is released which is the standard mode of observation being used for regular astronomical observations. In this mode, the final spectral resolution corresponding to 128 frequency channels can vary in the range of 128 KHz to 0.5 KHz depending on the total bandwidth of the base-band system (ranging from 16 MHz to 64 KHz).

2.1.5 The Software system

The vast software system of the GMRT can be broadly categorized into two parts: one is the ONLINE computer system (A.P. Rao, 1991) which tunes the receiver to the desired band, focuses the feed for the astronomical observations, controls and monitors the tracking of the GMRT array for the astronomical position specified by the user. Another part of the software is the Data Acquisition System (DAS) which controls, monitors & configures the correlator in various modes of observation. It also

performs the acquisition and processes the visibility data output from the correlator in real time by using the various software programs running across the network of computers which are mainly Pentium processor based machines having Linux operating system.
At each antenna there is an antenna based computer (ABC, 80186 based microprocessor) which controls and receives the information from the two subsystems, one subsystem does the servo operation of the antenna by using the servo control computer(SCC, 8086 microcomputer) and the other subsystem focusses the feed, set/unset the receiver settings by using the monitor & control module (MCM, based on 80C535 mirco controller). The UNIX work-station in the control room is the central supervisory computer which communicates to all the ABCs of thirty antennas via the communication handler. The ONLINE software running on this workstation does most of the jobs required for the scheduling and execution of the observing projects by providing the interface which accepts the commands either from the user's desk or from the *command file* which has the observing schedule. The ONLINE software is a collection of many independent communicating processes which controls and monitors the various systems and subsystems of the GMRT array ranging from the slewing of the antenna, tracking of the array on the same region of the sky, setting and monitoring of the receiver's electronics system parameters, and log the related information. Also, cross-linking across the network is provided so that the user has selectivity and control on the various observing modes like correlator configuration, selection of sidebands and channels, sampling rate, processing & averaging of the visibility data and control over it's acquisition. A number of independent group of antennas can be formed (*referred to as the subarray*) to run independent observing projects simultaneously.
As all the subsystems of the GMRT correlator have digital based control circuits and interface cards, the correlator control PC is used to initialize, synchronize and for configuring both the sidebands of the correlator in various modes. Also it loads the instantaneous model values of delay tracking, fringe rotation and fractional delay corrections in the correlator components via the software modules. There are two separate data acquisition systems which acquire the data from MAC units by using a specially designed add on card which is mounted on the PC. The total amount of data produced in the standard mode by each sideband of the correlator is 4MB/sec (528 MACs$\times$(1s/128ms)$\times$256 channels$\times$4bytes complex number). The accuracy for time stamping the visibility data is less than 100μsec, made possible by using the complex algorithm which collects the time information from the PC clock, GPS pulse and STA pulse (R.K.Singh, 2000).
The visibility data is acquired with a data rate of 2 sec (maximum data rate can be up to 128 ms) in the standard mode of operation, and recorded in a locally generated format known as LTA format (Long Term Accumulation) which can be averaged as per the observation requirement. There are a variety of online/offline software tools developed for the rendering of raw data which can display the bandpass, antenna dependent gains, visibility plots as a function of time, baselines and hour angle. Using these tools, the bad data occurring due to the malfunctioning of the antenna systems, correlator baselines or ionospheric problem like scintillation can be checked which is very useful for debugging, consistency check of the systems while observing or for

flagging and discarding the bad visibility data.

2.2 Observations

We had a total of six successfull observing sessions for NGC 2997 and NGC 4565 using the GMRT synthesis array. Each of the three frequency bands (325 MHz, 610 MHz and 1280 MHz) were observed once for each of the two sources during the period from 2002 to 2004. The observational parameters are summarized in the table (2.2).

2.2.1 Receiver Settings

Each time, the receiver was tuned to the default continuum observation settings having center frequency 325 MHz, 610 MHz and 1280 MHz for each observing band. To improve the sensitivity the widest possible IF-bandwidth of 32 MHz, and base-band bandwidth of 16 MHz for each sideband (upper or lower) were selected with the IF and base-band ALCs (Automatic level controller) ON. The automatic level controllers (ALCs) are used to keep the system gain such that power of input signal provided to the correlator samplers are at 0 dBm. The authenticated IF-attenuations at each frequency were used to keep the ALC operating point within its linear operating range. The correlator samplers are optimized to work with an input signal of 0 dBm where the distortion of the signal is less. The visibility data was acquired using either USB or LSB correlator configured in Indian polar mode which gives the RR and LL polarization data for each sideband. As the GMRT uses spectral correlator, 16 MHz band limited signal of each sideband for each polarization is decomposed into 128 spectral channels each of 125 KHz. The visibility data was integrated over 16 second, and stored in a locally generated format known as LTA (Long Term Accumulation) format.

2.2.2 Observational Procedure

The observed visibilities on the target source are corrupted because of various reasons ranging from the instrumental gain fluctuation due to the electronic systems, residual fixed delay errors due to the change in optical fiber length or the error in presumed baseline distances, inaccuracies in the time reference for the array, sensitivity changes of the receiver with the antenna elevation, pointing offsets and the ground radiation pickup. Most of these kinds of errors can be estimated in advance before the mapping observation by observation on the strong unresolved sources, and online corrections can be made. Apart from these errors, the plane wavefront from the sky at low radio frequencies at a few 100 MHz near the plasma frequency ($\nu_p \sim 1$ to 10 MHz) is distorted by the plasma fluctuation in the earth's ionosphere which varies over the day, seasons and solar activity. Therefore, the ionospheric refraction effects are dominant where the visibility phases are severely affected by the ionospheric gain fluctuation due to the larger size scale components of slowly varying refractive index, and the smaller scale phase irregularities due to the turbulence or the temporal and

spatial density fluctuation of the electron contents in the ionosphere which are difficult to predict. To measure and remove the effects of the ionospheric gain fluctuations which vary slowly over the time scales of hours to short scale rapid variations of a few minutes, and to make the corrections for the slowly varying instrumental gains during the observing time, periodic observation on strong unresolved calibrator source is required, so that the corrections determined on the calibrator can be applied to the target source. The calibrator source used for this purpose is referred to as a *phase calibrator*. A preferred phase calibrator source should be strong enough to give a good signal to noise ratio in a short duration observation, flux density of which should be non-variable, and it should be close to the target source so that the ionospheric or changes in the antenna gain with the pointing angle can be considered as same for both.

It is generally difficult to find a phase calibrator based on the criteria mentioned above, because many phase calibrators are known to have a variable flux density over a time scale of days, and may get resolved for a given baseline length. Therefore, observation of a known non-variable, *flux-density calibrator* is required, which can be used as a flux density reference to scale the flux densities of phase calibrator and target source. The VLA flux density calibrators, 3C147 and 3C286 were used for all the observing sessions; the flux density values for these calibrators can be set according to Perly coefficients derived from the VLA observations in 1999.2. The phase calibrators 0837-198 and 3C287 used during the observation of NGC 2997 and NGC 4565 respectively were also selected from the VLA calibrator manual (1999) which are largely unresolved for all the baselines ranges (0 to 100 kλ) used for the P-band to L-band observation. The chosen VLA phase calibrators were less than 15 degree distance from the given target source; the measured flux density values are given in table 2.2. Thus, a requirement of periodic observation on such phase calibrators during the observation avoided the uv-coverage loss on the target source because the time required for positioning the antennas between calibrator and target source was less, and also the gain-phase changes close to the object of interest could be tracked with time.

As the frequency dependent antenna based complex gains vary over the passband mainly due to the filter shapes and the residual fixed delay errors, these variations change with time but much more slowly than the temporal gain-phase changes due to the atmosphere/ionosphere. Therefore, it is necessary to correct these variations before averaging the visibilities from individual channels to form a continuum database. Generally, a strong point source having a flat continuum spectrum is used to determine the bandpass response function, known as a *bandpass calibrator*. The bandpass calibration involves dividing the visibility spectra of target source by the bandpasses found on the calibrator. Therefore, the bandpass calibrator must be observed for long enough time to get a high signal to noise ratio as compared to the target source so that the noise characteristic of the bandpass calibrator does not reflect on the target source spectrum. The required observing time on bandpass calibrator should be at least $\Delta t_{BPcal} = (S_{source}/S_{BPcal})^2 \times \Delta t_{source}$. As the strong flux calibrator 3C147 and 3C286 used for the observation are spectrally flat and give better signal noise to ratio in a short time duration, we used these flux calibrators as bandpass calibrators. For

the continuum observation at the GMRT, the antenna-based bandpasses are known to be reasonably stable for a period of five to seven hours, therefore, the bandpass calibration observation was done at the start and end of each observing session for a duration 10 to 15 minutes.
The gains of the receivers are unlikely to drift significantly during the observation time. It is estimated that the antenna based gain-phase variation over half an hour or so could be well approximated by a linear interpolation (Sanjay Bhatanagar, 2001). As the given phase calibrators were strong enough to give a good signal noise ratio (refer table 2.2), we used the phase calibrators as secondary calibrators to correct the variations in gain amplitudes with time. Therefore, to correct the ionospheric and instrumental gain variations, a phase calibrator observation of 6 minutes was interspersed each time after an interval of 25 minutes of observation on the target source. To execute the observing schedule, ONLINE readable command file was prepared where the appropriate commands for alternately tracking the phase calibrator and the target source, along with the data acquisition commands were given in the loop.

2.2.3 Target Sources

Two nearby galaxies NGC 2997 and NGC 4565 were selected from the *Nearby Galaxies Catalog, R.B.Tully 1988* , for the multi-band radio continuum observations . The details of the objects and optical parameters specified in table 1.1 are given from the NASA Extragalactic Database. As the selected candidates do not lie in the galactic plane, the corrections for the background sky temperature (Tsys) was not applied in either of the cases.
The measured radio dimensions of NGC 2997 and NGC 4565 given in the previous observations are $\sim 6.3' \times 5.8'$ (H.men, & J.L.Han,2005) and $\sim 10.5' \times 1.5'$ (E.Hummel et al,1984) respectively, which are within the primary beam size of the GMRT antenna at each observing frequency. The typical system parameters of the GMRT are given in the table 2.1. The sensitivity of a radio interferometer to large scale radio emissions depends upon the shortest uv spacings available, sampling interval in the visibility plane and the total integration time on the source. The required shortest baselines of $\sim 300\lambda$ to map the extended emissions up to an angular scale of ~ 10.5 arcmin were achieved using the shortest baselines from the central square with sufficient uv coverage. Although, the highest resolution achievable by using the longest spacings from the arm antennas were around a few to several arcseconds at 1280, 610 and 325 MHz, we applied the uv-taper to visibility amplitudes at the highest spatial frequency to get a smoother synthesized beam at various resolutions so that the large-scale emission as well as compact structures embedded in extended emissions could be detected reliably (which is discussed in Chapter-4). The shortest and longest spacings used at each frequency observation are mentioned in the table 2.2. Only the NGC 4565 data at 1280 MHz suffers due to the lack of short spacings; the structure larger than the angular scale of $\sim 5.6'$ was poorly represented, which resulted in loss of sensitivity for the total intensity mapping. The number of antennas used, and the total on-source integration time for each observing session after the flagging of bad data are mentioned in the observation parameter table.

Table 2.1: System parameters of the GMRT

Frequency (MHz)	Primary Beam (Degree)	System Temp. (K)	Gain of an antenna(K/Jy)	Synthesized beam (arcsec)	RMS noise in image† (mJy)
1420	$0.4 \times (1400/f)$	70	0.22	2	0.05
610	0.9	90	0.32	5	0.1
325	1.8	100	0.32	9	1
235	2.5	180	0.33	13	2
150	3.8	450	0.33	20	10

† The RMS noise in image is measured from the two-three hours of data using the full bandwidth (Ananthakrishnan and Rao, 2002).

2.3 Data Reduction

The Fourier inversion and image processing of the GMRT visibility data were done using the standard AIPS (version : 31DEC01) package. We converted the raw visibility data to FITS (*Flexible Image Transport System*) format using the gvfits (Chengalur,2003) program so that it can be read into AIPS. Before the conversion into FITS, the raw visibility data (available in 'LTA' format) was checked using the locally developed plotting tools to find out the bad data that occurred due to the non-working antennas, bad-baselines, RFI lines in the bandpass, the malfunctioning of the systems during the high wind speed and the ionospheric effects like strong amplitude scintillation. While converting the LTA data into FITS format, the bad data were filtered out by editing the input file for the gvfits program to specify only the working antennas and the number of good scans during which the visibility data was correct. The FITS file was generated with the (u, v, w) co-ordinate system chosen at the equinox J2000. The FITS file was then imported to the AIPS using the AIPS's task FITLD. The UV dataset was then sorted in time-baseline order by UVSRT task. The index table (NX) to assist the fast access to the UV-data set, and the null calibration table (CL) created with the help of INDXR task. Since the first and last record of each scan may be corrupted or may have wrong time stamps, these records were flagged using the QUACK task. The bad-baselines found by inspecting the raw visibility data were flagged by using the UVFLG task. The values of the flux densities for the primary and secondary calibrators in the source table (SU) attached with the FITS file were reset to zeros in order to avoid the wrongly boot-strapping of the observed quantities in the calibration steps. After resetting the information in the source table, the absolute flux density values of the primary calibrators at the observing frequency were set using the SETJY task which calculates it according to Perley coefficients derived from the VLA observations in 1999.2.
As we were interested only in the continuum information, the 128 spectral channel data could be collapsed to form the single channel continuum data base, but before

Table 2.2: observation table

I.	NGC 2997			
1.	Observing Band (MHz)	325	610	128
2.	Observing Date	Feb 25th,2004	Jan 22nd,2003	Aug 16t
3.	Pointing (2000)	←——	09h45m33.0s -31d10'28.0"	—-—
4.	Correlator Used (USB/LSB)	USB	USB	LSI
5.	Net Observing $time(Hrs.)^a$	4.86	3.41	2.8
6.	Receiver Bandwidth (MHz)	16	16	16
7.	No. of IFs	1	1	1
8.	No. of $antenna^b$	27	24	28
9.	Shortest spacing(kλ)	0.06	0.120	0.25
		$\sim 55m$	$\sim 60m$	~ 58
10.	Longest spacing(kλ)	27	40	101
		24.93 km	20.00km	24.18
11.	Flux density calibrator(s)	3C147,3C286	3C147,3C286	3C147,3
	Flux density in $(Jy)^c$	52.69,25.96	38.26,21.07	23.69,1
12.	phase calibrator(s)	0837-198,0902-142	0837-198	0837-1
	Flux density in $(Jy)^d$	$13.34 \pm 0.401, 4.30 \pm 0.137$	8.75 ± 0.07618	$4.66 \pm 0.$
II.	NGC 4565			
1.	Observing Band (MHz)	325	610	1280
2.	Observing Date	Aug 15th,2004	Feb 6th,2002	Sept.28th,2
3.	Pointing (2000)	←——	12h36m20.8s +25d59'15.7"	—-⟶
4.	Correlator Used (USB/LSB)	USB	USB	USB
5.	Net Observing $time(Hrs.)^a$	5.36	4.85	4.5
6.	Receiver Bandwidth (MHz)	16	16	16
7.	No. of IFs	1	1	1
8.	No. of $antenna^b$	27	25	24
9.	Shortest spacing(kλ)	0.06	0.08	0.410
		$\sim 55m$	$\sim 39.22m$	$\sim 96m$
10.	Longest spacing (kλ)	29.4	54	88
		26.18km	26.47km	20.62 km
11.	Flux density calibrator(s)	3C147,3C286	3C286	3C147,3C2
	Flux density in $(Jy)^c$	52.69,25.95	21.061	23.66,15.4
12.	Phase calibrator(s)	3C287	3C287	3C287
	Flux density in $(Jy)^d$	16.31 ± 0.05030	11.93 ± 0.14960	7.23 ± 0.11

a. Total observation time on the object before editing, b.Maximum number of antenna operational at any time during the observation, c.Set by SETJY task : / Using (1999.2) VLA or Reynolds (1934-638) coefficients d. Flux density and error from GETJY

collapsing of the channels of line data, corrections are needed for the channel or frequency dependent instrumental gain variations across the band which occur due to the antenna based band shapes or the filter response, and due to the residual fixed delay errors. Therefore, the bandpass calibration was the first operation done on the line data which is explained below.

2.3.1 Bandpass calibration

The bandpass calibration is used to determine the relative instrumental gain response across the spectrum, which is generally more stable in time as compared to the single channel instrumental gain variation with time (due to the temporal variation of the atmosphere). The bandpass calibrator is preferred to be a strong point source whose flux density is constant across the spectrum so that it can reveal the complex gain variation of the antenna as a function of spectral channels. One could apply the bandpass corrections to the baseline based passbands, but for a large array like GMRT there are 435 baselines, hence the baseline-based bandpass response function is decomposed into the antenna-based complex bandpass function using a *least-square method*. The standard procedure used in the BPASS task is to divide the spectral data by a source model or "channel 0" (generally vector average of RFI free channels in the observing band or the channels from central 3/4 portion of the total band). Since the *channel-0* division removes *source structure and atmospheric gain errors* across the band and reduces the source to the pseudo point source, the gain calibration of *channel-0* before determining the bandpass is not required.
As the observing band at low frequencies contain lots of strong RFI lines, the *channel-0* obtained by vector averaging may have poor signal to noise ratio resulting in less number of good gain solutions as a function of frequency. Hence, instead of *channel-0* division method for the bandpass calibration, we selected the bright calibrator which is spectrally flat. Then, first the gain calibration was done on these sources in time domain (which is discussed in next sub-section) using only two to three adjacent good channels which have no RFI lines through out the observation. The calibration table (CL) obtained by applying the antenna dependent complex gain solutions in time on the flux calibrator itself, is used to remove the frequency independent atmospheric gain errors across the channels. Most of the residual complex gain errors across the spectrum were purely due to the antenna based bandpass response functions which can be factorized into antenna-based bandpasses. This was achieved by setting the BPASS parameter option BPASSPRM(5)=1 . The BPASS task stores the antenna dependent bandpass response funtion in bandpass table (BP) attached with the uv-dataset.
The antenna dependent bandpass solutions for each polarization (RR or LL) stored in the BP table were checked using the POSSM task with the option APARM(8)=2. Also, the baseline based cross-power spectrum for each polarization were checked by applying the gain calibration from the CL table and the bandpass corrections from the BP table using the POSSM option DOBAND=2 (which selects the nearest bandpass solutions in time for the data points being corrected). The amplitude of the cross power spectra was found equal to the flux of bandpass calibrator, and the phase

across the band was close to zero. By studying the POSSM outputs of bandpass table spectra and cross power spectra, the different kinds of RFI lines appearing from the central square and arm baselines were flagged using the SPFLG task which shows all the spectral channel of individual baseline with time. After flagging the RFI lines and bad channels, the bandpass calibration was done iteratively until a good bandpass solution was obtained, i.e. normalized amplitude of the antenna bandpass around one, and the constant or the smoothly varying bandpass phase.

Averaging spectral line data in frequency :

The SPLAT task was used to vector average the spectral line data to form a continuum data base. Before the averaging of channels, only the bandpass solution table (BP) was applied to correct for the slowly varying channel dependent complex gain of the antennas. As the phase calibrators at the 325 MHz and 610 MHz observing band were quite strong enough to determine the antenna dependent bandpass solutions (refer 2.2), we also used them for the bandpass calibration. Hence the antenna dependent bandpass solutions found on each calibrator scan were interpolated in time, and applied to the target source by using the DOBAND=3 option of the SPLAT task. The single channel continuum data base formed at low frequencies by averaging all the 128 spectral channels from the line data may degrade the quality of map due to the bandwidth smearing effect. The bandwidth smearing effect in image plane is nothing but the radial smearing of the source, and it increases with the distance from the phase center. To avoid the bandwidth smearing effect, the line data at 610 MHz and 1280 MHz observing band was collapsed to five channels by averaging each adjacent 20 or 22 channels, and ten channels were formed by averaging each adjacent 10 channels of 325 MHz data. The first five to six channels and the last ten channels of the band for each observing band were discarded in the bandpass calibration procedure itself.

At this stage, before using the SPLAT task, we scrutinized the spectral line data baseline by baseline to find out the strong RFI lines using the POSSM and SPFLG task by applying the bandpass table, and the data were flagged using the SPFLG task which allow flagging by accepting the range of baselines for each stoke parameter and the clipped values based on the displayed visibility amplitudes or the RMS of the visibility amplitudes.

2.3.2 Gain Calibration

Primary point source calibrator observed at the phase center by an interferometer gives constant visibility amplitude, and its visibility phases are zero regardless of the baseline distance. The values of the observed visibilities may depart from the constant amplitude & zero phase thereby giving direct estimates of the corrections required for ionospheric and instrumental gain fluctuations. The determined corrections are the complex quantities referred to as the *complex gains* which can be obtained by dividing the observed visibilities by the true or known visibilities for the calibrator source. Therefore, to determine the unknown complex gains per baseline, one has to solve $\frac{1}{2}N(N-1)$ gain equations for an N element interferometer (435 baselines in case of GMRT array). Since most of the data corruption takes place before the

correlation, the baseline-based gain can be factorized into antenna based gains, in which ionospheric gains are also decomposed as antenna based complex quantities. The observed visibilities obtained from the correlator output therefore can be written as:

$$V_{ij}^{obs} = G_i G_j^{\star} V_{ij}^{true} + \epsilon_{ij}$$

where, $V_{i,j}^{obs}$ is the observed visibility by baseline (i,j) formed by an antenna pair i and j, the G_i & G_j are the complex gains of the antennas i and j, and ϵ is the additive noise on the baseline (i,j). Thus, instead of determining $\frac{1}{2}N(N-1)$ unknown complex gains for the N antenna interferometer, the N unknown antenna dependent complex gains can be extracted from the baseline based gains by solving the set of equations $G_{ij} = V_{ij}^{obs}/V_{i,j}^{true} = G_i G_j^{\star}$. This set of equations remains true even if we subract the phase of one G_i from all the G_j, where the phase of G_i becomes zero which is known as the *reference antenna*. Therefore, there are $2N-1$ quantities (N amplitdues, N-1 phases) to determine, which can be extracted from the $N(N-1)/2$ complex equations using a *non linear least square* technique.

The CALIB task of AIPS was used to determine the antenna based complex gains as a function of time from the observed visibility data on calibrator sources. The gain solutions found at the time of calibrator observations were then interpolated in time to the target source observations. The sequence of tasks (including the CALIB) required to accomplish the gain calibration are discussed briefly here.

1. Determining the antenna gain solutions : To determine the antenna-dependent gain solutions, the CALIB task accepts a number of input parameters called *adverbs*. Some of the essential adverbs are discussed here : (i) The CALIB task was run on the continuum data base by providing the multi-source input uv-file which was obtained by averaging the spectral line data after the bandpass calibration (as discussed in the previous section). (ii) Since both the primary and secondary calibrators were having high flux density values (see table 2.2), all the calibrators from each observing data set were specified in CALSOUR adverb. (iii) The reference antenna was selected using the REFANT adverb by considering the selection criteria of good signal to noise ratio, availability of the antenna throughout the observing session and free from gain jumps, etc. (iv) The phase calibrators are not always perfect point sources, but it depends on the length of the baseline, resolving of the point source by the long baselines or for very short baselines the extended structure becomes apparent. The UVRANGE adverb allow us to select only those baselines for which the calibrator source is strictly a point source. For this purpose, the plot of the visibility amplitudes against the uv distance ($\sqrt{u^2+v^2}$) were checked using the UVPLT task. It was found that none of the primary or secondary calibrators used for the gain calibration of each observing data set showed any significant structure for the short baselines or any drop in visibility amplitude for the long baselines. (v) The SOLINT adverb controls the solution interval in minutes over which the data is averaged before solving for the antenna gains. Normally, the value of SOLINT is given by assuming that gains are constant during the solution interval. Therefore, the data are averaged over each calibrator scan which is generally only of four to six minutes duration. But to take care of poor phase stability data, the SOLINT value was set to one minute. (vi) The solution type (SOLTYPE) by default uses the normal least square algorithm

to solve the calibration equations. In the case of a large number of failed solutions, the SOLTYPE was set to 'L1' solution, in which the modulus of the difference of the model and data is minimized instead of the square of the modulus. The 'L1' type solution is more tolerant of errors. (vii) The MINAMPER and MINPHSER adverbs were set to 10% and 20 degrees respectively, so that the CALIB can report the diagnostics on individual baselines only for the residual amplitude errors which are greater than 10% of the source flux density, and the residual phase errors which are in excess of 20 degrees from the model phase. These ranges of the residual errors were allowed because of the difference in the sensitivities of the antennas and short term phase variations. The residual errors often called as amplitude closure error and phase closure error.

Since we did not use any external source model or the external BP calibration table while gain calibrating the continuum data base, the DOCALIB and DOBAND options were disabled by setting their value to -1. The SOLMODE option was set to 'A&P'; therefore, the CALIB task solved the gain solutions for both the amplitude and phase. The CALIB creates a new SN table for each run of the gain calibration to store the determined antenna dependent complex gains, or overwrites the existing SN table each time if we provide the same SN table number. The CALIB task reports the number of good solutions found on the visibility data of calibrator sources and stores the two sets of antenna dependent complex gains for both the RR and LL polarization data. The SN table was carefully checked by plotting the antenna gains using the SNPLT task to find out the sudden jumps in gains (amplitude or phase) of the antennas. If it is found in all the antennas, then the phase referencing antenna were checked and changed to some different antenna, and the gain calibration was re-run using the reference antenna free from gain jumps.

2. GETJY : The absolute flux for the primary calibrators were registered in the source table (SU) using the SETJY task, but the flux density values for the secondary calibrators were assumed to be 1 Jy while solving for the antenna gains in CALIB. Hence, the task GETJY was used to work out the flux density of secondary calibrators. GETJY uses the flux densities of the primary calibrators stored in the SU table and the amplitude gain solutions stored in the SN table for the primary and secondary calibrators. After determining the flux densities for the secondary calibrators, the GETJY alters the amplitude solutions (found on secondary calibrators) in the SN tables so that it becomes appropriate with the newly calculated flux density values of the secondary calibrators.

These flux density values with uncertainties are listed in the table 2.2. It is seen that these values are close to the values listed in VLA calibrator manual.

3. Interpolation of the gain solutions : The CLCAL task was used to interpolate the antenna gain solutions derived from the calibrator sources to the target source. The OPCODE adverb was set to 'CALI' which merges the selected good solution tables, smooths it, and applies it to the previous CL table so that the gain solutions can be incrementally improved. But in the first step of gain calibration procedure, it takes the CL table 1 produced by the INDXR task (which has all ones and zeros for the amplitudes and phases), and uses it as a template to set the time interval for the gain solutions on the target sources as well as on the calibrator sources. The

resultant interpolated solutions were written in the higher versions of 'CL' table.
To check the validity of the determined antenna gain solutions on calibrator sources, each calibrator scan was calibrated with the gain solutions obtained from that scan itself. After this, the gain calibrated data on the calibrator sources should show the visibility amplitudes equal to the flux density of calibrators, and the visibility phases should be zero as expected on the point source. For this purpose, the adverbs SOURCE and CALSOUR were set to *primary/secondary calibrators* (Ref. table 2.2), and the INTERPOL adverb was set to 'SELF' which causes the nearest solutions in time to be selected for the specified calibrators, or the antenna gain solutions obtained from the calibrator itself which we are trying to self-calibrate. Later, the CLCAL was re-run with the adverbs SOURCE='*target source*', CALSOUR='*secondary calibrator*', and the INTERPOL option was set to '*2pt*' which does the two point linear vector interpolation between the antenna gain solutions found on the two sequential calibrator scans, so that the resulting interpolated gain solutions in time can be applied to the target source.
The gain calibrated visibility data of the calibrator sources were checked using the UVPLT task. It was found that the visibility amplitudes were reasonably distributed around the flux density values of the primary calibrators and the secondary calibrators which were registered in the SU table by the SETJY and GETJY tasks respectively, and the phases were close to zero irrespective of baseline lengths. The spread of visibility amplitudes on primary calibrators was around 4% at 1280 MHz, 9% at 610 MHz and 15% at 325 MHz, and the spread in phases was 2% to 5% for 1280 MHz to 325 MHz. This spread was allowed as the variation in antenna sensitivities, residual baseline based noise, and the residual short term phase variations.
If the gain calibrated data on the calibrator sources shows bad data: for example, if amplitudes are not close to the expected flux densities or the phases are not within some assumed range, then the bad data was flagged using the various flagging tasks like TVFLG or UVFLG. With the help of these flagging tasks, the required time range or any particular baselines can be selected. The individual polarization data was flagged. In this way, the whole gain calibration procedure was repeated again till a good solution is found.
4. SPLIT : At this stage, we applied the gain calibration table resulting from the CALIB procedure. The SPLIT task was used to apply the selected gain calibration table to the target source data by setting the adverbs DOCALIB=*true* and GAINUSE=(CL table number). The SPLIT applies the calibration directly to the visibilities on the target source, and creates a single source UV-data file, so that it can be used for further image processing.
Before going for the imaging, the visibilities on the object were carefully examined by using the UVPLT and VPLOT tasks to look for the bad baselines where the visibility amplitudes are sporadic or having isolated bad points in the time series. These bad data were flagged by using the TVFLG and UVFLG tasks. In addition IBLED task was extensively used to edit out the visibilities on the individual baselines in time domain.

2.3.3 IMAGR

The Fourier inversion of the gain calibrated visibility data of target source was achieved by the IMAGR task. The IMAGR task of AIPS has multi-capabilities, in addition to weighting, gridding and fourier transforming the visibility data to produce dirty beam and dirty map, it also does the multi-field imaging where the re-projection of the (u,v,w) co-ordinates as well as the phase rotation of the visibility data to shift the tangent point to each field center is possible. The deconvolution of each field was done by the enhanced version of CLEAN algorithm by Cotton and Scwab which is implemented in the IMAGR task. The imaging theory and the strategies in imaging procedure to map the NGC 2997 and NGC 4565 has been discussed in detail in Chapter-3; here we are emphasizing the way IMAGR was used while mapping the objects for this thesis.

1. Low resolution map : The first low resolution map of $\sim 45''$ was tried to find out whether the diffused emission could be guessed reliably. The map was obtained by applying a Gaussian taper to (u,v) plane which suppress the high resolution information on the longer spacings. The adverb UVTAPER$\sim$5 Kλ was set to specify the widths in U & V directions of the Gaussian function. In addition to this, the UVWT adverb for density weighting function was set to *natural weighting* which improves the sensitivity on shorter baselines and gives a broader synthesized beam. In order to find any strong confusing sources in the primary field as well as near it, each time the bigger image size was used than the primary beam area. Size of the image was set using the adverbs IMSIZE (number of pixels) and CELLSIZE (pixel separation in arc second).

2. Cleaning : While deconvolving the image in the IMAGR task, the boxes can be put around the obvious strong sources in the image plane by using the graphical interface given on AIPS's TV. This provides apriori information about the sources where the CLEAN searches for clean components (the pixels with the maximum brightness), and the GAIN adverb decides the fraction by which peak value is subtracted (Highest peak$\times$dirty beam$\times$gain) from the residual image. Initially, the sidelobes of the obvious strong point sources were removed by fitting the small CLEAN boxes around it, and using the adverb GAIN=0.5. First few clean iterations were tried up to a certain noise level, and boxes were put interactively around the sources as they become visible.

As the structure of low surface brightness distribution of the object started appearing after more than 500 clean iterations on the strong background sources, the clean loop gain was lowered to GAIN=0.03, so that the large number of clean components can be obtained on the extended object. Because the first clean iterations were dominated by the bright and sharp components of the source, some negative and erroneous clean components were also accepted (which CLEAN compensate later on) so that the cleaning on the low surface brightness area becomes possible.

The number of clean iterations continued till the brightest pixels in the residual image reaches to some multiple of r.m.s. noise level ($\sim 3\sigma$) or the cumulative sum of CLEAN components (total CLEANed flux density) reaches down to a roughly constant number. This indicates that there are no further sources in the residual map to clean. The

total number of clean iterations ∼40000 was tried to clean deeply on the extended object to model the lowest level intensity flux, and to get a high dynamic range map. The IMAGR stores the accumulated clean components with its flux values (Jy) and X-Y positions (arcsec), which are finally added back to the residual noise image by convolving all the clean components with the *clean beam*. The clean beam is nothing but the elliptical Gaussian with a FWHM equal to that of the synthesized dirty beam and free from the confusing side lobes.

3. Multi-field Imaging : The large number of strong background sources in the primary field at 325 MHz and 610 MHz limits the dynamic range of the map at higher resolution and distorts the image due to the increasing phase errors away from the phase center because of the w-term effects. Therefore, multi-field imaging was necessary to alleviate these effects. The *faceted transform* algorithm was used to do the multi-field imaging which is explained in section 3.7, where it does the 2-D approximation by shifting the phase center across different parts of the image which contains the localized bright sources. The small field around the shifted phase center gets cleaned independently with different dirty beams for each field. The SETFC task was used to create a number of fields called *facets*, which are then interpolated on a common tangent plane with respect to the pointing phase center of the target source by using the FLATN task. In the IMAGR task, the number of determined fields by the SETFC task was specified using the NFIELD option. The number of facets for the NGC 2997 at 610 MHz and 325 MHz was around thirteen and twenty-two respectively, and for NGC 4565 it was around seven and thirteen respectively. In this case, we set the IMAGR adverb DO3DIMAGE=1 which took care of shifting the tangent point (re-projection of u, v, w co-ordinates) to each field center so that each field can be approximated as a 2-D tangent plane to the celestial sphere. During the clean iterations, the side lobes of sources found in one field are not subtracted from the other overlapping fields because this causes the side lobes of strongest source to be taken as real source during the clean major cycle. To prevent this, the OVERLAP=2 option was set so that the strong source and its side lobes can be removed from the later overlapping fields before they are imaged.

2.3.4 Self-Calibration

In ordinary gain calibration using the external calibrator sources, the antenna dependent gain corrections applied to the visibility data of the target source may not remove the instrumental and ionospheric gain errors completely, because the gain corrections are obtained by interpolating the antenna based gain solutions which are determined from the visibility data of the calibrator sources taken at different times by interspersing the observation of calibrator source during the observation of target source. Also, there are atmospheric/ionospheric gain changes which are dependent upon the position of the calibrator and target source; some times it is a bit difficult to find a calibrator source close to the target source so that it lies in the same isoplanatic patch[2]. Therefore, gain calibration by the external calibrators removes the phase

[2]The ionospheric patch over which the phase variations are the same.

errors only partially and there will be always residual complex gain errors on the target source. The self-calibration method corrects the observed visibility data of the target source by the antenna based complex gain solutions obtained using the model visibilities. The model visibilities are obtained by fourier transforming the assumed model for the target source under some constraints in image plane like positivity of the brightness for the total intensity map, and the confinement of the source structure in image plane.

The aim of the self-calibration method is to improve the source model of the brightness distribution such that its fourier transform after corrections of some elemental gain errors should reproduce the observed visibilities within some noise level. This can be achieved by an iterative approach in which the source model is formed by the *clean components* obtained from the CLEAN deconvolution method, and the observed visibilities of the source are corrected by the antenna dependent complex gains which are found using the model visibility data. This is exactly implemented in the method suggested by Schwab (1980), where the sum of squares of residuals is minimized.

$$S = \sum_{i,j\ i\neq j} |\chi^2_{ij} - G_i G^*_j|^2 \omega_{i,j} \qquad ; \text{where, } \chi_{ij} = V^{obs}_{ij}/V^{model}_{ij}$$

Where, ω_{ij} weights applied which are inversely proportional to the variance of the baseline based noise. In the χ^2_{ij} term, observed visibilities are divided by the model visibility so that it will be independent of the source structure, and residuals are nothing but the product of two antenna dependent complex gains from which antenna based gains can be determined[3]. The usual procedure for self calibration to be followed is to select the initial model for the source by putting image constraints achieved by the CLEAN deconvolution method, divide the observed visibilities on the source by the model visibilities, determine the antenna dependent complex gains solutions so that the observed visibilities can be corrected using it and evolve the new model of the source from the corrected visibility data set. This procedure was repeated till the process converges i.e. a number of good solutions is obtained, and the source image is improved resulting in a higher dynamic range for the map.

Another aspect of removing the antenna based phase errors used by Roger Jannison where the Fourier phases of the source are recovered by taking the appropriate sum of the observed visibility phases on the source from three closed loop baselines called, *closure phase*.

$C^{obs}_{ijk} = (\phi^{true}_{ij} + \phi_i - \phi_j) + (\phi^{true}_{jk} + \phi_j - \phi_k) + (\phi^{true}_{ki} + \phi_k - \phi_i) + (\text{noise term}) = C^{true}_{ijk}$

To use this method to recover the phases (known as hybrid mapping), a source model by CLEAN is used to provide estimates of the true phase on two baselines and derive the phase on the third baseline in the loop from the observed *closure phase* and the new model is formed from the observed visibility amplitudes and the *predicted visibility phases*.

The self-calibration method derives the antenna based phase errors explicitly rather than baseline based corrections by enforcing the constraints on source structure using the CLEAN deconvolution method. The self-calibration converges faster as the ratio of visibility constraints to N unknown gains ($\frac{N-2}{2}$ for phases and $\frac{N(N-3)}{2(N-1)}$ for

[3]See the internal technical report *Computation of Antenna Dependent Complex Gains* by Sanjay Bhatnagar (1999).

amplitudes) increases with the the number of antennas. This algorithm was quite advantageous for the visibility data given by an array like GMRT. In our case the number of antennas used for the observation was around 27, and the source structure was well represented by a small number of degree of freedom (CC components in clean) since it was oversampled by many more short baselines. This also completes the basic requirements of self-calibration like the total number of degree of freedom (the number of free gains to vary plus the number of free parameters in the model of sky brightness distribution) should not be greater than the number of independent visibility measurements.

Implementation : Although the self-calibration procedure is simple for computation and deals with the antenna based residual complex gain errors which are mostly related to the ionospheric phase errors, there are a large number of free parameters which can degrade the performance of self-calibration. Therefore, a general procedure is evolved by considering the practical problems while using the self-calibration to improve the image. For rapid convergence of self-calibration, it is important to provide a good model of the source formed by clean components. To reject the unsatisfactory features in the model that are contributed by wrong clean components like negative clean components which are occurring due to the calibration errors, the source model provided in the first few iterations of the self-caliration procedure was formed using the positive clean components only. This was specified using the NCOMP adverb where the positive clean components above the first negative component from the CC (clean component) was used. The constraint for confining the structure was achieved by fitting clean boxes around the source structure. The sparse point source components given by very short baselines poorly represent the model for the diffused emission in case of extended structure. To get the correct estimations of the gain errors, short baselines up to 0.2 to 0.4 kλ was avoided in the first few iterations of phase self-calibration. Also, the longest baselines formed by the last array elements have poor phase calibration. In order to get the initial model, the longest baselines were constrained by using the UVRANGE adverb. Since the calibration errors are mostly due to the ionospheric phase errors, and the model fitting for phases may poorly fit for the amplitudes, the self-calibration was tried to solve the gain equations only for the phases by specifying the solution mode adverb SOLMOD='P'. While computing the gain corrections, the SOLINT adverb was an important control parameter to set the time resolution for solution interval (in min.) over which the model and the visibility data are averaged by assuming that the gain changes are constant. Initially, when the calibration was done using a strong point sources model where phases are stable, it was set a bit longer like two to four minutes, but to eliminate the shorter scale phase fluctuation caused by the ionospheric effects while calibrating using the source model, we set the solution interval time to be about one minute. After determining the gain corrections at finer time step using the source model, or in the case of bad solution occurrence, solution interval was increased to get a higher signal to noise ratio on all the baselines in the case of weak sources, so that the variance of computed gain corrections are acceptably small.

The standard self-calibration procedure used in the case of all the data sets of the object NGC 2997 and NGC 4565 was as follows :

(i) Firstly, the strong confusing sources at the edge of the primary beam were removed (see section 3.5). The faceted algorithm was used to clean each individual facets. (ii) Self-calibrate the visibilities using only the strong point sources near or within the inner quarter of primary field. For this purpose, high flux clean components obtained using a few clean iterations around 500 to 1000 were used. The SOLINT was set around 2 to 4, and the gains were solved for *phases* only. After two to three iterations using only point sources, the source model obtained by cleaning, up to the rms noise level of the map, was included for self-calibration. The visibility data was phase self-calibrated with the solution interval of one minute, with appropriate uv-range to avoid the shortest baselines. To get the correct phase gain solutions for the above iterations a more conservative approach was tried by restricting only the positive clean components representing 50% to 80% of total cleaned flux included in the model above the first negative component. iii. Finally, as the convergence of self-calibration started occurring, the target source was cleaned deeply with low loop gain values, so that a large number of components gets collected, and using all of them with the larger SOLINT, self-calibration was tried again to get a smoother structure of low surface brightness. Also, the self-calibration with the box and without box was tried to check for low level flux features of the source near the noise level.
NGC 2997 at 1280 MHz was having weak features with poor signal to noise ratio and hence self-calibration was not tried on this data set. At 610 MHz, although the clean components from each facet of the point sources within the beam was used, self-calibration on the model converged poorly and made no significant difference. At 610 MHz for NGC 4565, after four to five successive iterations, self-calibration convergence occurred. At 325 MHz, for both NGC 2997 and NGC 4565 data, it took around six to eight iterations to get good convergence of self-calibration resulting in improved high dynamic range maps.

2.3.5 Problems in the mapping

1. Flagging of bad visibilities : The visibility data on the point source calibrators is expected to have roughly constant amplitude and zero phases. Hence, irregular bad visibility data given by particular bad baselines were flagged. But in the case of a target source with complex structure, the bad data was checked after applying gain corrections (determined by an interpolation of good gain solutions obtained from the calibrator scans in the gain calibration step). Isolated high amplitude visibility points and sporadic visibility data given by bad baselines (due to malfunctioning of the antenna, correlator and the radio frequency interference, etc.) can cause strips and ring like structures in the image plane, which makes its appearance in the residual image even after deconvolution of the image. Such bad points and bad visibilities were spotted in the visibility plots by looking at the visibility amplitudes as a function of uv-distance or time and flagged. In the mapping plane, all sources were found to be below 2-3 Jy; therefore in the visibility plane, amplitudes above $\sim$10 Jy were considered as artificial amplitudes and clipped using the CLIP task. The intermittent narrow band radio frequency interference (RFI) often comes

during low frequency observations and for short baselines. As the GMRT visibility data acquired is in spectral line mode, it was possible to flag these individual strong RFI lines by using the FLGIT and SPFLG tasks. The graphical flagging tasks like TVFLG and IBLED were also used effectively to flag the bad data. The IBLED task shows the visibility function for individual baselines, and allow editing visibility data interactively so that an isolated bad visibility point can be found and flagged easily.

2. Removal of strong confusing sources : There were at least two to three strong confusing sources lying far from the phase center of the map at each frequency, near the edge of primary beam or outside of it (see section 3.5, and section 5.x), which were producing distortion across the map due to its sidelobes, and additional noise in image due to its incoherent sum of sidelobe response. To locate such sources, a low resolution map of larger size than the primary beam area was made by tapering the uv-plane. These sources and their effects were then removed using the UVSUB task which subtracts the clean components from the visibility data by fourier transforming it. The clean components of confusing sources were obtained by cleaning the field around each source separately and using the 3-D imaging where the phase center is shifted to each confusing source so that the distortion due to w-term effect can be reduced. Since the presence of moderately strong confusing sources in the mapping field dominates the signal on many baselines and makes it difficult to judge about the suspected bad-baseline data, the removal of strong confusing sources proved to be helpful in the case of identification of the bad baseline data.

3. NGC 4565 at 1280 MHz - Lack of Short spacings : The apparent radio dimension of edge-on galaxy NGC 4565 at 1.4 GHz is around $\sim 10.5^{'} \times 1.3^{'}$ (E.Hummel et al,1984). To get the sensitivity for such a large extended structure, the shortest spacings required at GMRT is around ~ 76 meter. But in our case, NGC 4565 observational data at 1280 MHz was having the shortest spacings range above ~ 0.410 kλ (96 meter), which is sensitive to only emission of angular scale $\sim 8^{'}$. There were only seven baselines present in the range of 621 kλ to 1000 kλ. As a result, the apparent observed dimension was only of the order of $5.9' \times 0.83'$, and the total flux density measured was 72 mJy, which is less than expected.

Chapter 3

Imaging of NGC 2997 and NGC 4565

The imaging of low surface brightness objects like NGC 2997 and NGC 4565 becomes difficult at low frequencies due to the various sensitivity limiting factors like strong confusing sources in the large primary field of view, non-coplanarity of baselines and radio frequency interference etc.
To get the unique image with the high dynamic range and fidelity, the prior assumption about the instrument and the source is required. The apparent brightness of extended emission region in an image depends on the resolution element of the telescope, so the synthesized beam of telescope should be such that an extended structure is detectable while considering the total integration time required to achieve the brightness sensitivity or the rms noise in image. The details of observing parameters are given in table 2.2 of chapter-2. Other factors affecting the map of extended object depends on how the visibility data sampled by the observation (uv-coverage), weighting and tapering function applied to the visibility data at the imaging stage.
In the prior assumptions for the total intensity mapping, we have consider the sky is positive, brightness distribution for the extended object is connected, and the brightness distribution is limited to the convenient box on the sky, which is the basic assumption for the image reconstruction method.
The imaging procedure used to obtain the map using the AIPS software package by NRAO requires a basic understanding of the algorithms implemented in AIPS, their effects and the interaction between the input or control parameters. The data analysis is not automatic but requires special treatment depending on the observing frequency, observing field around the object, atmospheric effects, and the bad data occurrence because of the instrumental effects, and radio interference in the observing band.
Although, the theory about imaging briefly discussed in this chapter is available with the details in many reference books, the discussion has been mainly emphasized on the imaging procedure using the AIPS to map the NGC 2997 and NGC 4565. A few experiments have been tried using the GMRT data to explain how to process the visibility data for the mapping and why. The bad data flagging and calibration is discussed in the previous chapter, hence the discussion in the next section starts with the imaging of the visibility data.

3.1 Imaging

A visibility $V(u,v)$ is a continuous complex function which represents the Fourier transform of the true sky brightness distribution $I(l,m)$. Due to the finite number of antennas and finite amount of time for the observation, in practice, an interferometer samples the visibility function or spatial coherence function only at certain locations in the (u,v) plane, called uv-coverage. Therefore, there are always gaps or holes in the measurement of the visibility function, and also these visibilities are corrupted by the thermal noise due to the receiver and ionosphere. The sampling function of the aperture synthesis array is given by

$$S(u,v) = \sum_k \delta(u-u_k, v-v_k)$$

where, the summation is over all the baselines.
Thus, the aperture synthesis array provides the sampled visibility function $S(u,v)V(u,v)$ as the actual data. The inverse Fourier transform of the sampled visibility function gives the *dirty image* $I^d(l,m)$

$$I^d(l,m) = \iint S(u,v)V(u,v)e^{2\pi i(ul+vm)}du\,dv \tag{3.1}$$

Here, we have approximated the 2-D Fourier transform relationship between the spatial coherence function $V(u,v)$ and the source surface brightness $I(l,m)$ by assuming the small field of view for the imaging $|\pi(l^2+m^2)w| \ll 1$, and absorbing the primary beam pattern factor *A(l,m)* in to $I^d(l,m)$.
Using the *Convolution theorem*, above equation (3.1) can be re-written as

$$I^d = \mathbf{F}(S \cdot V) = \mathbf{F}(S) \star \mathbf{F}(V) = B(l,m) \star I(l,m) \tag{3.2}$$

Where '$\cdot$' represent the multiplication, '$\star$' is the convolution and 'F' denotes the Fourier Transform. The Fourier transform of sampling function $S(u,v)$ is known as the *dirty beam* $B(l,m)$, which is nothing but the instrumental function depends on the uv-coverage. It is also known as the *point spread function* since for a point source of unit amplitude at the phase tracking center $\delta(l_0,m_0)$, the visibility function will be $V(u,v) = 1+0i$ everywhere.
The equation (3.2) shows that the dirty image is a convolution of the dirty beam with the true sky brightness distribution.

3.1.1 Dirty Beam

The synthesized beam is an elliptical Gaussian fitted to the main lobe of the *dirty beam*, which determines the resolution of the telescope. For the point source, flux density per synthesized beam is independent of the size of synthesized beam, where as the apparent brightness of extended emission in the dirty image is depends on source structure itself and the beam width of synthesized beam.
While mapping the NGC 2997 and NGC 4565, it was necessary to map the low level brightness structure with enough signal to noise ratio and also the high resolution components in diffuse emission like hot spots, star formation regions in spiral arm of NGC 2997, and the compact components along the major axis of NGC 4565. It

was desirable to have a high-resolution as well as low-resolution maps of NGC 2997 and NGC 4565 to check the reliability of high and low resolution components. Also, there was need to make the maps with a similar resolution in the various bands from 325 MHz to 1280 MHz for the study of inter frequency comparison. The maps shown with different resolution in section 4.1 is obtained by changing the beam width of the synthesized beam by controlling the shape of dirty beam.

The shape of the dirty beam can be controlled by weighting the sampled visibility data. A weighted, sampled visibility function (V^w) is a multiplication of the sampled visibility function with the weighting functions.

$$V^W(u,v) = \sum_k T_k\, D_k\, \delta(u-u_k, v-v_k)\, V(u,v)$$

Where, T_k is known as uv-tapering function, and D_k is the density weighting function, the significance of both the functions are described below briefly.

1. Tapering function : Tapering function is a smoothly varying function of (u_k, v_k) which is used to downweight the visibility information at the edge of uv-coverage, because the long spacings sample the visibility function sparsely, and produce small-scale variations in the dirty map.

Often a Gaussian taper $T(u_k, v_k) = exp[-(u_k^2 + v_k^2)/s^2]$ is applied to the (u, v) plane, where s is a measure of the width of the taper.

While mapping at each frequency, we made a low resolution map first to make a diagnostics of the confusing sources, and to identify the low surface brightness areas in the region of interest by strongly tapering the visibility data beyond the $\sim 5k\lambda$.

2. Density Weighting function : The density weighting function can change the relative proportion of the weights applied to the uv-points. During long run of continuum observations, since the short spacings near the origin changes slowly in (u, v) plane, the aperture synthesis array over samples the short spacings near the center of (u, v) plane than long spacings. In *natural weighting* ($D_k = 1$) all the samples in uv-plane are weighted by their input weights specified by the inverse square of its uncertainty. Therefore, while taking the local average of visibility samples within a specified area around each (u_k, v_k), the array becomes more sensitive to the visibility data from the short spacings, which yields a broader dirty beam with the better signal to noise ratio. The natural weighting is preferred while mapping the weak compact sources, it also helps to map the extended emission smoothly by minimizing the negative inner sidelobes.

In *uniform weighting* ($D_k = \frac{1}{N_k}$), each visibility is weighted by the inverse number of visibilities N_k in a specified area around a grid point, called cell (which is explained in next subsection). Since the lightly sampled isolated cells gets comparable weight with respect to those heavily sampled regions, the sampling function appear to be uniform over the (u, v) plane, and gives the narrow dirty beam. Using the uniform weight we get a high resolution map, but with the reduced signal to noise ratio, and the resulting beam size is mostly depend on the tapering function.

As per the requirement of mapping of extended object with its high resolution components embedded in an extended emission, it needs to compromise between the uv-tapering (*close to natural weighting*) which down-weights the longer spacings and uniform weighting which down-weights shorter spacings. The ROBUST parameter

in AIPS can be used to get result which lies between pure natural and pure uniform weighting, where uniform weighting is temper by adding a constant to the local density of weights.

3.1.2 Gridding

To approximate the dirty image $I^d(l,m)$ on a uniform grid of $(N \times N)$ pixels, the Fourier transform equation (3.1) is computed either using the *brute-force* method by evaluating the direct Fourier transform of M sampled visibilities at each point of an $(N \times N)$ grid, or using the *Fast Fourier transform* method, in which visibilities are interpolated onto a regularly spaced grid. The direct Fourier transform method is expensive for large M or N, since it requires $2MN^2$ operations or N^4 multiplications whenever $N \sim M$. The number of required operations can be reduced up to $N^2 log_2 N$ using the FFT algorithm efficiently, in this method the weighted sampled visibility data is convolved with some suitable function $C(u,v)$ centered at each grid point. Since the FFT requires regularly spaced data, the convolution is then re-sampled on regularly spaced grid of power two array size. The final re sampled visibility function is given by

$$V^R = R\,[(C \star V^W)] \rightleftharpoons \mathbf{F}(R) \star [c\,(\mathbf{F}W \star \mathbf{F}V)]\ (= \tilde{I}^d)$$

In practice, the function C is only a few grid cell wide, and truncated to a width of m cells, so that, for 1-D case, $C(u) \equiv 0$ for $|u| < m\Delta u/2$; where, Δu is (u,v) plane cell spacing. The useful griddling convolution functions include like pillbox (two-dimensional circular step), truncated exponentia , sinc and truncated spheroidal function, which are discussed with the details in NRAO notes on image synthesis.
In above equation, $R(u,v)$ is a re-sampling function, which is also known as bed of nails function

$$R(u,v) = \sum_j \sum_k \delta(j - u/\Delta u, k - v/\Delta v)$$

Where, Δu & Δv are cell size or the separation between grid points. Since the V^R is sampled on regular grid, we can use FFT to obtain the dirty image $\tilde{I}^d$, as mentioned in above equation. The FFT of re-sampled visibility data V^R effectively makes $\tilde{I}^d$ a periodic function of l and m with a period $1/\Delta u$ in l & $1/\Delta v$ in m. Therefore, the convolution with $\mathbf{F}(R)$ is the step that causes aliasing. To minimize the aliasing, the $\mathbf{F}(C)$ should fall to zero sufficiently rapidly outside the primary field of view $(1/\Delta u, 1/\Delta v)$. The default convolution function being used in IMAGR task is truncated spheroidal function whose Fourier transform c drops very rapidly outside the image.
Since the dirty map $\tilde{I}^d$ is multiplied by $c(l,m)$ in the image domain, the effect of convolution function can be removed by dividing the dirty map & the dirty beam by Fourier transform of convolution function $C(u,v)$.
The IMAGR task in AIPS is used for the weighting, griding and Fourier inversion of the visibility data to produce the *dirty beam* and *dirty image*. The actual region for mapping can be specified by the CELLSIZE and IMSIZE parameter given in IMAGR, where CELLSIZE is pixel separation in arcsec and IMSIZE is size of the image in pixels. As per Nyquist sampling, the cellsize Δl & Δm in image domain should be such that $N_l \Delta u = 1/\Delta l$ and $N_m \Delta v = 1/\Delta m$, where Δu & Δv is the width

of grid spacing in wavelength and Δl, and Δm in radians. For the effective clean process and higher dynamic range map, there should be at least three to four cell across the main lobe of dirty beam.

3.2 Image reconstruction

As mentioned in the previous section 3.1, the sampling function $S(u,v)$ of aperture synthesis array measures the noisy visibilities at the discrete location along the uv-tracks in aperture (u,v) plane. In the image domain, the Fourier transform of such sampling function resulted in the dirty beam $B(l,m)$ which is having the positive and negative sidelobes whoes amplitude can be greater than 10% of the peak. The convolution of the true image with the dirty beam having sidelobes gives the *dirty image* or *principle solution* which has the rumble of sidelobes around the strong point sources and unphysical negative brightness and artifacts, because of this the rms noise in the dirty image increases which is more than the thermal noise present in the image due to the receiver system.

$$I^d(l,m) = B(l,m) * [I^{true}(l,m) + \eta(l,m)]$$

where, $I^d(l,m)$ is the dirty image , $I^{true}(l,m)$ is the true image and η is the noise in the image.

Image reconstruction is used to recover the true image through the various deconvolution schemes. Deconvolution algorithm removes the sidelobes present in the image plane and in doing so estimates the visibility function at spatial frequencies in the unsampled part of the (u,v) plane.
In linear deconvolution, by taking the Fourier transform of the above equation and then dividing by the transfer function $S(u,v)$, one can do Fourier inversion again to recover $I(l,m)^{true}$. But in case of the poor signal to noise ratio, the final term $\eta(l,m)$ in the measurement equation gets amplified and introduces high frequency artifacts in to the obtained image.
In order to fills the gaps of invisible distributions in the (u,v) plane, where the synthesis array is insensitive, there are an infinite number of visibility distributions which can be added to the measured data. The nonlinear deconvolution make the best guess by using the 'priori' knowledge or constraints, and generates new spatial frequencies information at the unmeasured spatial frequencies in the aperture (u,v) plane.
Mainly, in radio astronomy imaging there are two nonlinear deconvolution schemes, CLEAN and MEM, which recovers the true image from the blurred dirty image due to the PSF response. These algorithms with its merits & demerits are discussed below. This section also discusses the experience and understanding of the practical usage of CLEAN algorithm & its various types implemented in IMAGR task, and of MEM algorithm implemented in VTESS task.

3.2.1 The CLEAN algorithm

The IMAGR task in AIPS implements B.G. Clark's (1980) CLEAN algorithm with the enhanced version made by Cotton & Schwab (1984).

The original CLEAN algorithm devised by Högbom (1974) assumes that the sky is a collection of point sources. As per this algorithm, the dirty map can be considered as the superposition of point sources, where each point source is multiplied by the instrumental function i.e. the dirty beam. Then, this algorithm finds the positions and strengths of these point sources and divide the dirty beam in non-linear fashion i.e. repeated subtraction of the dirty beam.
In practice Högbom algorithm proceeds as follows : (i) From the given dirty map, find the brightest peak and store its flux value and position. (ii) Multiply it with the dirty beam and loop gain factor ($\gamma < 1$). Shift this weighted dirty beam at the location of brightest peak and subtract it from the dirty map. (iii) Take the new residual map as a dirty map and repeat the algorithm until the residual map reaches to the noise level. (iv) Finally, convolve all the ensemble of accumulated points known as 'clean' components with a clean beam which is generally a elliptical Gaussian fitted to the FWHM of synthesized dirty beam. (v) These convolved clean components are added back to the last residual map in order to get the 'clean map'. This kind of addition of convolved clean component to the residual map is equivalent to adding a sine wave of some amplitude and phase to the visibility function in (u, v) domain. In this way the visibility measurement at spatial frequency of unsampled part i.e. holes in the aperture plane are filled.
A variation of Högbom CLEAN by Clark and revised by Cotton-Schwab work sequentially in two loops, one is a minor loop in which patches are defined surrounding the brightest peaks in the dirty map and uses a patch of dirty beam to clean each patch using Hoğbom clean. The next loop is the major loop surrounding the minor loop, Fourier transform the clean components using either DFT or FFT to UV plane and remove from the ungridded uv-data. Then, make a new residual map by gridding the data and fourier transform it to the image plane. Algorithm repeats the minor and major loop till the residual map reaches to noise level.
Fig. 3.1-a shows the map of NGC 4565 at 617 MHz using the Cotton-Schwab algorithm. The practical use of the 'CLEAN' algorithm depends upon the number of control parameters which are discussed bellow :
1. Loop gain and number of iterations : The number of iterations decides the maximum number of clean components, and the value of loop gain ($\gamma \leq 1$) is the fraction by which the peak is subtracted. So to reduce the number of iterations in the CLEAN procedure, value of loop gain can be increased up to one. The subtraction of weighted dirty beam with the loop gain value equal to one has no problem for the isolated point sources, but when the dirty beam with its negative sidelobes & high loop gain gets subtracted from the smooth brightness area, it creates opposite sidelobes on the residual map, and hence these dummy signature are considered as the brightest peak in the next clean iteration. Therefore, CLEANing on the smooth brightness region should always be done with a low value of the loop gain. As the strong source sidelobes affects the weak source, the dirty beam is subtracted with some attenuation by the loop gain value which is by default 0.1 .
We used a loop gain equal to 0.5 for cleaning confusing bright sources away from the region of interest, and as the source structure started appearing after a few iterations, the loop gain has lowered to the value equal to 0.02 or 0.03 to clean on the object.

The deep cleaning with the lower loop gain was necessary to get the maximum clean components of low surface brightness emission of NGC 4565 and NGC 2997, the number of iteration used for this purpose was typically around 40000 to 50000.

2. Flux : Clean will stop its iteration either when the maximum number of clean components exceed the 'niter' value or the absolute value of highest peak is less than the given value for the FLUX. It is an optional adverb and normally it's value should be around the expected RMS noise level of the map times the dynamic range of the dirty beam.

3.Windows and degree of freedom : As per Schwarz analysis of the CLEAN, clean can not converge on unique solution if the number of clean components exceeds the number of independent visibility data points. The "Clean window" is the way to provide aprior knowledge about the source to the CLEAN algorithm, where the the CLEAN can optimize the number of clean components as a representation of the sky by searching the clean components over the restricted area only. To locate these areas, we first made a low resolution and large size map so that boxes or clean windows can be put around the strong confusing sources and the target field.

4. Restoring beam : The pixel to pixel correlation across the main central lobe is not enforced in CLEAN, which can result into the spurious structure on scales smaller than the resolution allowed by maximum baseline. Such implicit extrapolation by CLEAN beyond the maximum baseline can be weighted down by convolving the clean components with the restoring beam, which is generally an elliptical Gaussian. The size of restoring beam can be specified by the BMAJ,BMIN and BPA. If the values of BMAJ and BMIN are zero, then by default, elliptical Gaussian is fitted to the central portion of the dirty beam.

5. Zero spacing flux : Any extended structure with a low brightness emission has much power at the short-spacings. The lack of short spacing can cause poor interpolation for the unsampled region of short uv-spacing, which can result unphysical negative brightness region around the source and incomplete structure of the extended source. So it is some times necessary to cope with the short spacing problem by providing zero spacing flux, which should ideally measured by the single dish. For the map presented in this section, there was no indication of negative brightness region around the object, hence the zero-spacing flux is not applied.

Instabilities of CLEAN algorithm is well described in course notes from NRAO on synthesis imaging and *VLBI techniques and application* by Felli & Spencer. The map of extended and smooth brightness distribution structure produced by CLEAN has spotty or blotchy appearance due to the dirty beam subtraction from the smooth brightness area which is explained above. Also, clean is known to produce "strips" in the maps, which appeared in our case for one of the NGC 2997 maps at 610 MHz. Also as mentioned above, in the case of poor sampling CLEAN does incorrect interpolation or extrapolation in the unsampled part of UV-plane. The priori information can be introduced in a CLEAN algorithm by only the "Clean Window", and there is no other constraint which can be put in this algorithm in contrast to the Maximum Entropy Method algorithm, which we will discuss in the next section.

The CLEAN is easy to visualize and use, and can produce the reasonably good maps, so we used the CLEAN algorithm throughout for the mapping in this report.

3.2.2 The Maximum Entropy Method

In MEM the sky is assumed to be positive and smooth. To generate new spatial frequencies information at the unmeasured spatial frequencies in (u, v) plane, MEM uses the non-linear transfer function in the 'entropy' form which maximizes or minimizes the pixel brightness, and ensures that the image is positive. Among the many solutions to the non-linear deconvolution, MEM selects the solution havin the greatest entropy and the solution is also subject to the constraint that the Fourier transform of model or true image multiplied by the sampling function should yield the true visibility data within some noise limits. The priori information can be introduce in the MEM via a total intensity normalization constraint.
The general purpose form of normalized entropy used in the MEM is

$$H = \sum_i -b_i \ log(\frac{b_i}{m_i})$$

In this equation, b_i is the brightness at the i'th pixel and m_i is the default brightness or the default image which allows the *priori* information incorporated into the problem. The default image can be a low resolution image of the object. The maximization of the entropy function enforces the smoothest positive image in which details does not appear unless it is found in the data.
In a practical implementation of MEM, the requirement that each visibility is fitted exactly by the model usually invalidates the positivity constraint. Therefore, data are incorporated with the constraint that the fit, χ^2 , of the predicted visibility to that observed, be close to the expected value. A requirement of the total flux F in the model (normalization) being correct as specified by the zero spacing flux is also usually enforced. Hence the function to be maximized, Q, thus contains two or three terms.

$$Q = H - \lambda\chi^2 - \alpha F$$

A Lagrange multiplier is introduced for each constraint : λ for the χ^2 constraint which governs the weighting given to entropy & the χ^2 term, and α for the normalization constraint.
Fig. 3.1-b shows the restored image of NGC 4565 at 617 MHz using the AIPS's task VTESS, which performs a non-linear deconvolution of dirty beam from the dirty image by the Maximum Entropy Method. VTESS maximizes the entropy subject to the constraint that the r.m.s residual noise be ≤ 1, and the total flux is equal to the zero spacing flux provided by the input parameter FLUX. Thus, there are various vital control parameters which are required to get the VTESS image.
As the MEM algorithm spends much of its time to adjust the brightness of strong point sources which represent only the few dominant pixels, the strong confusing sources in the primary field are removed by cleaning only these point sources and then subtracting it from the visibility data by the UVSUB task. Then the image size was restricted only to 1024×1024 pixels for the further processing.
1. Convergence : The convergence depends on the combination of input parameters like NITER, FLUX and rms residual or NOISE. If the given number of iteration is less than zero, then VTESS stops its iterations when either the number of iteration has reached the value of ABS(NITER), or the solution is achieved, i.e. rms residual $< 1\sigma$, and the total flux density value of the VTESS map is achieved within the

5% of FLUX. To converge faster and to alleviate the effect of sidelobes due to the bright point source embedded in extended emission, the dirty map is convolved with an elliptical Gaussian beam.

2. Default image : As the entropy function reveals that the MEM image is biased towards the default image, a priori information can be provided to the algorithm via the default image. A low resolution CLEAN map is provided as the default image, which MEM algorithm uses as the initial model of the object to begin with. After a few iterations, the VTESS task is stopped manually, and the VTESS image provided as a default image for the next two loops.

3. Noise : The r.m.s noise level is a crucial control parameter. It should be comparable to the r.m.s. noise level in blank region of a CLEAN map. If it is too high, then VTESS will not do much deconvolution and if it is too low number then convergence will not achieved, since there will be no positive map which fits the data to that level. The value of NOISE parameter was given around 0.3 to 0.5 mJy/Beam, this value is estimated from the blank regions in the clean image shown in fig 3.1-a.

4. Total flux density : The total flux contained in the image is a important parameter; if it is not specified then the value obtained may be biased towards a low signal to noise ratio. The high value of total flux density allow the algorithm to build up brightness in the largest sidelobes of the dirty map. The positive value of the FLUX needs correct estimates so that it must fit to within 5%. A rough idea of total flux density within a factor of 2 can be provided with the negative sign so that it will help the VTESS to estimate the true value. The flux value of 400 mJy with the negative sign was provided to estimate the zero spacing flux for VTESS image, the estimated value was given from a low resolution image, and from the Westerbork observation at 610 MHz by E Hummel et al (1984).

5. Resolution : VTESS gives the output image which has units of Jy/pixels, and the resolution of this image is dependent upon the signal to noise ratio. To compare the MEM image with the equivalent clean image where map units are in Jy/beam, the MEM output image is convolved with the circular Gaussian beam of 12 arcsec resolution.

After 46 iterations with the default VTESS image of previous run, we got the MEM image with the total flux around 419 mJy, and the rms residual $\sim$1.5E-4 Jy/beam.

Fig. 3.1-a and Fig. 3.1-b are both restored using the circular gaussian beamsize of 12 arcsec, rms noise level σ in both the maps is 0.3 mJy/beam area. Contour levels plotted are at $3\sigma\times$ (-3, 1, 1.5, 2, 2.5, 3, 3.5, 4, 4.5, 5, 5.5, 6). From the CLEAN and MEM map, it is clear that the MEM image is more smooth and flattened than the CLEAN image and also most of the features in the CLEAN map is matching with the MEM image.

Figure 3.1: NGC 4565 at 617 MHz

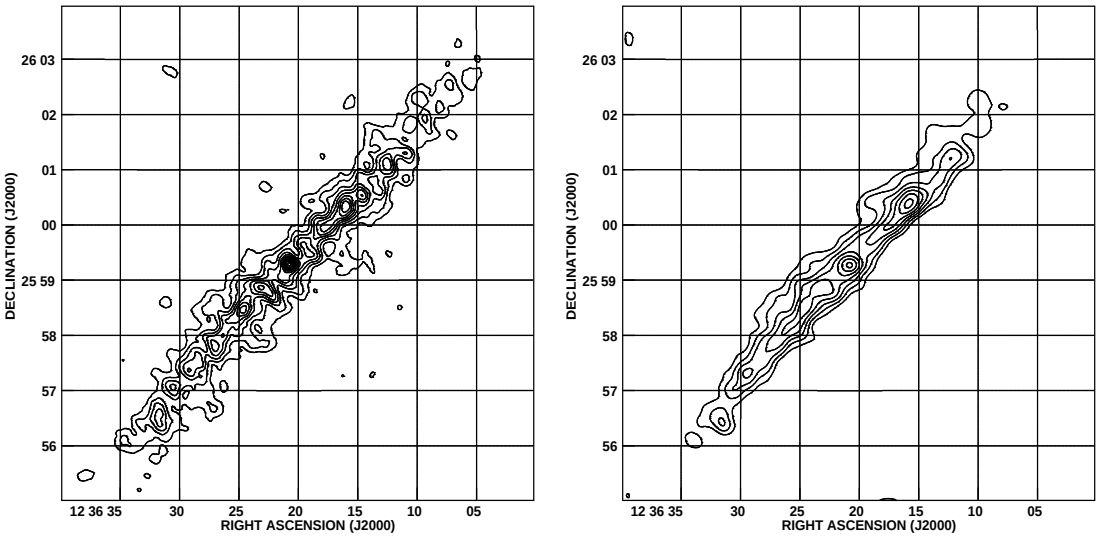

fig a. CLEAN image

fig b. MEM image

3.3 Sensitivity of an Image

The RMS noise in stoke I image formed from dual polarization data given by the homogeneous array of N identical antennas is given by

$$\Delta I_m = \frac{\sqrt{2}\, k_B T_{sys}}{\eta_c\, \eta_a A \sqrt{N(N-1)\, N_{IF}\, \Delta\nu\, T}}$$

Where, k_B is a Boltzmann constant, η_c is the correlator efficiency, A is the antenna area, N is the total number of antenna, N_{IF} is the number of independent IF channels, T is the total observing time, and $\Delta\nu$ is the observing bandwidth. The T_{sys} is the system temperature defined to include many sources of additive noise from the receivers, ground spill over, atmospheric emission, the galactic background emission at low frequency, and microwave background emission. The RMS variation of brightness I limits the weakest feature that can be detected in absence of other imaging limitations like confusion , dynamic range etc.
The brightness of a source is given by Jy per synthesized beam and RMS noise in the image is ΔI_m Jy per synthesized beam. A point source has constant apparent flux per synthesized beam regardless of the beam size. For an extended source which is resolved, having constant flux I per steradian, the flux density is $I\Omega_s$, where Ω_s is the synthesized beam area in steradians. Hence, the signal to noise ratio of the extended source is $I\Omega_s/\Delta I_m$. In this case, the signal to noise ratio increases with size of synthesized beam till the beam size is smaller than the extended structure of interest.

As discussed in the imaging section, the natural weighting enhances the sensitivity for the detection of the source at the expense of low resolution, since every measured visibility is given same weight and density of uv-points is high near the

center of (u, v) plane. Whereas uniform weighting yields a high resolution beam but degrades the sensitivity by down-weighting the densely sampled short spacings. For an extended structure, the longest baselines generally will have less correlated flux density, and hence using them in image processing can contributes to the noise. By tapering, we can reduce the noise and improve the detectability of the source using only those baselines which contributes to the signal. Effectively, the result of weighting is also depend on the uv-coverage, and sensitivities of antennas in the array.
As per values of observing parameters given in table 2.2 for NGC 2997 and NGC 4565 and the GMRT specifications of the T_{sys} & the Gain (K/Jy) of the array element, the theoretical estimate of RMS noise ΔI in the total intensity image at 325 MHz is $\sim 17\mu$Jy , at 610 MHz it is around $\sim$ 16 to 20μJy, and at 1280 MHz 0.2 to 0.22μJy. These values are calculated assuming a natural weighting.
Image obtained by Fourier inversion of the visibilities generally gets corrupted with the noise level many times higher than the theoretical value of ΔI_m due to various reasons, like incompletely sampled uv-plane, phases are affected by atmospheric or instrumental effects, and radio interference etc. So the RMS noise in the total intensity map achieved using the tapered and weighted visibility data is much higher than the theoretical value. The values of RMS noise level are given in the map parameter table 4.1 for NGC 2997 and table 4.3 for NGC 4565. The RMS noise in the total intensity map of NGC 2997 using uniform weighting & without uv-taper is 1 mJy/beam at 325 MHz, 200 μJy/beam at 610 MHz and 100 μJy/beam at 1280 MHz. The total intensity map of NGC 4565 at 20 arcsec resolution with the natural weighting and tapering the longer baselines, the RMS noise is 1 mJy/beam at 325 MHz, 400 μJy/beam at 610 MHz and 300 μJy/beam at 1280 MHz.
In practice, the griding process in imaging degrades the sensitivity at the edge of image due to the noise aliased back in the image by the re-sampling of convolved visibilities, and due to the division of the image by Fourier transform of convolution function of visibility to remove the effect of convolution done in the visibility domain. Also, the sensitivity is reduced at the off-center image locations due to the primary beam gain attenuation by the array element. These limiting factors in the image synthesis are discussed in the next few sections of this chapter.

3.4 Radial and azimuthal smearing

For continuum observation, spectral components over the observing band are averaged together, and the spatial frequency coordinates (u_0, v_0) are computed with respect to the band center ν_0. Since (u, v) are the baseline components measured in wavelengths, the spatial frequency coordinates for the measured visibility $v(u, v)$ at the other frequency ν within the band is scaled to the spatial frequency coordinates with respect to ν_0, such that, $(u, v) = (\frac{\nu}{\nu_0}u_0, \frac{\nu}{\nu_0}v_0)$.
While converting the scaled visibility at frequency ν into the brightness in image plane (l, m) , the effect on image can be shown by the application of similarity theorem of

Fourier transform,

$$V\left(\frac{\nu_0}{\nu}u, \frac{\nu_0}{\nu}v\right) \rightleftharpoons \left(\frac{\nu}{\nu_0}\right)^2 I\left(\frac{\nu}{\nu_0}l, \frac{\nu}{\nu_0}m\right) \tag{3.3}$$

where, (l, m) are the direction cosines with respect to (u, v).
Thus, the true brightness is scaled in (l, m) by ν/ν_0 and the amplitude is multiplied by $(\nu/\nu_0)^2$.
Since the correlation and Fourier transform are linear processes, the mean brightness distribution over the finite bandwidth can be obtained by summing the images made from all the frequencies within the band. The net effect of averaging the images aligned at the phase centre will produce radial smearing of the brightness before it is convolved with the dirty beam. A point source at an angular distance $\sqrt{l^2 + m^2}$ from the phase centre will have radial smearing by $\triangle\nu/\nu_0\sqrt{l^2 + m^2}$. The radial smearing comparable to the synthesized beam will suppress the sky features with reduction in surface brightness but without changing integrated flux density.
The radial smearing can be reduced by splitting the observing band into many narrow band channels. Since the FX correlator of GMRT gives 128 spectral channels across the observing band, to avoid the bandwidth smearing effect, the observing band of 16 MHz of USB or LSB is split in to four to five channles of 3-4 MHz for the L-band & 610 MHz and ten channles of ~ 1 MHz at P-band.

azimuthal or temporal smearing :

In the earth rotation aperture synthesis, the (u, v) components of baselines follows the elliptical path with the changing hour angle of the observing source in the sky. As the earth rotates with an angular velocity ω_e $(7.27 \times 10^{-5} rad\, s^{-1})$, longer baselines moves fast compared to shorter baselines. While averaging visibility data from the correlator for the finite time interval τ_a, the (u, v) coordinate is assigned with respect to averaged time centred at $\frac{\tau_a}{2}$, so the (u, v) coordinates for the sampled instantaneous visibility data points within the time interval τ_a in the (u, v) plane will have offsets up to $\pm\omega_e\frac{\tau_a}{2}$. The shift of the visibility data point along the uv tracks will produce the equal amount of shift in the image domain. In the final map, the result of averaging images made from each short snap will have the azimuthal distortion which manifests more with increasing distance from the phase centre. The azimuthal smearing is considered to be same as the bandwidth smearing but in the orthogonal direction.
The GMRT FX-correlator accumulates the visibility data with 128 ms rate, which can be averaged for long term acquisition. The default mode of averaging for the continuum observation is 16 sec.

3.5 Confusing sources in the primary beam

As number of strong background sources in the primary field is larger at the low frequency; it limits the dynamic range of map by adding noise due to its incoherent sum of the sidelobe response, called the confusion "noise". Sometimes rumbles are

appearing in mapping window due to strong point sources which are present just outside the mapping window, and also, unreasonably large size of map is required to clean the sidelobes of such sources.
The rms confusion expected from background sources in a primary beam with the source distribution function $n(S)$ is

$$\sigma_c = \rho\sqrt{\int P^2 d\Omega \int S^2 n(S)\, dS}$$

Where, P is the primary beam response, and ρ is the rms fluctuation of the synthesized beam.
While mapping the NGC 4565 and NGC 2997, the total brightness of fainter extended emission was not much larger than the rms noise fluctuation produced by the discrete background sources , so the 'confusion' was serious mapping problem. We first made low resolution map by giving UV-taper around 5 $k\lambda$ with larger image size than the size of the primary field to find the strong confusing sources which may be sitting outside or near the edge of the primary beam. The size of the primary field of view for the GMRT at 325 MHz, 610 MHz & 1280 MHz is 1.5 degree, 0.7 degree & 0.44 degree respectively.
There were two to three strong point sources near or outside the edge of the primary field at each frequency map of NGC 2997 with peak flux ten to twelve times stronger than the peak flux on the object. So the desired size of map to remove sidelobes responses from these sources was a bit larger than the default size of the primary field, we made maps of NGC 2997 at 325 MHz, 610 MHz & 1280 MHz with the size of primary field around 1.7 degree , 1.1 degree and 0.54 degree respectively
NGC 2997 image at 325 MHz was having three strong point sources near the edge of the primary field, lying more than $\sim 0.50^\circ$ distance from the phase centre and having ten to twelve times stronger peak flux than the peak flux on the object. Similarly map of NGC 2997 at 610 MHz was having two strong point sources outside the primary beam area at a distances of $\sim 0.46^\circ$ & $\sim 0.51^\circ$ from the field center. At 1280 MHz map of NGC 2997, there was one strong point source at the edge of the primary beam. There were five strong point sources in the primary field of NGC 4565 at 325 MHz having peak flux around twenty to hundred times greater than the peak flux of NGC 2997 . Four of them was outside the primary beam area having distances around $\sim 0.85^\circ$ to $\sim 1.0^\circ$ from the field center and one was near the edge of the primary field. Therefore, desired size of the primary field for the mapping of NGC 4565 became around 2.2d. Positions of these sources and the detail of flux measurement are given in section 4.3.
Since the sidelobes of the brightest sources affects the field of weak sources, sidelobes response in the field of interest must be removed to reduce the level of confusion noise. In the CLEAN deconvolution algorithm this is exactly achieved via storing the deconvolved image by finding and removing the series of delta functions from the image. To achieve the parallel deconvolution for all the field, the clean component found in any one subregion is fourier transformed to the u-v plane and removed from the ungridded visibility data.
The strong isolated point source situated outside the primary field of view or at much farther distance from the region of interest contributes noise due to its sidelobes. To

remove such kind of effects by deconvolution using the clean algorithm, it requires a larger map size than the size of interest, which becomes an overhead each time while cleaning iteratively in the self calibration procedure. At 610 MHz map of NGC 4565, there was an isolated point source at a distance of 0.60 degree from the phase center, with peak flux around $\sim$ 46 times greater than the peak flux on the object. The response of this source was removed using the UVSUB task. After cleaning the field around this point source with the 3D-image option (which reduces the non-coplanar distortions), the clean component file was provided to the UVSUB task, which subtracts the Fourier transform of clean components from the visibility data by the DFT (Direct Fourier Transform) method.
The rms confusion uncertainty σ_c due to the confusing sources which are lying behind the galaxy disk or close to it, can contribute to the errors in the measurement of integrated flux density over the disk region. In the case of NGC 2997 and NGC 4565, since the radio emission generally exhibits well centred and symmetrically extended, we tried to look at the confusing point sources which are brighter and not coinciding with the optical positions in the optical map of the galaxy. The extra nuclear components was along the spiral arm in the case of face-on, or along the equatorial plane in case of edge-on, so we did not find any such confusing source which could affect the measurement of total flux density.

3.6 W-term correction

W-term is a baseline vector component pointing towards the direction of phase tracking centre where fringe rotation effectively phases the array. A wavefront away from the phase tracking centre but on the celestial sphere ($\mathrm{l}^2 + \mathrm{m}^2 + \mathrm{n}^2 = 1$), will introduce an "extra" phase equal to $2\pi w\sqrt{1 - l^2 - m^2} = \pi w\theta^2$ or phase error $\phi\,\alpha\,B_{max}\lambda/D^2$, where B_{max} is the length of the maximum baseline in meter and D is the antenna diameter in meter.
For mapping the region of a small angular extent, sky can be approximated to 2-D plane close to the phase tracking centre. Therefore, dependence of the visibility on the *w-term* is very small. Assuming $|\pi(\mathrm{l}^2 + \mathrm{m}^2)\mathrm{w}| \ll 1$, we can get the source brightness distribution $\mathrm{I(l, m)}$ by two dimensional Fourier inversion.
In the case of the planar arrays, where baselines are in east-west directions and the component of baseline vector parallel to the earth axis is zero, *w-term* is a linear function of u & v and gives linearly increasing phase error across the u-v plane, which can be corrected geometrically by redefining the direction cosine (l, m).
Need for w-term correction: The array configuration at GMRT is made in a 'Y' shape to maximize u-v coverage by keeping the baselines with a significant component parallel to the earth's axis. Also, when the earth-rotation aperture synthesis performed, the baselines are no longer coplanar, since the array geometry as viewed from the source changes with time.
Primary field of view at low frequency like 610 MHz and 325 MHz is large and generally contains around 20 to 40 confusing sources or more, the sidelobes from these sources can contribute to image noise. If such sources are away from the phase centre,

they produce phase errors which increase with the square of distance from the phase centre. Such phase errors severely distort the image.
Thus, non-coplanar baselines and spherical curvature of nature causes the apparent shift in source position, rms noise fluctuation in the map, which results in limiting the dynamic range of map and distortion across field of view.
There are several techniques for reducing non-coplanarity problem; an overview of possible solutions and the implemented method to reduce the *w-term* effect at the 325 MHz & 610 MHz are discussed briefly as below:

1. 3-D Fourier Transform : A three dimensional Fourier transform of visibility $v(u, v, w)$ can be taken by considering the 3-D celestial sphere (l, m, n),where (u, v, w) & (l, m, n) are conjugate variables.

$$F(l, m, n) = \iiint V(u, v, w) e^{2\pi i(ul+vm+wn)} du\, dv\, dw \tag{3.4}$$

   where, $n = \sqrt{1 - l^2 - m^2}$ is treated as an independent variable, and F(l,m,n) referred as image volume.
   Sampling the visibility along w-axis at Nyquist rate will give the telescope transfer function,i.e. dirty beam $B(l, m, n)$

$$B(l, m, n) = FT[s(u, v, w)]$$

   Dirty beam gives dirty 'image volume' by convolving with the true image volume.

$$I^D(l, m, n) = \left[\frac{I(l, m)\, \delta(\sqrt{1 - l^2 - m^2} - n)}{\sqrt{1 - l^2 - m^2}} \right] * B(l, m, n) \tag{3.5}$$

   Where, $I(l, m, n)$ will be finite away from the celestial sphere which would correspond to non-physical emission in the image volume due to sidelobes of the dirty beam.
   A 3-D deconvolution using the dirty image and the dirty beam will produce a clean image volume. After 3-D deconvlution an interpolation is required to put all the points of a clean image volume along the celestial sphere on a common 2-D tangent plane.

2. Sum of snapshots : For a snapshot over suitably chosen intervals, w is a linear function of u & v, as in the case of the coplanar array. Then the field can be imaged in each interval with different effective co-ordinate systems, and deconvolved separately. Thus, the correction can be made for the distortion introduced by neglecting the *w-term*.
   Finally, all the images are averaged.

3. Faceted Transform : To reduce the *w-term* effect, a 2-D approximation can be done by shifting the phase centre to different parts of the image and a small field around the shifted phase centre can be used for mapping, which is nearly a tangent plane, called 'facets'. To reconcile multiple fields made from the single image, an interpolation is done on a common tangent plane with respect to the

pointing position of observation.
Visibility data is phase rotated to shift the phase center at each facet. In this case, the visibility data is decomposed into summation of k visibilities predicted from a number of 'facets'.

$$v(u,v,w) = \sum_k \left[V_k(u,v) \frac{e^{j.2\pi\,(ul_k + vm_k + w\sqrt{1-l_k^2-m_k^2})}}{\sqrt{1-l_k^2-m_k^2}} \right] \tag{3.6}$$

Where, the visibility of the k^{th} facet in 2-D transform is given by

$$V_k(u,v) = \int I(l-l_k, m-m_k) e^{-j2\pi[u(l-l_k)+v(m-m_k)]} dl\, dm \tag{3.7}$$

To cover all the sources in the primary field and strong confusing sources near the primary beam, the required number of fields or facets is $2B_{max}\lambda/D^2$, where B_{max} is the length of maximum baseline and D is the diameter of the antenna in meter.
The number of facets used for the mapping of NGC 2997 at 325 MHz and at 610 MHz were around 22 and 13 respectively, whereas for the mapping of NGC 4565 at 325 MHz and 610 MHz the number of facets for each map was 7 and 13. We used the 'IMAGR' and 'FLATN' tasks of the AIPS to implement the faceted transform algorithm while mapping the NGC 2997 & NGC 4565 data at 610 MHz and 325 MHz , in the following sequence :

a. As the primary field at 325 MHz and 610 MHz contains many bright sources and complex structure, number of fields were created by the 'SETFC' task. It searches the NVSS source catalogs for sources above the given flux limit in Jy and given search radius in degree around the pointing used for target source. The SETFC task writes determined multiple fields in a text file specified by the adverb BOXFILE which contents the field number, field size in pixels, and RA & DEC for each field center. Also, we put boxes manually around the obvious bright sources which could degrade the rms noise level and the quality of the map.
   As the number of field was around ten to twenty, a text file created,in which the field number, size of the field in pixel and the centre RA & DEC for that field specified in the co-ordinate card format. This text file was provided as a input to the IMAGR task using the BOXFILE & NFIELD options.

b. After residual images formed for all the facets, partially deconvolution was done for individual facets to update the model (clean compontnes) of each facets.

c. By giving the OVERLAP ≥ 2 option in the IMAGR task, components found in one field is restored in all the overlapping fields. Also, the clean component found in one field is subtracted from the ungridded UV data to avoid the affects of sidelobes of strong sources appearing in other fields.

To improve the dynamic range of map, the DO3DIMAGE TRUE option is used for 3-D imaging which shifts the tangent point to the field's centre. Residual image is recalculated and algorithm repeated till the residual image is reaches to noise level.

d. After deconvolution of each field, finally all the cleaned facets are projected on to a common tangent plane with the phase centre at the pointing of observation. The FLATN task is available in AIPS for this purpose, which also does the primary beam correction.

3.7 Primary Beam Correction

The field of view for the aperture synthesis array is limited by the normalized reception pattern or primary beam response of the array element, which is given by $A(\theta, \phi) = A_e(\theta, \phi)/A_e^{max}$, where, the A_e^{max} is the primary beam response at the beam center, and $A_e(\theta, \phi)$ is the effective collecting area of the antenna.
The primary beam response or the power pattern is a square of the complex far field voltage pattern of the antenna. For 1-D case of circular aperture, electric field across the aperture is a rectangular function and Fourier transform gives the far field voltage pattern of antenna which is a *sync function*. The main lobe of far field pattern is known as the primary beam of antenna; the primary beam gain falls at the edge of beam.
The sky brightness distribution $I(l, m)$ across the field view is multiplied by the primary beam response of array element, which result in reduction of the apparent brightness of sources depending on their positions in the primary field of view. The primary beam response is a frequency dependent instrumental function. Hence, to recover the actual brightness of the sources within a field of view, image is divided by the primary beam gain factor. In the case of a GMRT antenna, the model for primary beam response at different frequencies can be obtained by fitting a Gaussian or polynomial fit of 8^{th} order to the primary beam data measured along the 1-D grid in the azimuth or elevation direction on the strong point source at the beam center. The details of the experiment and the result obtained can be referred in the tech. report *GMRT antenna power pattern in L-band by N.G. Kantharia & A.P.Rao* (July, 2001).
The primary beam corrections are applied after deconvolution of image or at the final stage of image using the PBCOR task in AIPS. The PBCOR requires the model of primary beam of the functional form

$$F(X) = 1.0 + (a * X)/10^3 + (b * X^2)/10^7 + (c * X^6)/10^{10} + (d * x^8)/10^{13}$$

Where, a,b,c and d are the coefficients of polynomial fit, and X is (Distance from the beam center(arcmin) $\times$ Frequency(GHz))^2. The primary beam correction is applied to all the maps of NGC 2997 and NGC 4565 using the FLATN task, which interpolates all the set of cleaned facets to a single image having a common phase center. The FLATN applies the primary beam correction similar to PBCOR. The coefficient value of the polynomial fit for 325 MHz, 610 MHz & 1280 MHz maps were provided from the report mentioned above. The correction to scale the coefficients in

above the equation at the observing frequency is done by the FLATN or PBCOR task.

Chapter 4

Observational Results

The results deduced from the multi-frequency radio continuum observations of NGC 2997 and NGC 4565 using the GMRT at 325, 610, and 1280 MHz are presented in this chapter via the total intensity maps made over a variety of spatial resolutions at each frequency. The features of the radio continuum structure emerging from the low-resolution as well as the high resolution maps and their properties are summarized in the first section of this chapter.
We have studied the radio continuum emission spectra for both the galaxies in the range of 325 MHz to 10.5 GHz,including the total flux densities obtained from the GMRT observations. In order to derive the relative contribution of the thermal free-free emission and the synchrotron emission to the total flux densitiy at a certain frequency, a two-component (bremsstrahlung and synchrotron) spectra were fitted to the integrated spectrum of each galaxy. For the spectral index distribution study, we made the maps for each object at λ92 m, λ42 cm, and λ23 cm with a similar spatial scale and smoothed them to a common resolution. The total emission curve and spectral index distribution study of NGC 2997 and NGC 4565 are discussed in the section 4.2.
A list of the flux densities and the positions for background sources in the primary beam of each observing frequency is given in the last section.

4.1 Total intensity maps

The total intensity maps of NGC 2997 and NGC 4565 are shown in figures 4.1, 4.2, 4.3, 4.5 and 4.6. The tables 4.1 and 4.3 give map parameters of NGC 2997 and NGC 4565 respectively, for the above mentioned figures.
To detect the low surface brightness distribution from the disk or from the halo of the galaxy, one needs the shorter baselines of the central-square antennas of GMRT. The enhanced high angular resolution given by the longer baselines from the arm antennas is useful to reveal the strong spiral ridges, morphological details of the nucleus in the case of the face-on galaxy and the emission features from the thin disk in the case of the edge-on. Also, good sensitivity at high resolution is useful to detect the compact sources embeded in the diffuse emission like bright Giant HII regions ionized by hot stars and nonthermal compact sources. However, the same set of baselines at two

frequencies may see completely different structures of the source, since the visibility measured by a baseline is a function of the observing frequency. To make maps of the object at different frequencies to a similar spatial resolution so that consistency of the radio features can be checked, we used the uv-tapering function which suppresses the visibilitiy samples from longer baselines. The uv-tapering and weighting functions used while mapping the object at various resolutions is given in the table for the map parameters for each object.
To make it easier to interpret the clean map, maps presented here were restored with the circular clean beam equivalent to that of the elliptical gaussian beam obtained by default fitting to the central portion of the dirty beam. Also, the area of the circular beam was kept close to the default clean beam area, so that residuals convolved with the dirty beam and clean components convolved with the circular beam do not differ greatly. Also, it is important to note that our maps restrored with the circular clean beam did not super-resolved the obtained synthesized clean beam; the resotred circular beam size is $\gtrsim 0.8$ than that of the synthesized beam, and hence, does not crosses the limits of super-resolution criteria set by Felli & Spencer (*VLBI techniques and application*). The map restoration with the circular clean beam has the advantage that any elongated structure in the continuum map will appear in their correct orientation. The synthesized clean beam and the restoring beam of the individual map are mentioned in tables 4.1 and 4.3.
All the total intensity maps were corrected for the primary beam attenuation using a polynomial approximation of the GMRT primary beam which is discussed in section 3.7. The depicted radio continuum maps have the first positive radio contour at 3σ level. The maps are superimposed on the optical images taken from the Digitized Sky Survey (Royal Observatory Edinburgh, *the Southen Sky* or the Oschin Schimidt Telescope on Palmor Mountain, *the Northern Sky*). The overlaying of the radio map on the optical image makes the interpretation of the radio features easier and helps in the study of the radio-optical correlation.

4.1.1 NGC 2997

NGC 2997 is a bright late-type spiral (SAc) galaxy, centered at α_{2000}=$09^h45^m38.8^s$; $\delta_{2000} = -31°11'28''$ (de Vaucouleurs et al., 1991). This galaxy possesses a small bright yellow nucleus and two prominent spiral arms begin at the center along with the opaque dust lanes which are clearly seen against the high-surface-brightness of the inner disk. Its southern arm shows bifurcation into a third arm towards the west. Spiral arms show many red lumps of ionized hydrogen regions which are likely to be star-forming regions. The disk of NGC 2997 is inclined at about 40° (Milliard & Marcelin 1981) to our line of sight, where the southern edge is nearest to the observer (Peterson 1978). NGC 2997 is at a distance of $\sim$ 12 Mpc ($H_0 = 75 km\, s^{-1} Mpc^{-1}$), hence, along the major axis, 1 arcmin corresponds to a linear scale of about 3.5 Kpc. A description of the total-intensity GMRT images of NGC 2997 at 325, 610 and 1280 MHz is given below with respect to low, medium, and high resolution maps at each observing frequency, the map parameters are given in Table 4.1.
1. 325 MHz : The total intensity maps at 325 MHz with a spatial resolution of 48,

Table 4.1: Map parameters of NGC 2997

Band Center (MHz)†	332	616	1272
Final Bandwidth $(MHz)^a$	12.5	12.5	12.5
Low Resolution Map	Fig 4.1a	Fig 4.2a	Fig 4.3a
Synthesized beam^b	$49.5'' \times 41.2''$@45°	$32.0'' \times 21.7''$ @36°	$15.8'' \times 12.4''$ @25°
Restoring beam^c	48″	29″	15″
UV-taper/Weighting	$5k\lambda$/NA	$9k\lambda$/NA	$20k\lambda$/NA
RMS noise in the Map (mJy/beam)	2.0	0.8	0.3
Medium Resolution Map	Fig 4.1b	Fig 4.2b	Fig 4.3b
Synthesized beam^b	$29.9'' \times 25.0''$@41°	$17.9'' \times 11.7''$@41°	$9'' \times 5.8''$ @10°
Restoring beam^c	29″	15″	8″
UV-taper/Weighting	$8k\lambda$/NA	$20k\lambda$/NA	$28k\lambda$/UN
RMS noise in the Map (mJy/beam)	2.5	0.5	0.2
High Resolution Map	Fig 4.1c	Fig 4.2c	Fig 4.3c
Synthesized beam^b	$15.9'' \times 12.0''$@14°	$10.6'' \times 5.3''$ @44°	$5.3'' \times 2.6''$@4°
Restoring beam^c	15″	8″	4″
UV-taper/Weighting	$16k\lambda$/UN	None/UN	None/UN
RMS noise in the Map (mJy/beam)	1.0	0.2	0.1

†All maps are stoke I and corrected for the shape of the GMRT primary beam.
NA-Natural weighting, UN-Uniform weighting.
a. Final bandwidth for analysis after editing
b. Final synthesized clean beam, position angle with respect to the major axis is given in degree.
c. Restoring beam is a circular gaussian with PA=0 degree, and the area is approximated to the gaussian clean beam area in square arcsec $\Omega_s = 1.13 * \beta_{maj} \times \beta_{min}$.

29, and 15 arcsec are shown in figures 4.1a, 4.1b, and 4.1c respectively. The GMRT low resolution image at 325 MHz covers an emission area of $\sim 7' \times 8'$, being slightly less than the VLA 1.49 GHz radio contour map at a resolution of 0.9' ($\sim 7.3' \times 8.5'$) by Condon J.J. (1987). The spiral arms are barely resolved in the low resolution image, and shows a bright component in the northern arm at RA=$09^h45^m45.53^s$, DEC= $-31°10'29.79''$. Disk emission appears smooth, and more extended than the optical emission region of the galaxy.

The medium resolution map (Fig. 4.1b) shows a bright compact nucleus of $\sim$ 1.8 Kpc in size and a prominent northern spiral arm plus many discrete components which are clearer in the higher resolution image (Fig. 4.1c). There is an extended emission feature at the south-east side of the fig 4.1b near the region RA=$9^h45^m44^s$, DEC= $-31°13'50''$ (J2000), which has also been seen in the total intensity and the polarized intensity VLA maps at λ6 cm (Hans, 1999).

The position of the central source in the 325 MHz image (fig. 4.1.c) is at RA=$9^h45^m38.8^s$, DEC= $-31°11'24.23''$ (J2000), which is close to the values in H.Men & J.L.Han (2005) : RA=$9^h45^m38.6^s$, DEC= $-31°11'26.0''$ (J2000). The integrated flux density of the central nucleus at 325 MHz is 125.15 $\pm$5.19 mJy, and the peak intensity is 41.72 mJy/beam. A high resolution image of 15 arcsec at 325 MHz is shown in fig. 4.1c, overlaid on an optical DSS image. The distribution of radio emission from

the spiral arms are more extended than the optical spiral arms and follows roughly a similar spiral pattern as that of the NGC 2997 optical image. A high resolution radio image shows an interesting bright north source centered at RA=$9^h45^m39.9^s$, DEC= $-31°8'45.29''$ (J2000). An optical counterpart for this source does not appear in the DSS image. Another discrepancy between the optical and radio image is clear from the abscence of radio emisson from the region near RA=$9^h45^m32.8^s$, DEC= $-31°10'$ (J2000). This gap has also been seen in the VLA total intensity maps at λ20 cm, λ21 cm, and λ18 cm (J.L.Han, 1999; H.Men et.al, 2005). The prominent feature of radio emission distribution appearing in the fig. 4.1c is a bright compact component of the northern spiral arm, centered at RA=$09^h45^m45.53^s$, DEC= $-31°10'29.79''$. This component exactly overlies on the red-lump of HII region residing in the north-spiral arm shown by DSS image. A high resolution radio continuum map at 325 MHz does not show a bifurcation as seen in the DSS optical image.

2. 610 MHz : The low, medium and high resolution images of NGC 2997 at 610 MHz are given in figures 4.2a, 4.2b, and 4.2c respectively. All the total intensity maps at 610 MHz have the position of the central source at RA=$9^h45^m38.8^s$, DEC= $-31°11'26.0''$ (J2000). The uncertainty in RA and DEC is less than 0.16^s and $2''$ respectively. This position is close to the values given in de Vaucouleurs et al.(1991) : RA=$9^h45^m39.4^s$, DEC= $-31°11'28.0''$ and Han (1999) : RA=$9^h45^m39.4^s$, DEC= $-31°11'28.0''$. The measured integrated flux density of the central source (0.5') is about 75 mJy at 610 MHz.

All the maps at 610 MHz also show the north bright point source centered at RA=$9^h45^m40.0^s$, DEC= $-31°8'49.09''$ (J2000), and the obvious gap of radio emission in the north-west spiral arm; as seen in our 325 MHz maps and also in the total intensity VLA maps at λ20, λ18 cm and λ6cm (J.L. Han,1999). A low resolution image of 29 arcsec has broad emission from the north-spiral arm where the brightness peaks at the location of the red blob of HII region seen in the optical image. The correlation between the two (ie: the red blob and the radio component) is also clear from the high resolution image of 8 arcsec (fig. 4.2c). This northern spiral arm component is centered at RA=$9^h45^m45.0^s$, DEC= $-31°10'25.2''$ J2000.

Apart from these, the low resolution map (fig. 4.2a) shows a broad emission feature at the bifurcation of the southern spiral arm towards the west, being centered at RA=$9^h45^m31.8^s$, DEC= $-31°12'34.8''$ (J2000). In the total intensity maps of 29 arcsec and 15 arcsec resolution (fig 4.2-a and b), there is a compact emission source at RA=$9^h45^m48.8^s$, DEC= $-31°11'38.98''$ in the east direction $-$ at the end of the northern spiral arm. An extended faint emission in the south-east direction is also present in the medium resolution map of 15 arcsec which is similar to the medium resolution map at 325 MHz (fig. 4.1b). The 610 MHz high resolution radio image (fig. 4.1c) shows very clear spiral arm pattern which follows the optical arms, where the brightness peaks occur slightly on the inner side of the optical arms. Also, a radio emission feature of the bifurcation of southern arm towards the west into the third arm is seen clearly in this map.

3. 1280 MHz : The total intensity maps at 1280 MHz depicted in figures 4.3a, 4.3b, and 4.3c have spatial resolution of $15''$, $8''$ and $4''$ respectively. The radio emission

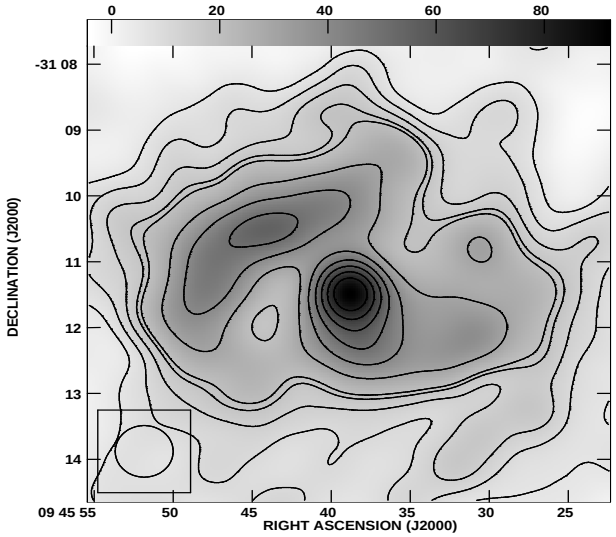

Fig. 4.1a : Low resolution map with the beamsize of 47", grey scale plus contours. The peak brightness is 89 mJy. The rms σ is 2 mJy per beam area, the beam size is shown in the bottom left corner. Contours levels are (-5, -3, 3, 5, 6, 7, 9, 10, 15, 20, 25, 30, 35, 40) $\times$ σ.

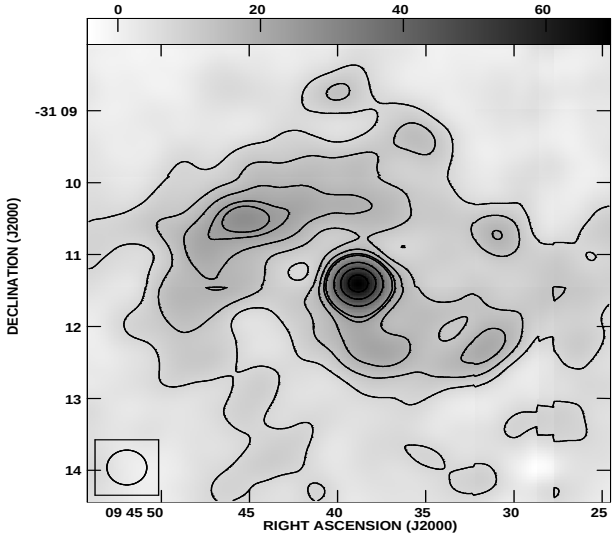

Fig. 4.1b : Medium resolution map at the beamsize of 29" with grey scale plus contours. The peak brightness is 68.8 mJy. The rms σ is 2.5 mJy per beam area, the beam size is indicated at the BLC. Contours levels are (-5, -3, 3, 5, 6, 7, 9, 10, 15, 20, 25) $\times$ σ.

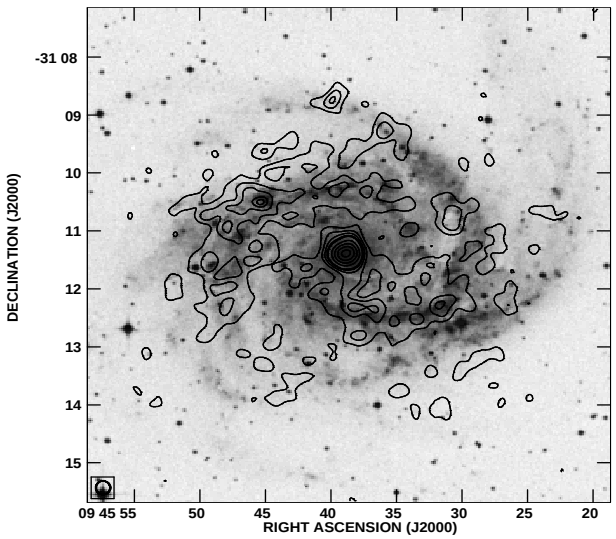

Fig. 4.1c : High resolution map with the beam size of 15", superimposed onto an optical Digitized Sky Survey image. The peak brightness is 36.3 mJy. The rms σ is 1 mJy per beam area, the beam size is shown at the BLC. Contours : (-5, -3, 3, 5, 6, 7, 9, 10, 15, 20, 25, 30, 35) $\times$ σ.

Figure 4.1: The total intensity map of NGC 2997 at 332 MHz

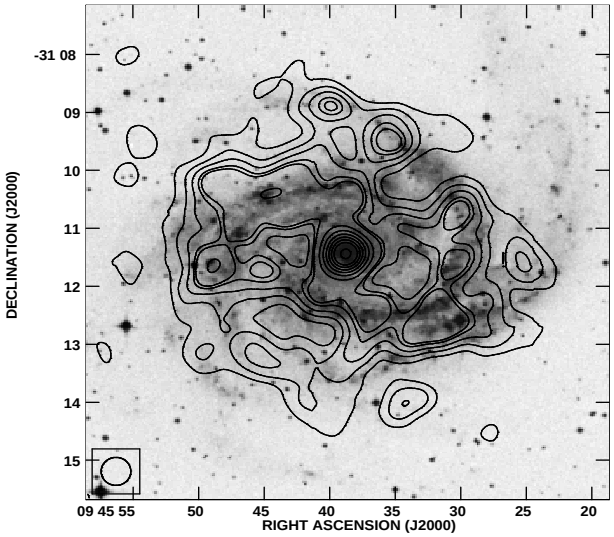

Fig. 4.2a : Low resolution map with the beam size of 29", showing the contours over a DSS optical image. The peak brightness is 47.4 mJy. The rms σ is 0.8 mJy per beam area, the beam size is indicated at the bottom left corner. The contours are at (-5, -3, 3, 5, 7, 9, 10, 15, 20, 25, 30, 35, 40, 50) $\times$ σ

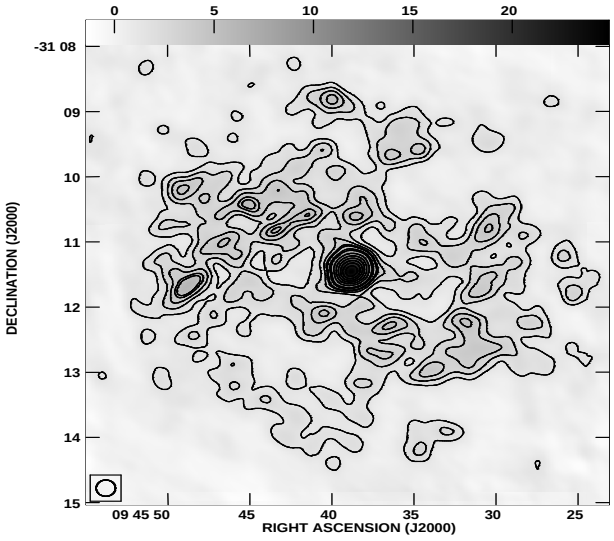

Fig. 4.2b : Medium resolution map with grey scale plus contours, the beam size is 15". The peak brightness is 25 mJy. The rms σ is 0.5 mJy per beam area, the beam size is depicted at the bottom left corner. Contours : (-5, -3, 3, 5, 7, 9, 10, 15, 20, 25, 30, 35, 40, 45) $\times$ σ

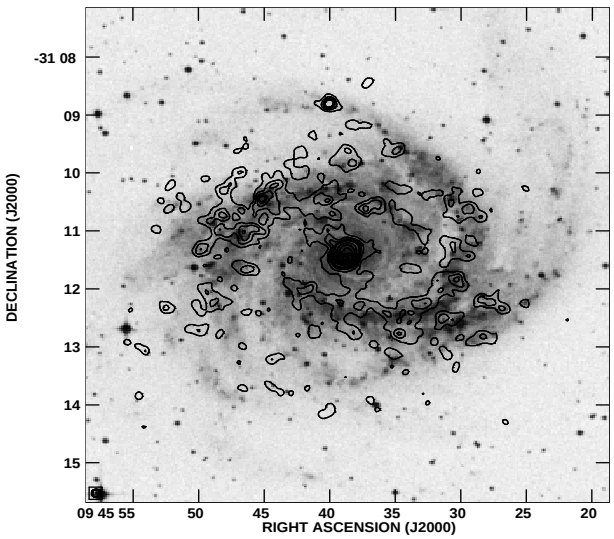

Fig. 4.2c : High resolution map overlaid on the DSS optical image, having beam size of 8". The peak brightness is 12.6 mJy. The rms σ is 0.3 mJy per beam area, contours are at (-5, -3, 3, 5, 7, 9, 10, 15, 20, 25, 30, 35, 40) $\times$ σ

Figure 4.2: The total intensity map of NGC 2997 at 616 MHz

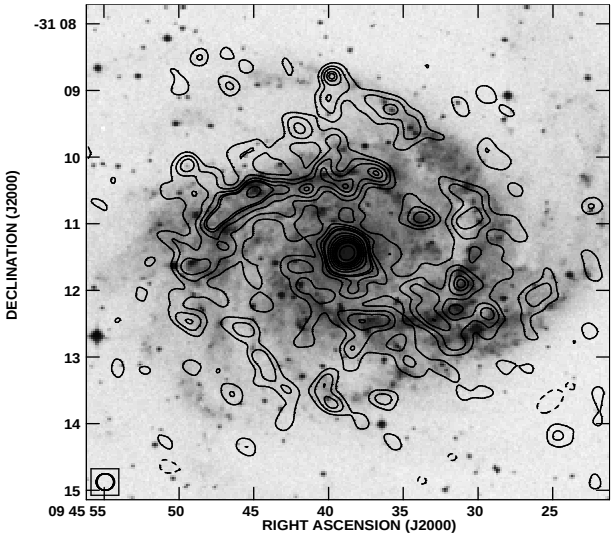

Fig. 4.3a : Low resolution map with a resolution of 15", the contours are shown overlaid on the DSS optical image. The peak brightness is 18.9 mJy. The rms σ is 0.3 mJy per beam area, the beam is depicted at the bottom left corner. The contours are at (-5, -3, 3, 5, 7, 9, 10, 15, 20, 25, 30, 35, 40, 50) $\times$ σ

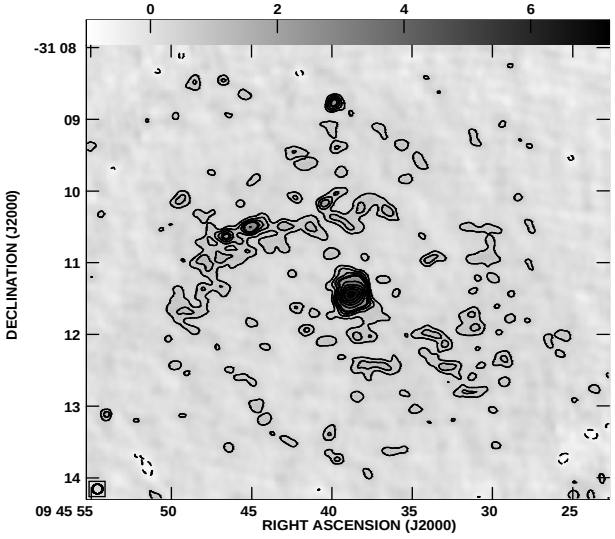

Fig. 4.3b : Medium resolution map with a beam size of 8" and the grey scale map with the contours are shown. The peak brightness is 7.2 mJy. The rms σ is 0.2 mJy per beam area. the contours are at (-5, -3, 3, 5, 7, 9, 10, 15, 20, 25, 30, 35) $\times$ σ.

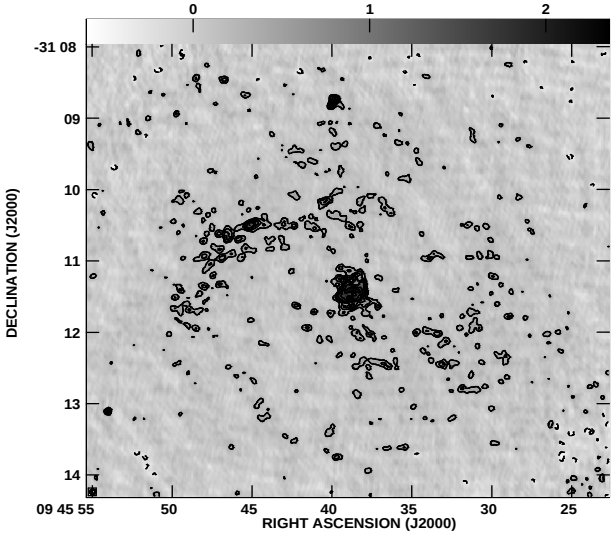

Fig. 4.3c : High resolution map with a beam size of 4" and the grey scale map with the contours are shown. The peak flux is 2.35 mJy. The rms σ is 0.1 mJy, the contours : (-5, -3, 3, 5, 7, 9, 10, 15, 20) $\times$ σ

Figure 4.3: The total intensity map of NGC 2997 at 1272 MHz

distribution in all the three images at 1280 MHz shows a clear spiral pattern similar to that of optical spiral pattern with the two dominant spiral arms. The nucleus is centered at RA=$09^h45^m38.75^s$, DEC= $-31°11'26.40''$ J(2000) with the position errors in RA and DEC less than 0.04^s and $0.6''$ respectively. The integrated flux density on the nucleus (1.76 kpc in size) is 49.4 mJy. As shown by our previous total intensity maps at 325 MHz and 610 MHz, all the 1280 MHz maps show a bright point source at the north, situated at RA=$09^h45^m39.85^s$, DEC= $-31°08'48.47''$ (J2000). Also, the gap of radio emission is present in the south spiral arm near the region RA=$09^h45^m33^s$, DEC= $-31°10'$ (J2000). In all the fig.4.3 images, east component ($43''$ by $29''$ in size) at the end of north-spiral arm is centered at RA=$09^h45^m49.13^s$, DEC= $-31°11'37.5''$ (J2000). The 1280 MHz maps have clear radio features of bifurcation of the southern arm towards the west, which starts at RA=$09^h45^m32.96^s$, DEC=-$31°12'25.26''$. The fig. 4.3-b,c show a horizontally elongated component situated in the southern arm which is 3.67 kpc ($60.28''$) distance from the central nucleus and the position of this component is RA=$09^h45^m37.36^s$, DEC= $-31°12'26.86''$ (J2000).
A low resolution 1280 MHz radio contour map in fig.4.3a reveals the extended component of radio emission overlying on the compact red lump of HII region seen in the optical image. This component gets resolved into two components as shown by the medium and high resolution maps in fig.4.3b and 4.3c and the brightest component is centred at RA=$09^h45^m45.36^s$, DEC= $-31°10'35.5''$. The prominent north-east discrete component is present in all the three maps at 1280 MHz, positioned at RA=$09^h45^m49.41^s$, DEC= $-31°10'07.63''$ (J2000) and lying roughly above the elongated radio emission of northern spiral arm centered at the red lump of HII region. The size of this discrete component is $\lesssim$ 0.9 kpc, and the integrated flux density is around 3.7 mJy. It is the same radio component seen in the medium resolution map at 610 MHz and 325 MHz maps.The south-east extended faint emission component seen in fig 4.1b and 4.2b also appears in 1280 MHz maps, the integrated flux density measured over the 3σ contour level being 11.17 mJy.

Summary of the Radio Continuum Structure

The total intensity maps of NGC 2997 at various spatial scale resolutions shown in figures 4.1, 4.2, and 4.3 are made from data sets observed at different frequency bands of the GMRT on different dates (refer table 4.1). The data set obtained at each observing band has its own limitation due to the uv-coverage, spatial resolution and possible residual errors which could not be eliminated. To check the reliability of the discrete sources in the galactic disk and the faint extended emission components of the spiral arms, we made at least two maps with spatial resolution of $8''$ or $29''$ and $15''$ at each observing band by using the uv-taper and the weighting function (refer table 4.1). Thus, while summarizing the radio continuum features, we assume a feature to be real if it is observed at more than one frequency band or if it is present in another independent observation using a different telescope. The GMRT and VLA total intensity images at λ20 cm with the same resolution of $18''$ are shown in figure 4.4. The VLA observation was done by H.Men and J.L.Han (2005) at 1435.1 MHz and 1652.4 MHz using BnC array.

The total intensity GMRT maps presented in this section show remarkable positional coincidence between four to six regions including the nuclear source. Some discrete sources and radio emission features of NGC 2997 are also shown with the help of numbered tags in fig.4.4. In table 4.9, we have summarized their positions, size, observed flux densities, etc. The overall summary of radio emission features in NGC 2997 is given below :

(i) The radio emission distribution in low-resolution image at each observing band

Figure 4.4: Total intensity maps of NGC 2997 at λ20 cm

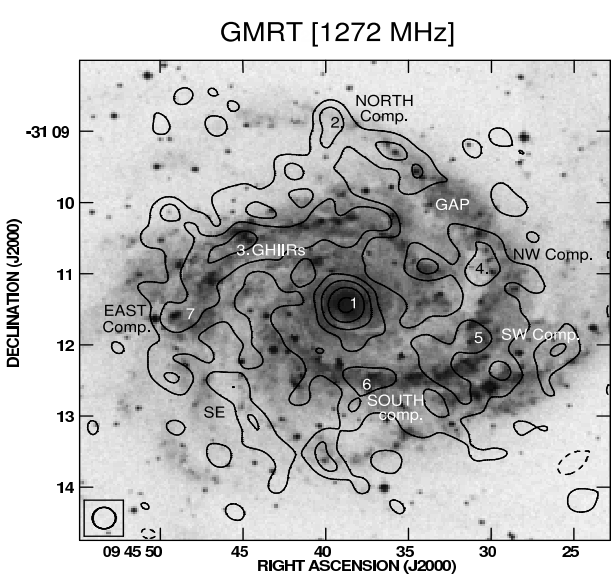

4.4a : Total intensity map at 1272 MHz with a resolution of 18″, superimposed on to an optical image from the Digitized Sky Survey. Contours : (-3,3,6,12,24,48)×σ. The rms $\sigma = 0.4$ mJy per beam area

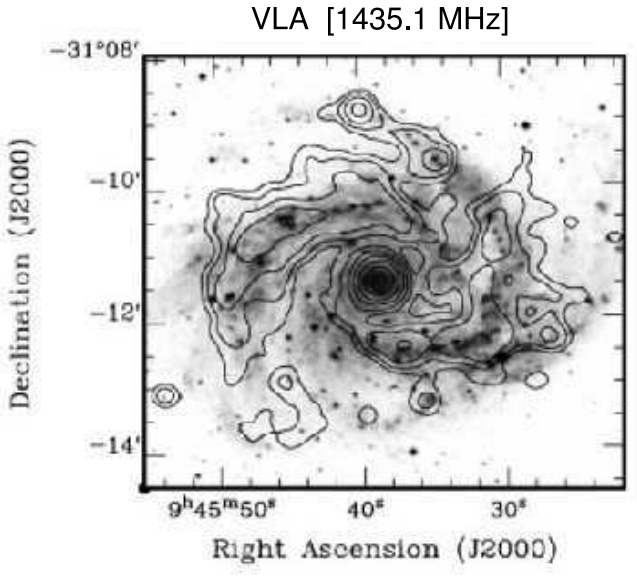

4.4b : Total intensity map at 1435.1 MHz with a resolution of 19″, superimposed onto an optical image from the Digitized Sky Survey. Contours : (-3,3,6,12,24,48,96)×σ. The rms $\sigma = 0.98$ μJy per beam area, (Ref : H.Men & Han,2005).

can be traced out to at least an area of 6.5′ by 8.1′ which is considerably larger than that of the optical extent, and more extensive than the VLA images at 20 cm by H.Men & Han,2005 (6.3′ by 5.8′), but is slightly less than the low-resolution image at 1.49 GHz by Condon J.J., 1987 ($\sim 7.3' \times 8.5'$).

(ii) All our total intensity maps show compact bright nucleus, less than 1.8 kpc (0.5′) in size and centered at, RA= $09^h45^m38.8^s$; DEC= $-31°11'25.55''$ (J2000). The uncertainty in RA and DEC is 0.5^s and 0.53″, respectively. The position is close to the values given in H.Men & Han (2005), Han (1999) : RA= $09^h45^m38.7^s$; DEC= $-31°11'27''$ (J2000), de Vaucouleurs et al.(1991) : RA= $09^h45^m39.4^s$; DEC= $-31°11'28''$, and DSS image : RA= $09^h45^m38.79^s$; DEC= $-31°11'27.88''$ (J2000).

(iii) The radio continuum emission from two spiral arms were clearly detected. The overlay of radio contour map over the optical image shows that the radio spiral arm is well aligned with the optical spiral arm. The structure of spiral arm shows Sc classification, originating from the small nucleus and covering the whole disk. The northern spiral arm shows intense extended region as compared to the southern arm.

(iv) A low-resolution image of 29″ at 610 MHz (Fig.4.2a) shows broad emission component centered at RA=$9^h45^m31.8^s$; DEC= $-31°12'34.8''$ (J2000), which almost overlies on the bifurcation of the southern arm towards the west into the third arm − seen in the optical image. The high resolution map at 610 MHz (Fig.4.2b), low and medium resolution maps at 1280 MHz also show the bifurcation feature clearly, being represented by two to three discrete components.
(v) A gap of radio emission in the southern arm near the region RA=$9^h45^m32.8^s$; DEC= $-31°10'$ (Northern-west part of the map) is seen in almost all the maps of NGC 2997 at the three frequencies. This region in the optical image appears blue, suggesting that there is an absence of star-forming region or blue light is coming from the hottest stars (O-A type of stars or old stellar sources like white dwarf). This gap is also seen in the VLA total intensity maps at λ20 cm, λ18 cm, and λ6 cm (J.L. Han et al., 1999; H.Men et.al, 2005). Also, abscence of magnetic field in the gap region is seen in the polarized intensity maps at λ6 cm and λ13 cm by J.L. Han et al.(1999).
(vi) In all the figures of NGC 2997 except Fig. 4.1a, a bright compact source is seen at RA= $09^h45^m39.9^s$;DEC= $-31°08'50.0$" north of the galaxy, where it's optical counterpart does not exist. This feature is similar to previous VLA observations by H.Men & Han, 2005 and Han, 1999.
(vii) There is an intense region of compact emission situated in the northern spiral arm, centered at RA= $09^h45^m45.07^s$;DEC= $-31°08'33.4$". This compact region shows exact positional coincidence between the giant HII region identified by V.Firpo et al. (2005) using the Clay telescope, LCO at the 6.5m. The H_α image of NGC 2997 by C.Feinstein shows similar intense region at this location. Hence, the emission from this compact source must be from an active star-formation region. Our high resolution image at 1280 MHz resolved this region into two components as shown in fig.4.3b,c.
(viii) The medium and high resolution maps (fig. 4.3b,c) at 1280 MHz shows a faint point source of $\sim$ 1.85 mJy, situated at RA=$09^h45^m54.11^s$, DEC= $-31°13'07.22''$ (the lower east-edge of map). The same faint source also appears in the VLA total intensity maps at λ21 cm, λ18 cm, and λ6 (H.Men & J.L. Han,2005; Han, 1999).
(ix) The Fig.4.2b, 4.3a show an extended faint emission feature at the south-east near the region RA=$9^h45^m44^s$, DEC= $-31°13'50''$ (J2000), which has also been seen in the total intensity and the polarized intensity VLA maps at λ6 cm (Hans, 1999).
Global radio continuum properties :
The total flux density value at each observing frequency is obtained by direct integration on the low resolution map, over a region above 3σ contour level to reduce the statistical errors. The total flux density values with the luminosities are given in the table 4.2.
The global spectral index values determined from the total flux densities indicates a flatter spectral index towards low frequencies. The low-frequency spectra of many normal spiral galaxies with only moderate surface brightness (Israel & Mahoney 1990), appear to be flattened slightly in the range 0.1-1 GHz; they proposed free-free absorption by very cool ($T_e < 1000$ K) ionized gas filling a large fraction of the radio emitting volume to explain their low-frequency spectra.
can be occured due to thermal abosorption, The radio-selected samples of *nor-*

Table 4.2: Global radio continuum properties of NGC 2997

	332.43 MHz	616.563 MHz	1272.688 MHz
Flux density (mJy)	1134 ±111	730 ±22	367 ±8
Spectral Power ($10^{21} W\,Hz^{-1}$)	18.45 ±1.7	11.88 ±0.3	5.97 ±0.1
Global Spectral Index	$332 \rightarrow 616 : -0.71$	$616 \rightarrow 1272 : -0.94$	$332 \rightarrow 1272 : -0.84$

mal galaxies are also characterized by the FIR/radio flux density ratios (Condon J.J, 1992). Halou et al. (1985) defined the parameter q as a logarithmic measure of the FIR/radio flux density ratio. From the IRAS surveys (A.J.Fitt et al., 1992) at 60-μm and 100-μm the flux densities of NGC 2997 are 32.28 Jy and 85.14 Jy, respectively. For more general comparisons, the $\hat{q}_{FIR}$ is defined as $\hat{q}_{FIR} = log\{S_\nu(FIR)/[S_\nu(\nu_{rad}) \times (\nu_{rad}/1.4GHz)^\alpha)]\}$ (A.J.Fitt et al., 1992), where, α is the radio spectral index ($S_\nu \propto \nu^{-\alpha}$). Using least-squares fit, average spectral index for the observed flux densities is computed to be -0.79 ±0.07. Using our integrated flux densities and the IRAS FIR flux density measurements for NGC 2997, $\hat{q}_{FIR}$ parameter is derived for each frequency which is 2.19±0.03. The NGC 2997 has far-infrared/radio ratio $q = 2.18$ at 1.2 GHz, which is near the mean for spirals $\hat{q}_{FIR} \approx 2.30$, with the rms scatter $\sigma_{\hat{q}} \lesssim 0.2$.

4.1.2 NGC 4565

The edge-on galaxy NGC 4565 is classified as late- to intermediate-type (Sb) galaxy, seen at an inclination angle of more than 85.°5. The optical parameters of the galaxy are summarized in table 1.3. NGC 4565 has an intermediate star-formation level like NGC 3044 and NGC 5907. SFR and SN rate are similar to our galaxy (DLG95). In NGC 4565, Hummel et al.(1984) could find only marginal indications of the existence of radio halo emission. The distance to NGC 4565 is 10.2 Mpc, so 1' corresponds to 2.96 kpc in linear scale.
The total intensity maps of NGC 4565 are presented in two sets, low resolution maps shown in figure 4.5 are restored with the circular Gaussian beam of 45″ in size, and overlaid on an optical image by Digitized Sky Survey. Another set of high resolution maps depicted in the figure 4.6 are restored using circular Gaussian beam of 20″ in size. The map parameters for both sets are given in table 4.3. The observed radio dimension of NGC 4565 by E. Hummel (1984) at 1.41 GHz is $10.'5 \times 1'.5$, at 10% level. Our total intensity maps at 1280 MHz suffers due to lack of short-spacings. Hence, we have interpreted our observation mainly based on the maps at 325 MHz and 610 MHz.

Low resolution maps

In the low resolution maps (fig.4.5) the extent of radio emission of the galaxy in the direction of the major axis is significantly less than the optical extent, but along the minor axis it seems to be comparable to the optical extent. Low resolution maps

Fig.4.5c : The total intensity map at 333.62 MHz, overlaid on Digitized Sky Survey's optical image. The peak brightness is 62.91 mJy. The rms σ is 3 mJy per beam area, the beam size is indicated at the BLC. Contour levels are (-5, -3, 3, 5, 6, 7, 9, 10, 15, 20) $\times$ σ.

Fig.4.5b : The total intensity radio map at 610 MHz superimposed on DSS optical image. The peak brightness is 33.61 mJy. The rms σ is 0.8 mJy per beam area, the beam size is indicated at the BLC. Contour levels are (-5, -3, 3, 5, 6, 7, 9, 10, 15, 20, 25, 30, 35, 40) $\times$ σ.

Fig.4.5a : The radio contours of the total intensity at 1280 MHz superimposed on Digitized Sky Survey's optical image. The peak brightness is 15.75 mJy. The rms noise in the map, σ is 0.7 mJy per beam area, the beam size is indicated at the BLC. Contour levels are (-5, -3, 3, 5, 6, 7, 9, 10, 15, 20) $\times$ σ.

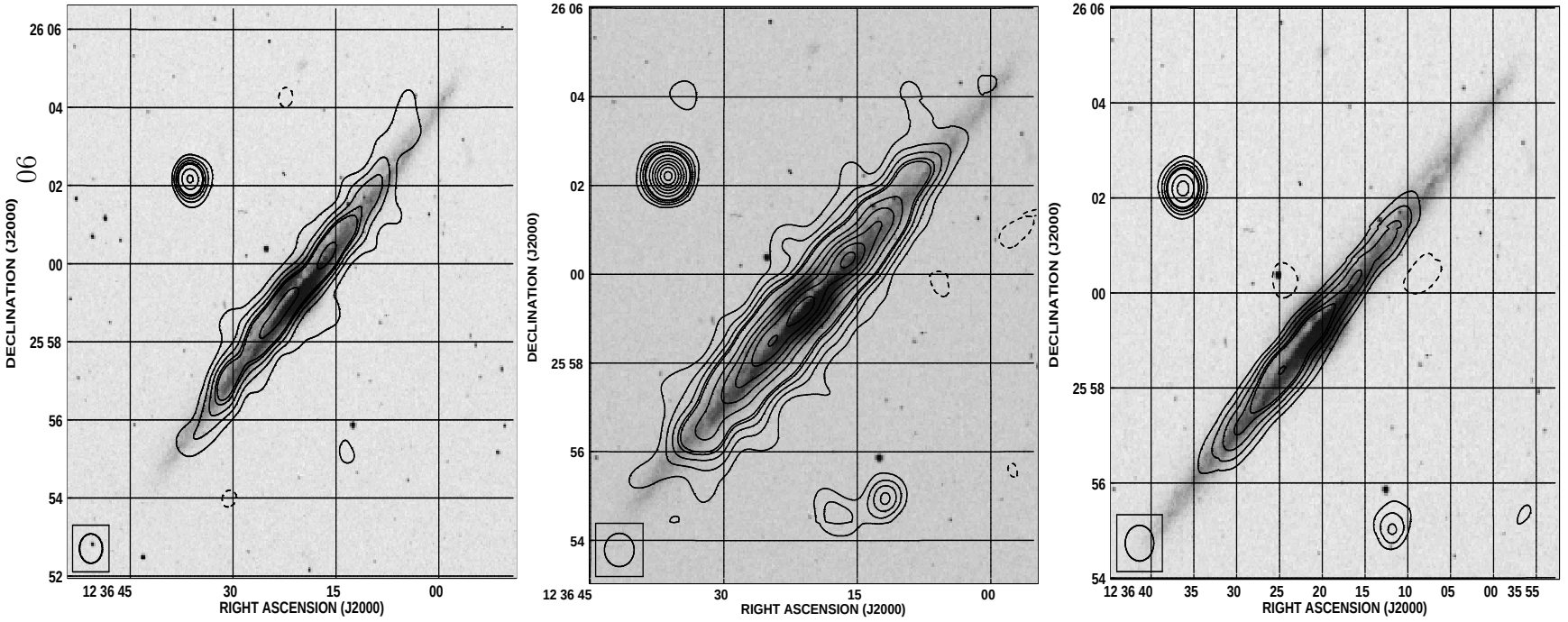

Figure 4.5: The total intensity map of NGC 4565 at low resolution (45″)

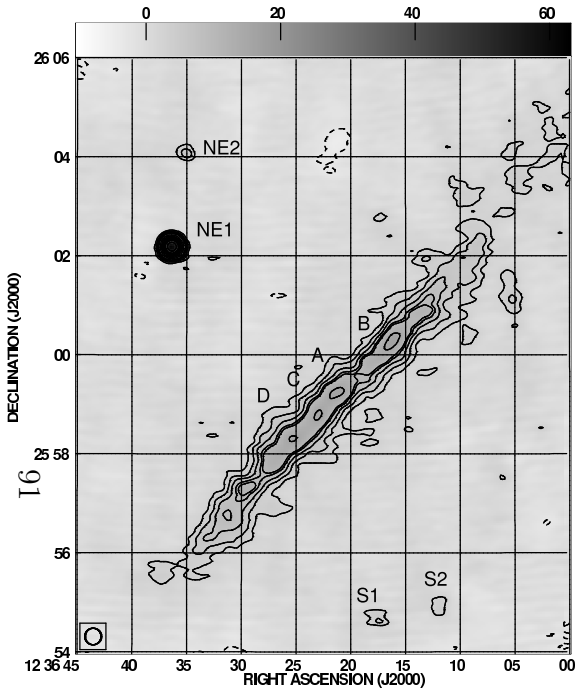

Fig. 4.6c : Shows total intensity map at 333.62 MHz with grey scale and radio contours. The peak brightness is 61.48 mJy. The rms σ is 1 mJy per beam area, the beam size is indicated at the BLC. Contour levels are (-5, -3, 3, 5, 6, 7, 9, 10, 15, 20,25,30,35,40,45,50) $\times$ σ.

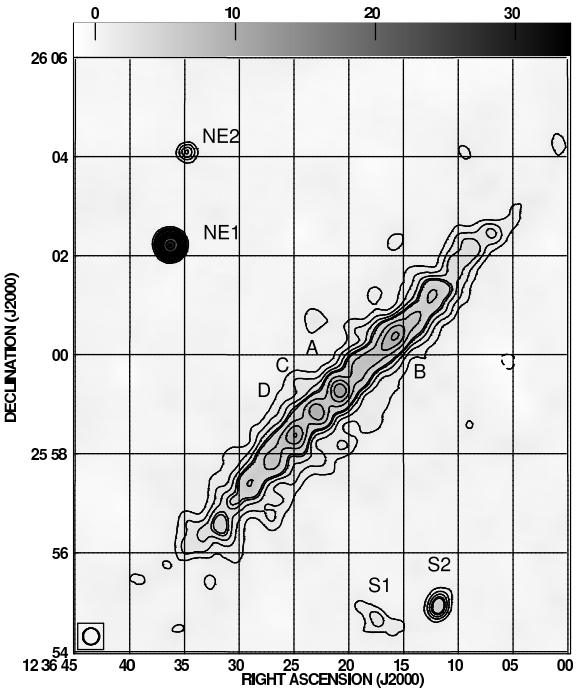

Fig.4.6b : The radio contour map with grey scale at 610 MHz. The peak brightness is 33.82 mJy. The rms σ is 0.4 mJy per beam area, the beam size is indicated at the BLC. Contour levels are (-5, -3, 3, 5, 6, 7, 9, 10, 15, 20, 25, 30, 35, 40,45,50,70) $\times$ σ.

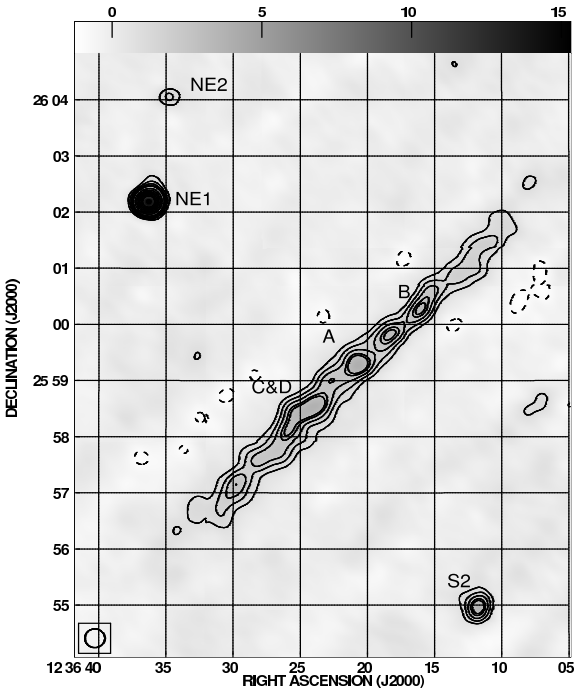

Fig.4.6a : The total intensity map at 1280 MHz with grey scale and contours. The peak brightness is 15.28 mJy. The rms noise σ is 0.3 mJy per beam area, the beam size is indicated at the BLC. Contour levels are (-5, -3, 3, 5, 6, 7, 9, 10, 15, 20, 25, 30, 35, 40, 45, 50) $\times$ σ.

Figure 4.6: The total intensity map of NGC 4565 at high resolution (20″)

Table 4.3: Map parameters of NGC 4565

Band Center† MHz	BW[a] MHz	Fig.	UV-taper $k\lambda$	Synthesized beam[b] arcsec^2	Restoring beam[c] arcsec^2	rms noise (mJy/beam)	Peakflux mJy
333	12.5	4.5c.	6	$45.8'' \times 35.9''$@70°	45	3	62.91
		4.6c.	0	$20.6'' \times 12.7''$@87°	20	1	61.48
617	12.5	4.5b.	7	$44.9'' \times 40.2''$@-63°	45	0.8	33.61
		4.6b.	34	$19.3'' \times 14.4''$@-63°	20	0.4	33.82
1287	13.75	4.5a.	4	$44.3'' \times 39.0''$@-27°	45	0.7	15.75
		4.6a.	16	$20.4'' \times 14.5''$@51°	20	0.35	15.28

†All maps are stoke I, and corrected for the shape of the GMRT primary beam.
The natural weighting was used for all the maps.
a. Final bandwidth for analysis after editing
b. Final synthesized clean beam, position angle with respect to major axis is given in degree.
c. Restoring beam is a circular gaussian with PA=0 degree, and the area is approximated to the gaussian clean beam area in square arcsec $\Omega_s = 1.13 * \beta_{maj} \times \beta_{min}$.

at 325 MHz and 610 MHz show two sources along the major axis, one, the central weak source which is extended in the southern direction, and the second, along the major axis located at a distance of 1.73 arcmin (5.12 kpc) from the central source − in the north-west half of the galaxy. The source in the north-west half of the galaxy is also seen in the total intensity maps of NGC 4565 at λ2.8 cm (M.Dumke et al.,1995) and λ20.3 cm (Sukumar & Allen, 1991). The peak intensities of both the sources, the central weak and the north-west, are the same at each observing frequency, which is 48.5±3.2 mJy/beam and 49.20±3.3 mJy/beam respectively at 325 MHz, and 28.4 ±0.9 mJy/beam for each source at 610 MHz. A map at 610 MHz (fig.4.5b) shows concentrated emission of thin-disk, and fainter emission from thick-disk which is extended to a large z-distance compared to the 325 MHz low resolution map. The 325 MHz total intensity map (fig.4.5a) shows a small deviation of the radio continuum emission from the principal plane of optical image, which is prominent in the northern half of the galaxy. E. Hummel et al.(1984) attributes this deviation as a warp in the HI and optical layer that are seen further out in the galaxy.

Figure 4.7 shows the radio emission distribution along the major- and minor-axis of NGC 4565 at 325, 610 and 1280 MHz. The emission distribution along the major- and minor- axis was obtained on regridded and smoothed maps at a common resolution by taking slices of data. A slice of $12'$ length was taken along the principal plane of the galaxy. In a similar way, a slice of $\sim 2.1'$ length was taken perpendicular to the major axis (i.e. in the Z-direction). The FWHM of the peak intensity (peak intensity value at 0 arcmin of fitted Gaussian) at each observing frequency is given in the table 4.5. For general comparison of the radio emission distribution along the major-axis, we have normalized the observed flux by the peak flux value at 0 arcmin obtained from a gaussian fit (see fig.4.7). The radio emission distribution at 325 and 610 MHz show two peaks of equal intensities which are separated by about 1.7 arcmin distance,

Figure 4.7: Radio emission distribution along the Major-axis and Minor-axis

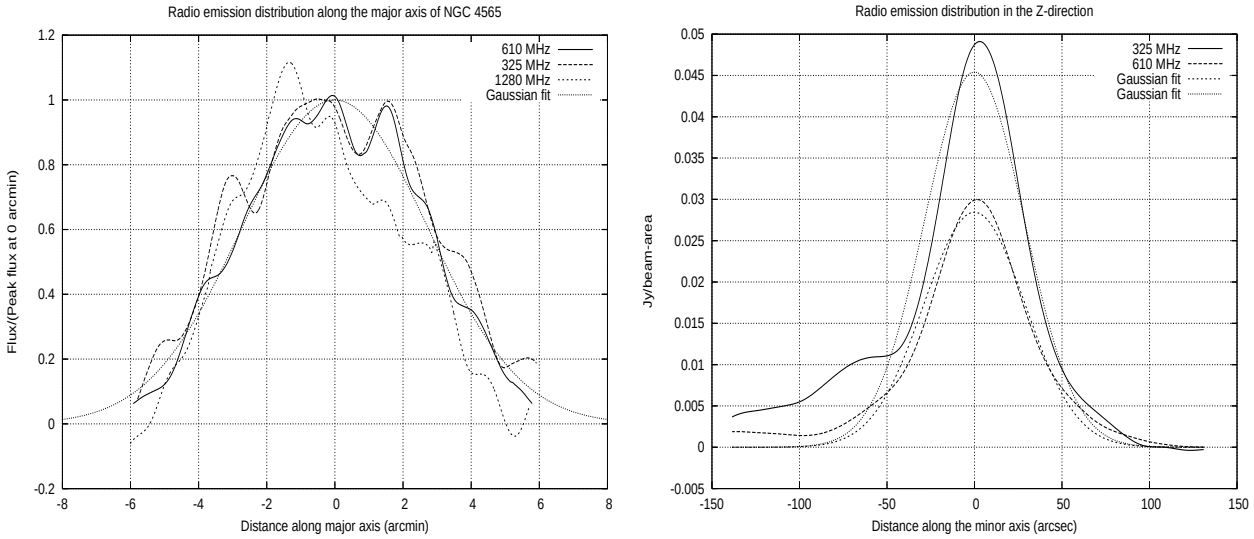

one of them being centered at our observing center coinciding with the peak of the central source of the galaxy and the other peak being for the north-west component. Between these two peaks, a dip was observed in the 325 MHz and 610 MHz data which lies $\sim 44''$ away from the centre. This peculiar brightness distribution has also seen in WSRT-610 MHz map of E. Hummel et al.(1984) at their assumed center for the galaxy : RA= $12^h34^m00^s$, DEC= $26^d15'00''$ (B1950). After regridding our observing co-ordinates to the epoch of mean coordinates 1950 (i.e. Basselian-B1950), the B1950 coordinates are RA= $12^h33^m52.04^s$, DEC= $26^d15'46.068''$, which is close to the values given by M. Dumke (1995): RA= $12^h33^m52.00^s$, DEC= $26^d15'47''$. Hence, our observing center for NGC 4565 differs from the observation of E.Hummel et al.(1984), and suggests that the dip is not exactly situated at the center of galaxy.

High resolution maps

In our high resolution maps (fig.4.6), the central source (marked as 'A') along the major axis is located at RA= $12^h36^m20.8^s$, DEC= $25^d59'16.38''$ (J2000), the uncertainties in RA and DEC are $\pm 0.17^s$ and $\pm 2''.18$, respectively. This value is close to the position of the center given by Laurent-Muehleisen S.A et al. (1997) : RA= $12^h36^m20.8^s$, DEC= $25^d59'16''$ (J2000).
To check the observed radio dimensions (FWHM) of NGC 4565 in the low resolution maps which may have been affected by beam broadening, we measured the radio dimensions in the high resolution maps of $20''$, which were smoothed and regridded to a common resolution. The slice data were taken along the major and minor axis of NGC 4565 map at 325 MHz and 610 MHz which shows that the radio dimensions are $395'' \pm 1.3'' \times 37.7 \pm 1.7$ and $370'' \pm 1.63'' \times 37.9 \pm 1.54''$ respectively. The radio dimensions of NGC 4565 at 1414 MHz measured by A. H. Broeils and R.Sancisi(1985) using the WSET with the synthesized beam of $13'' \times 30''$ are $375'' \times 39''$. Hence our

values measured at high resolution maps are close to this value.
The high resolution maps at 325 MHz and 610 MHz reveals that the central source extended in south-west half of the galaxy gets resolved into three components which are marked as 'A', 'B' and 'D' respectively in the figure 4.2. The flux densities, peak-intensities, and positions for these sources were found by 2-D gaussian fit which are mentioned in the table 4.4. The north-east source along the major axis (marked as 'B') is relatively brighter than the source 'A' at 325 MHz, whereas in the 610 and 1280 MHz map, it is relatively weak as compared to the central source. The north-east source along the major axis (marked as 'B') is relatively brighter than the source 'A' at 325 MHz, whereas in 610 and 1280 MHz map, it is relatively weak as compare to the central source. Whereas, the spectral index distribution for source 'B' clearly indicates its nonthermal nature with spectral index value around ~ -0.8, we suspect that component 'B' may be a radio supernova, like presence of a radio supernova SN 1986J (0.07Jy; Allen et al.1978) observed in NGC 891 towards south-west side of the nucleus.
Two point sources in the North-East corner of each high-resolution map (marked as NE1 and NE2) are located respectively at RA=$12^h36^m36.^s29$, DEC= $26°02''12.52''$ and RA=$12^h36^m34.^s77$, DEC=$26°04''5.11''$. The observed GMRT low-frequency spectra for these sources indicates that these are steep spectrum sources with spectral index value $\alpha \sim -1.0$. These two north-east point sources have also been seen in the WSRT 1.4 GHz map (E.Hummel,1984) and in the VLA λ20.3 cm map by Sukumar & Allen (1991). The high-resolution maps at 325 MHz and 610 MHz show two sources near the southern edge of the map, marked as S1 and S2. In the 1280 MHz map we did not see the presence of S1 source. The flux densities measured on the S2 source indicates that this source has flatter spectra, the spectral index value obtained between 325-610 MHz and 610-1280 MHz is $\alpha \sim -0.3$. The WSRT 1410 MHz map also shows the presence of only one source, but in the VLA $\lambda 20.3cm$ map, the presence of both the southern sources are seen.

The radio brightness distribution at 325 MHz and 610 MHz along the major axis of NGC 4565 (using the high resolution maps) is shown in the figure 4.8, the upper panel shows the spectral index distribution ($\alpha_{325-610}$) along the major axis. The figure shows the north-west component and the three components for the sources seen in the southern-half of the galaxy. Also, it clearly reveals the dip which was observed in the low-resolution map. The spectral index distribution between 325 MHz and 610 MHz along the principal plane (using the slice data) shows a trend of flatter spectrum for source 'A', source 'C', and for the observed dip.

Summary of radio continuum structure of NGC 4565

(1) The total intensity maps at 325 MHz and 610 MHz overlaid on the optical DSS image (fig.4.1) shows that the distribution of radio emission has two components, one being concentrated along the principal plane of galaxy and showing the radio emission from the thin disk, and the other radio emission component represents the thick-disk radio emission which is smooth and extended in the z-direction.
(2) The low resolution maps at 325 MHz and 610 MHz show two sources along the

Table 4.4: Sources along the major axis of NGC 4565

Source	Observed positions 610 MHz $\alpha_{2000} = h\,m\,s\ \pm s$ $\delta_{2000} = {}^\circ\ {}'\ {}''\ \pm''$	Integrated flux densities (mJy) & Peak intensities (mJy/beam) at 325 MHz	610 MHz	1280 MHz	Comments
A	12 36 20.82 ±0.0 25 59 16.38 ±0.6	100.7 ±10 15.8 ±1.4	39.8 ±1.7 11.0 ±0.4	11.9 ±1.3 03.7 ±0.3	Central Source
B	12 36 16.17 ±0.1 26 00 17.69 ±1.5	111.7 ±11 15.8 ±1.4	61.5 ±2.7 9.8 ±0.4	10.8 ±1.4 3.1 ±0.3	North-West component
C	12 36 22.93 ±0.0 25 58 50.68 ±0.7	101.6 ±16 15.4 ±1.4	41.8 ±2.1 9.2 ±0.4	30.9 ±3.0 3.5 ±0.3	
D	12 36 25.25 ±0.0 25 58 18.52 ±1.0	95.0 ±15 15.0 ±1.3	40.4 ±1.9 9.7 ±0.4	– –	
	Other sources in the field				
NE1	12 36 36.29 ±0.0 26 02 12.52 ±0.2	62.3 ±2.7 61.3 ±1.5	34.1 ±0.7 33.1 ±0.4	16.0 ±0.6 15.3 ±0.3	Nonthermal Source
NE2	12 36 34.77 ±0.0 26 04 05.11 ±1.0	62.0 ±2.6 63.6 ±1.5	35.6 ±0.7 38.1 ±0.4	17.4 ±0.6 16.1 ±0.3	Nonthermal Source
S2	12 36 11.82 ±0.0 25 54 56.28 ±1.1	8.0 ±3.9 4.3 ±1.4	8.8 ±1.0 5.25 ±0.4	5.7 ±0.8 3.5 ±0.4	Flat spectrum source

Figure 4.8: Radio brightness distribution at 325 MHz and 610 MHz along the Major-axis

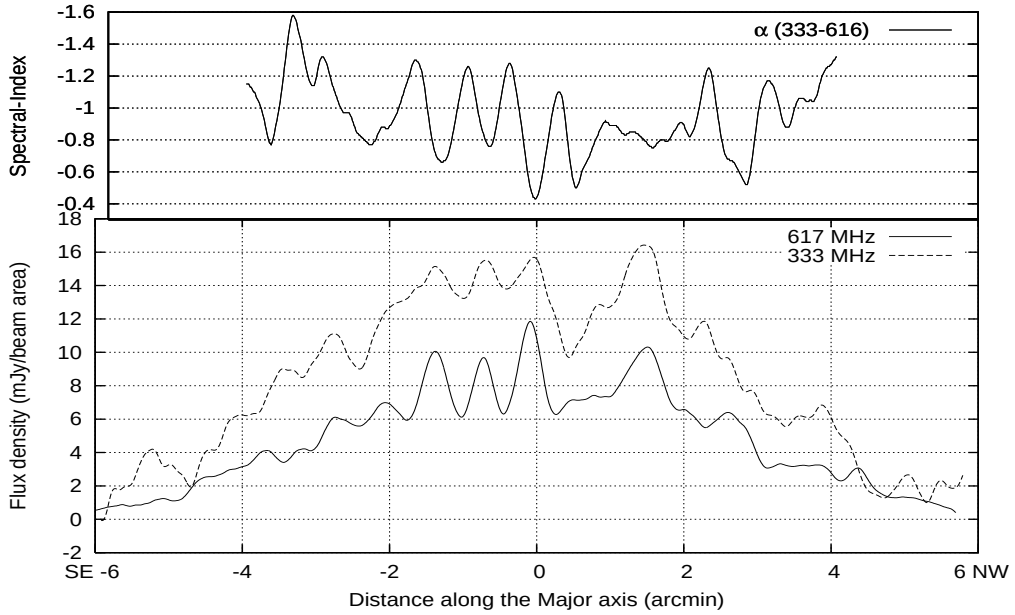

major axis of which one is a weak central source which is extended in the southern direction along the major axis, and the other prominent component in the North-East side, which is 1.7′ off the distance from the central source. A dip has been observed between these two sources at 325 MHz and 610 MHz in the low resolution maps as well as in the high resolution maps, which is roughly centered at RA= $12^h36^m19^s.42$, DEC=$25^d59'37.59''$(J2000). A contour map of the polarized intensities of NGC 4565 at λ2.8 cm (M. Dumke, 1995) shows abscence of magnetic field in this region. (3) The radio distribution of NGC 4565 in a low resolution map at 325 MHz shows small deviation from the principal plane of the major axis, which is prominent in the nothern-half of the galaxy. This kind of deviation has been seen at 1410 MHz map (E.Hummel et al.1984) and show suggestion of a warp to the north-west.
(4) In our high resolution maps (fig.4.6), NGC 4565 galaxy is centered at RA= $12^h36^m20.8^s$, DEC= $25^d59'16.38''$ (J2000), the uncertainties in RA and DEC are $\pm0.17^s$ and $\pm2''.18$, respectively. This value is close to the position of center given by Laurent-Muehleisen S.A et al. (1997). Using the high resolution maps of 20″, the radio dimensions (FWHM) of NGC 4565 are $395'' \times 37.7''$ and $370'' \times 37.9''$ at 325 MHz and 610 MHz, respectively. These values are close to the radio dimensions (FWHM) measured at 1414 MHz by A. H. Broeils : $375'' \times 39''$.
(5) The central source extending towards the south-west half of the galaxy gets resolved into three discrete sources in our high resolution maps at 325 MHz and 610 MHz. The spectral index distribution between 325 MHz and 610 MHz along the major axis (see fig.4.8) shows that sources 'A', 'C', and the dip have flatter spectral indices. Source 'B' is found to be nonthermal in nature.
(6) All high resolution maps depicted in the fig.4.6 show two steep spectrum ($\alpha \sim -1.0$) point sources (NE1 and NE2) located near the north-east corner, and southern source (S2) at the lower edge, which has flatter spectral index ($\alpha \sim -0.3$).

Global radio continuum properties :

The integrated flux density at each observing frequency was obtained over the 3σ

Table 4.5: Radio continuum properties of NGC 4565

	333.62 MHz	617.62 MHz	1490 MHz[a]
Flux density (mJy)	725 ±22	407 ±30	131
Spectral Power ($10^{21} W\,Hz^{-1}$)	8.5 ±0.25	4.8 ±0.35	1.5
Global Spectral Index	$333 \rightarrow 617 : -0.93$	$617 \rightarrow 1490 : -1.28$	$333 \rightarrow 1490 : -1.14$
Radio Dimension (arcmin)[b]			
Major axis, (FWHM)	7.2 ±0.04	6.41 ±0.023	7.0±0.00
Minor axis, (FWHM)	1.11±0.013	1.13±0.013	1.21±0.00

a. Flux density at 1.49 GHz used from Condon J.J.(1987).
b. Observed value for low-resolution maps of 45 arcsec, not corrected for beam broadening; 1.49 GHz VLA map at 60″ resolution (Condon J.J.,1987)

radio contour level and the values of the total flux densities and luminosities are given in table 4.5. The spectral index of NGC 4565 determined from our total flux density values including the total flux density at 1.49 GHz (Condon J.J,1987) is $\alpha = -1.14$

($S_\nu \propto \nu^\alpha$). This value is steeper than a spectral index $\alpha = -0.93$ found by E.Hummel et al.(1984). From the Far Infrared observations of NGC 4565 by the IRAS satellite (R.J. Wainscoat et al.1987), the flux densities of NGC 4565 at 60 μm and 100 μm are 11 and 65 Jy respectively. Using our integrated flux densities at 325 MHz and 610 MHz and the IRAS flux densites, the $\hat{q}_{FIR}$ parameter (see section 4.1.1 and eq.1.10) was found to be 2.37 and 2.30 at 325 MHz and 610 MHz. These values are consistent for the spiral galxies : $\hat{q}_{FIR} \approx 2.30$, with the rms scatter $\sigma_{\hat{q}} \lesssim 0.2$.

4.2 Spectral study

4.2.1 Total emission spectra measurement

Integrated flux densities of NGC 2997 and NGC 4565 obtained using GMRT at 325, 610, and 1280 MHz bands are given in tables 4.6-I and 4.6-II respectively. A low resolution map of NGC 2997 at each observing frequency covers an emission area about $6.5'$ by $8'$, the integrated flux densities are measured over this area. Our total flux density values of NGC 2997 at low-frequencies were not affected significantly due to the lack of short-spacings since the final uv-data sets have the short spacings which are sensitive to structures in the range of $13'$ to $57'$ (refer tables 2.2 & 2.1). Total flux density of NGC 4565 at observing frequencies were obtained from low-resolution maps depicted in fig.4.5 by integrating over an emission region above 3σ radio contour level. Due to lack of short-spacings, total flux density value at 1280 MHz obtained from our observation is less than the values at 1.4 GHz given by E.Hummel et al.(1984) and J.J Condon(1987). The GMRT integrated flux density of NGC 4565 at 610 MHz is close to a value measured by Hummel et al.(1984). The errors given in the observed flux densities are assumed to be quadratic sum of two terms. The first term is an error due to the calibration (this term has been estimated from the percentage of errors in the flux estimation of phase calibration given by GETJY), and the second term is due to the noise plus confusion, which has been evaluated from a statistical analysis of fluctuations found in random source free areas in the final cleaned map. Other published values of integrated flux densities for NGC 2997 and NGC 4565 are listed in tables 4.6-I and 4.6-II respectively.

The integrated spectrum of a galaxy can be subjected to an analysis to derive both, the relative amount of thermal emission at a certain frequency as well as the spectral index of the nonthermal emission. A more rigorous approach to separate synchrotron and bremsstrahlung (or free-free) radio emission in 31 samples of spiral galaxies by N. Duric et al.(1988) was to consider the synchrotron spectral index as a free parameter and composite spectra (thermal free-free plus synchrotron) are fitted to accurate interated flux densities over a large range of frequencies. We follow the same model given by N. Duric in which the integrated flux of a galaxy is entirely due to power law synchrotron radiation and optically thin bremsstrahlung emission from a 10^4 K photoionized gas,

$$S_\nu = A\nu^{\alpha_{nt}} + B\nu^{-0.1},$$

where S_ν is the integrated flux density at frequency ν, α_{nt} is the non-thermal spectral

index, A and B are measures of the relative contirbutions of the two forms of radiation. This model assumes that the thermal free-free radiation in the optically thin region, i.e. $S_\nu^{th} \propto \nu^{-0.1}$, the synchrotron radiation is optically thin every where, and the synchrotron & Compton losses are not too strong.
We fitted both, a composite and single power law model (i.e.B=0) to our data using the method of nonlinear least-squares. The best-fitting model spectra with the data of NGC 2997 and NGC 4565 spectrum are shown in figure 4.9.

1. NGC 2997 : A single power-law ($S_\nu \propto \nu^\alpha$) best-fitting model to the radio spectrum of NGC 2997 was obtained with the best fit value of spectral index $\alpha = -0.98 \pm 0.06$, which is close to the best-fit value $\alpha_{nt} = -1.10$ given by H.Men & Han J.L(2005). The best-curve fitted to a single power law indicates that no thermal flux is present to within the errors of the fit. The composite spectra model fitted to the radio data of NGC 2997 did not give better result where we got the negative value for thermal fraction (see fig 4.9a).
Assuming the measured flux densities at our observing frequencies for NGC 2997 to fall within the non-thermal regime of the spectrum where the thermal fraction should be very small, we fitted a power-law to only the low-frequency GMRT spectrum and the best fit value obtained is $\alpha_{nt} = -0.796 \pm 0.071$. Condon & Yin (1990) estimated a global thermal fraction for most of the normal galaxies, which is : $S/S_{th} \sim 1 + 10\left(\frac{\nu}{GHz}\right)^{(0.1-|\alpha|)}$, where α is a typical nonthermal spectral index, S is the total flux density, and S_{th} is the flux density due to the thermal component. Taking, $\alpha = -0.796$, thermal fractions derived at 1272 MHz, 616 MHz and 332 MHz are 10.33%, 6.08% and 3.58%, respectively, of the measured total flux density value at each observing band. We found the intensity of the thermal emission to be almost the same, being about 40 mJy, in all our three observing bands. Independent constraint on the average thermal fraction of the normal galaxies from FIR/radio correlation study for normal galaxies (condon & Yin,1990) and from observed ratios of $S_{1.4GHz}/F(H_\alpha)$ of normal disk galaxies (Kennicutt,1993), puts the upper limit for the thermal fraction $\langle S_{th}/S \rangle \lesssim 0.1$ at 1.4 GHz; accordingly our flux-density measurement at 1272 MHz is consistent with this limit and the thermal fraction S_{th}/S at 1.272 GHz is 0.10 for NGC 2997.
Considering the small value of the thermal fraction in the total emission of NGC 2997 at low frequencies and assuming that the spectral power given in the table 4.2 is due to nonthermal origin, we estimated the supernova rate (yr^{-1}), the average star-formation ($SFR(M \gtrsim 5M_\odot)$ $M_\odot\, yr^{-1}$) and the ionization rate ($N_{uv}\, s^{-1}$) which is given in the table 4.8 (refer section 1.3.4 & 1.3.5 for details). To see the effect of the thermal contribution in calculating these parameters, we subtracted the derived thermal fraction from each total emission data points at our observing bands, and again parameters were calculated which did not show any significance difference.

2. NGC 4565 :
Both the best-fitting model spectra (composite spectra and single spectra) are shown, using the NGC 4565 data, in Fig. 4.9b. In the case of NGC 4565 radio spectrum, the least-square error for the composite spectra is 0.0096, as compared to the single spectra (0.010). Hence, we considered the composite-spectra model with the best fit

Table 4.6: Total flux densities

4.6-I. Radio spectra measurements of NGC 2997 :

Frequency GHz	Flux density Jy	Reference
8.460	0.034 ±0.004	VLA, J.L.Han et al.(1999)[a]
5.010	0.092 ±0.010	Whiteoak,J.B. (1970)
4.860	0.067 ±0.011	VLA J.L.Han al.(1999) [a]
4.850	0.141 ±0.014	THE PARKES-MIT-NRAO (PMN) Surveys VIII Source catlog for the zenith 1996 ApJS 103..145W
1.652	0.128 ±0.015	H.Men & J L Han (2005)
1.543	0.255 ±0.020	VLA J.L.Han al.(1999)
1.490	0.290	J.J. Condon (1987) VLA
1.435	0.195 ±0.011	H.Men & J L Han (2005)
1.400	0.235 ±0.010	NVSS GRP- VLA (1993)
1.280	0.367 ±0.008	Our observation
0.610	0.730 ±0.022	Our observation
0.325	1.134 ±0.111	Our observation

a.Lower limits, because of missing spacing problems.

4.6-II. Radio spectra measurements of NGC 4565 :

Frequency GHz	Flux density Jy	Reference
10.70	0.020 ± 0.007	Gioia et al.(1982)
10.55	0.028 ± 0.003	M. Dumke et al (1995)
4.80	0.044 ± 0.010	Gioia et al.(1982)
1.40	0.1425	NVSS GRP (1993) VLA
1.49	0.131	J.J. Condon (1987)
1.41	0.150 ± 0.010	E Hummel et al (1984)
1.28	0.0746 ± 0.08	Our observation [a]
0.84	0.205 ± 0.060	Israel and van de Hulst (1983)
0.610	0.337 ± 0.048	E Hummel et al (1984)
0.610	0.407 ± 0.030	Our observation
0.43[b]	0.350 ± 0.100	Lang and Terzian (1969)
0.43	0.450 ± 0.090	Israel and van der Hulst (1983)
0.41[b]	0.280 ± 0.015	Gioia and Gregorini (1980)
0.325	0.725 ± 0.022	Our observation.

a. Less flux due to lack of short spacings. b. Neglected

Figure 4.9: The Radio continuum spectra

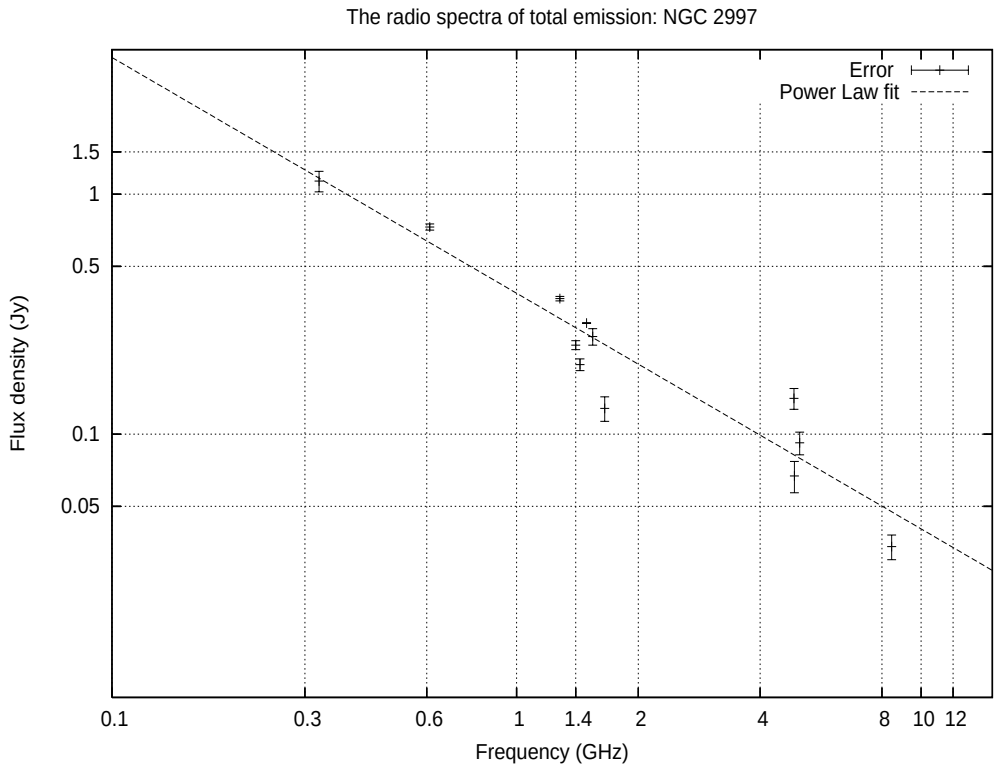

4.9a : The total emission spectra of NGC 2997

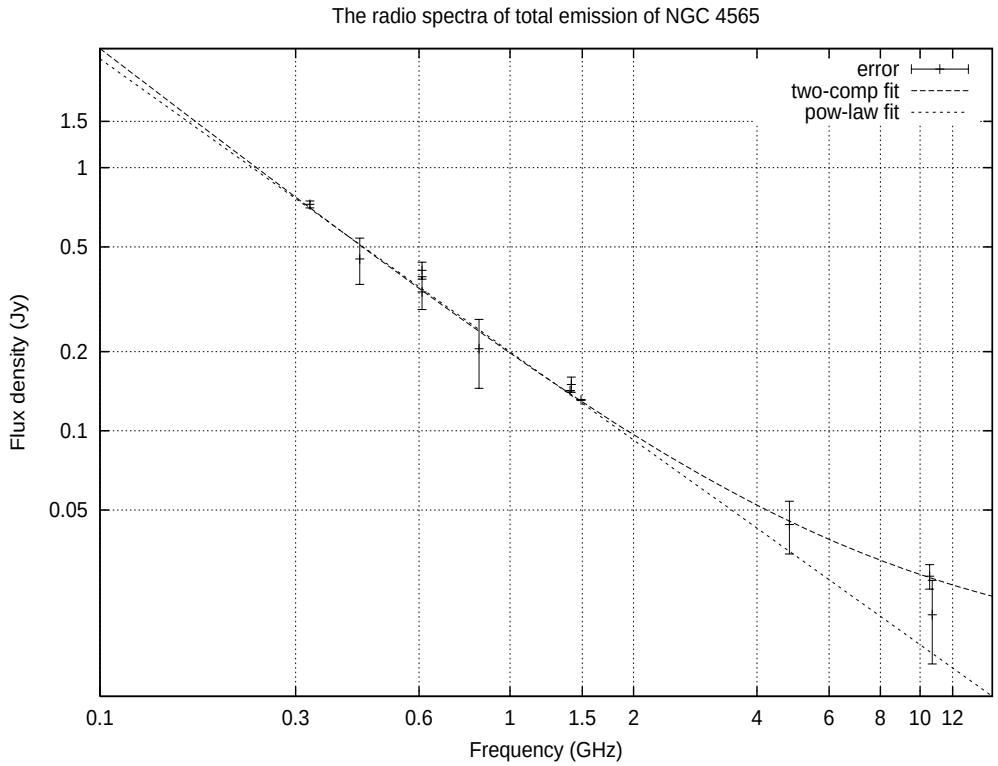

4.9b : The total emission spectra of NGC 4565

value of non-thermal spectral index, $\alpha_{nt} = -1.19 \pm 0.16$ for further interpretation. The value of α_{nt} is steeper than the mean value $\langle\alpha_{nt}\rangle = -0.83 \pm 0.02$ obtained for a sample of 74 galaxies by Niklas et al.(1997). Also, it is slightly steeper than the previously obtained spectral index values for NGC 4565 radio spectrum, which are -0.965 ± 0.002 (N. Duric et al.,1988) and -0.93 ± 0.08 (E.Hummel et al.,1984).
In table 4.7, we have listed the derived thermal flux density (column 2: T), synchrotron flux density (column 3: N), thermal fraction (column 4: T/(T+N)) and the ratio of thermal to synchrotron flux density (column 5: T/N) at each observed frequency of NGC 4565. Along with these derived parameters, we also gave the thermal fraction (column 6: S_T/S) and thermal flux density (column 7: S_T) using the equation by Condon & Yin (1990) and taking the nonthermal index $\alpha_{nt} = -1.19$ (see section 1.3.1). The values of thermal flux densites are noticeably equal between 4.8 GHz to 0.8 GHz data, and at our 610 MHz data. Note that in table 4.7, the derived

Table 4.7: Thermal and nonthermal flux densities for NGC 4565

Freuqency (GHz)	T (Jy)	N (Jy)	T/(T+N)	T/N	S_T/S	S_T (Jy)
10.700	0.017	0.010	0.630	1.700	0.680	0.014
10.550	0.017	0.010	0.630	1.700	0.676	0.019
4.800	0.018	0.027	0.400	0.667	0.431	0.019
1.400	0.020	0.117	0.146	0.171	0.134	0.019
1.490	0.020	0.109	0.155	0.183	0.143	0.019
1.410	0.020	0.116	0.147	0.172	0.135	0.020
0.840	0.022	0.216	0.092	0.102	0.074	0.015
0.610	0.022	0.318	0.065	0.069	0.050	0.017
0.610	0.022	0.318	0.065	0.069	0.051	0.021
0.430	0.023	0.483	0.045	0.048	0.033	0.015
0.325	0.024	0.676	0.034	0.036	0.024	0.017

thermal fraction at 1.4 GHz is about 0.1, which is consistent with the upper limit set for averaged thermal fraction of normal galaxies by Condon & Yin (1990) and Kennicutt (1983).
The estimated values of the radio supernova rate, average star-formation rate ($M_\odot\, yr^{-1}$) and the production of Lyman continuum photons (s^{-1}) for NGC 4565 is given in table 4.8, to calculate these parameters (see section, 1.3.4 & 1.3.5), we used non-thermal spectral power derived at our observing frequencies which also includes 1.49 GHz data from Condon J.J.1987 (Since observed GMRT integrated flux densitiy at 1.272 GHz is less).

Radio counts of young Galactic SNRs suggest a radio supernova rate of 0.013 yr^{-1} (CasWell & Lerche,1979) or Type II supernova rate $\nu_{SN} \sim 0.023\, yr^{-1}$ estimated by Tammann(1982). The radio supernova rate in NGC 4565 estimated by us is close to the values given for our Galaxy. Our data suggest that the radio supernova rate in NGC 2997 is a factor of three to four times higher than that of our Galaxy and the NGC 4565. The production of Lyman continuum photon rate of the Galaxy is 2×10^{53}

Table 4.8: The estimated parameters for NGC 2997 and NGC 4565

	NGC 2997	NGC 4565
1. The radio supernova rate (yr^{-1})	0.058	0.016
2. Star-formation rate [SFR($M \gtrsim 5M_{\odot}$)] ($M_{\odot}yr^{-1}$)	1.44	0.39
3. The ionization rate [N_{uv}] (s^{-1})	5.01×10^{53}	1.36×10^{53}

photons s^{-1} (Gusten and Mezger,1982). Our estimation of Lyman continuum photon production rate in NGC 4565 is 30% less than that of our Galaxy. The derived star-fomration rate in NGC 4565 and NGC 2997 suggest that these galaxies are normal galaxies with intermediate star-formation (SF) levels where the disk-halo interactions occur only in a few locations where the local SFR is high. The derived values of star-formation rate and the production of Lyman continuum photon rate of NGC 2997 and NGC 4565 are comparatively less than the values derived for M82 by Condon J.J.(1992). For M82, the star-formation rate SFR($M \gtrsim 5M_{\odot}$) is $\sim 2.2M_{\odot}\, yr^{-1}$, the ionoization rate is $N_{uv} \sim 8 \times 10^{53}\, s^{-1}$ and the radio supernova rate is $\nu_{SN} \sim 0.1\, yr^{-1}$.

4.2.2 Spectral index Maps : NGC 2997

To determine the accurate spectral index ($S_{\nu} \propto \nu^{\alpha}$) distribution over the disk region of galaxy, we used the maps of identical beam pattern by UV tapering and weighting; Fig. 4.1a, 4.2b, and 4.3c shows similar spatial resolution maps which are restored with 15″ circular gaussian beam. To reduce the statistical errors, all the three maps were smoothed to the same grid, convolved with the circular gaussian beam of 18 arcsec, and all the points below a level of 3σ blanked. Spectral index maps were then derived using the COMB task which uses direct method of determing the spectral index between two maps : $\alpha = log\{S(\nu_1)/S(\nu_2)\}/log(\nu_1/\nu_2)$. Spectral index maps formed between 1272-616, 616-332, and 1272-332 MHz are shown in figures 4.10a, 4.10b and 4.10c respectively.

The total intensity maps of NGC 2997 at 332, 616 and 1272 MHz reveal many regions of intense radio emission across the disk of the galaxy. In regions, where there are strong features registered with position errors of the order of 3″ to 4″, one can make larger changes in the spectral index measurements. Therefore, we have also given flux densities, position and spectral index for each strong feature found in all the three maps, these values are mentioned in table 4.9. To obtain the position, peak and integrated intensity of each radio source, we used JMFIT task to fit a Gaussian-shaped component to strong features which are not too extended. When a source was clearly non-gaussian, its total flux density was computed by integration on the map together with the position of the centroid of its emission. The integrated flux densites quoted in table 4.9 have been normalized to the circular Gaussian beam of 18″ which, corresponds to a linear size of about 1.08 kpc. All discrete sources listed in the table 4.9 have the same positions in all the maps at our three observing frequencies, errors

Figure 4.10: Spectral index maps of NGC 2997

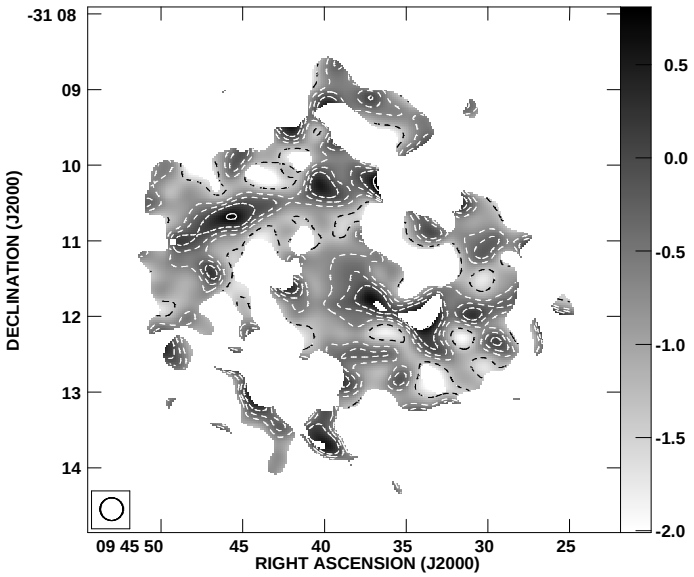

Fig. 4.10a : Spectral index map between 616 and 1272 MHz ($S_\nu \propto \nu^\alpha$). The greyscale is shown on the right side; the darker regions show relatively flat spectrum as compared to the ligher regions which represent steep spectrum and the Contours are at Levs= 4.800E-01× (-2.8, -1.4, -0.7, 0, 1.4).

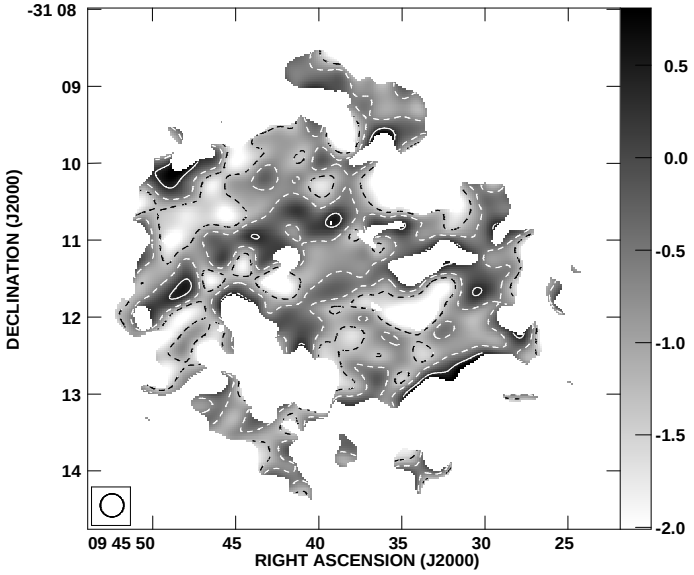

Fig. 4.10b : Spectral index map between 332 and 616 MHz ($S_\nu \propto \nu^\alpha$). Contours are at Levs= 5.4E-01 × (-2.4, -1.2, 0.6).

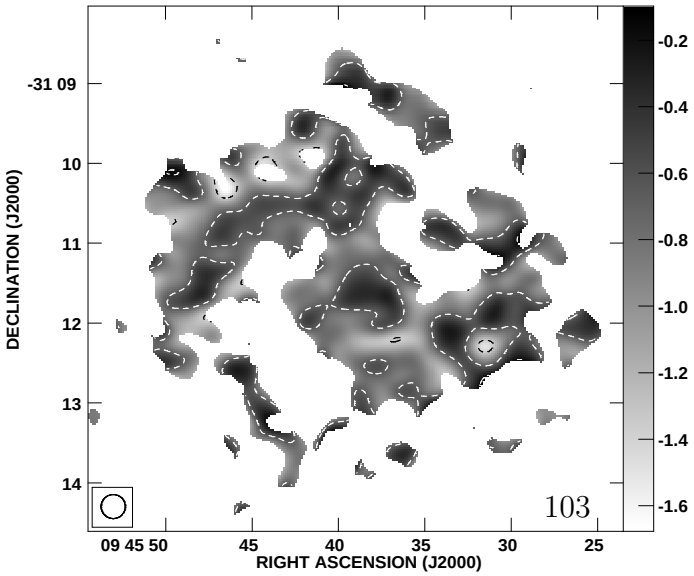

Fig. 4.10c : Spectral index map between 332 and 1272 MHz ($S_\nu \propto \nu^\alpha$). Contours are at Levs= 2.400E-01 × (-5.6, -2.80, -0.7,0).

in RA and DEC being less than $\pm 0.6^s$ and $\pm 5''$, respectively. The discrete Gaussian like components also show similar sizes in all the three frequency maps of similar spatial resolution. Sizes for some of the important components are given in table 4.9. The causes of position errors in one or two sources might be due to residual phase errors and noise plus confusions.

Interpretation : Spectral index maps in the figure 4.10 shows prominent flatter spectra in the northern arm region and steeper spectra in the outer region of the spiral arms (see fig 4.10-a,c). The low-frequency fitted spectra (332 MHz to 1272 MHz) have $-1.26 < \alpha < -0.65$ for all the discrete sources in the disk of the galaxy and these sources are listed in the table 4.9. The GMRT low-frequency spectra are shown in fig.4.11

NGC 2997 is known to be a "hot spot" galaxy (Meaburn & Terret 1982) with a number of UV luminous knots near the center, which are massive star-clusters. S.S Larsen et al. (1999) also detected plenty of young massive star-clusters (YMCs) in the center and outside of it. A single power law fit to the integrated flux densities on the central region of $0.5'$ in size (source 1), gives a spectral index of -0.65 (fig. 4.10c , 332-1272 MHz). The flatter values near the nucleus might be due to the comsic ray acceleration occuring in this region where particles are younger or due to thermal absorption by ionized gas in massive-star clusters which are known to be present in the central region. R. Martin, Perth Observatory, reports the discovery of an apparent supernova 2003JG located at RA= $9^h45^m37^s.91$; DEC= $-31°11'21''$ (J2000) which is almost close to the central part of the nucleus. But we did not find any clear indication of steeper spectral value in this region and the spectral index value of the central region between 332-610 MHz is -0.73. The spectral index value of source 1 is given in table 4.9 and is consistent with the measured mean spectral-index value from maps given in fig. 4.10 (by direct integration over the central region of $0.5'$).

Source 3 in ridge-component of the northern arm, is embeded in the giant HII region detected by V.Firpo et al.(2005) using high resolution spectra ($\lambda 3736 - 7136A°$). The core source in this region has been classified as a thermal source. Spectral index map in fig. 4.10a shows flatter spectra for the ridge component. In contrast, integrated flux densities of source 3 from our measurements given in table 4.9 suggest that it is nonthermal in nature with spectral index value $\alpha = -1.04$. Also, a single power law fit to the flux densities of the northern-arm ridge component shows characteristics of nonthermal emission. This characteristic is similar to the observation of the spiral galaxy M83 (S.Sukumar at al., 1987) at 327, 1465 and 4750 MHz. Also, the map of nonthermal continuum emission between $\lambda 21$ cm and $\lambda 6$ cm (H.Men & Han,2005) shows prominent nonthermal ridge-component in northern arm with the bright compact nonthermal source located at its centrepiece. Hence, our low-frequency spectra confirm the nonthermal emission nature of source 3 and ridge-component (source 3.a).

Source 6 in the southern arm shows unusually steep spectrum ($\alpha = -1.26$); high resolution GMRT images (fig.4.3-b and c) at 1272 MHz reveal that this source is elongated horizontally (East-West) which is 4.6 kpc by 2.16 kpc in size. We guess that there may be interaction of type II- supernova remnatnts with the ISM in this region to produce cosmic-rays.

The observed integrated flux densities over weak components which may not be perfect gaussian components can lead to wrong spectral index measurements. Instead of integrated flux densties over these components by JMFIT, we also calculated the spectral indices using the peak intensites at each source. It is found that peak intensity for source embeded in northern ridge-component (Source 3) show flat spectrum ($\alpha \approx -0.2$)at the GMRT observing bands. The spectral index value found on source 2 (northern bright source) also show flat spectrum ($\alpha \approx= -0.69$) towards low-frequency which is consitent with results obtained for spectral index using the observed flux densites. The spectral indices obtained using peak intensites for source 7 and nucleus is also consistent with result obtained using integrated flux density measurements. Source 6, and south-, north- west components (sources 4 and 5) have steeper spectra ($\alpha \approx -1.0$) towards low-frequency; this contradicts the spectral indices obtained using integrated flux densities over these components (see table 4.9).

Table 4.9: Some discrete sources in the disk of NGC 2997

Source	Observed position at 1272 MHz $\alpha_{2000} = h\,m\,s\ \pm s$ $\delta_{2000} = {}^\circ\ {}'\ {}''\ \pm''$	Integrated flux densities (mJy) & Peak intensities (mJy/beam) at 1272 MHz	616 MHz	332 MHz	Spectral index 332-1272 MHz	Comments
1	09 45 38.75 ±0.0 -31 11 26.66 ±0.3	51.9 ±1.7 21.2 ±0.5	75.8 ±4.2 29.6 ±1.2	125.1±5.1 41.7 ±1.3	-0.65 -0.50	Nuclear region of 1.8 kpc in size
2	09 45 39.62 ±0.1 -31 08 51.35 ±1.9	10.5 ±2.1 3.3 ±0.5	19.0 ±5.2 5.7 ±1.2	26.1 ±5.3 8.5 ±1.3	-0.69 -0.69	North source, 2.2 kpc by 1.6 kpc in size.
3	09 45 45.04 ±0.1 -31 10 32.88 ±1.0	18.1 ±1.8 6.3 ±.05	31.2 ±7 6.7 ±0.9	73.1 ±7 15 ±1.0	-1.04 -0.19	Nonthermal source in northern-arm
3.1	09 45 45.07 ±0.1 -31 10 33.41 ±1.0	70.3 ±5.8 4.9 ±.04	104.6 ±17 5.9 ±0.9	198.5±17 12.8 ±1.4	-0.77	Nonthermal northern ridge component (∼7.2 kpc by 2.7 kpc)
4	09 45 30.52 ±0.1 -31 10 55.39 ±2.6	15.2 ±2.7 3.4 ±0.5	33.2 ±8.2 5.7 ±1.2	43.4±7.1 9.6 ±1.3	-0.77 -0.76	North-west component, 2.4 by 2.04 kpc in size
5	09 45 31.18 ±0.1 -31 11 54.02 ±1.9	13.9 ±2.3 3.90 ±0.5	37.6 ±9.9 5.20 ±1.2	46.0±7.2 10 ±1.3	-0.80 -0.70	South-west coponent
6	09 45 37.37 ±0.2 -31 12 28.33 ±1.9	18.7 ±3.2 3.4 ±0.5	35.7 ±9.1 5.4 ±1.2	102.4±13 10.5 ±1.2	-1.26 -0.83	Source in southern arm, 4.6 by 2.16 kpc in size
7	09 45 48.90 ±0.2 -31 11 36.68 ±2.3	15.7 ±2.8 3.4 ±0.5	42.6 ±8.7 6.8 ±1.2	46.9±8.1 8.8 ±1.3	-0.81 -0.71	East component of North-east arm

4.3 Radio Sources in the Field of View

The size of primary field of view for the GMRT at 325, 610, and 1280 MHz is 1.5°, 0.7° and 0.44°, respectively. Besides NGC 2997 or NGC 4565, we have idendtified 10 to 35 other radio sources in the primary field of GMRT at each observing frequency (see fig.4.12 and 4.13). The positions and the flux densities for these sources are givn in table 4.10 and 4.11. We have also listed the flux densities of sources at 1.4 GHz by VLA (NVSS GRP) observations.

Table 4.10: NGC 2997 : Other Sources in the primary field of view at 325 MHz

Source	RA(2000) $h\,m\,s$	DEC(2000) $^\circ\ '\ ''$	$S_{325\ MHz}$ (mJy)	$S_{610\ MHz}$ (mJy)	$S_{1280\ MHz}$ (mJy)	$S_{1.4}$ (mJy)
(1)	(2)	(3)	(4)	(5)	(6)	(7)
1	9 45 35	-31 20 8	230.6 0.07	47.2 0.04	127.8 8.3	75.9 3.5
2	9 44 44	-31 19 12	68.3 0.06	47.2 0.04	51.2 7.6	23.2 3.7
3	9 44 40	-31 8 19	59.5 0.07	31.3 0.04	19.6 8.2	14.7 3.6
4	9 45 49	-31 6 15	115.3 0.08	64.9 0.05	33.8 9.6	35.7 3.7
5	9 46 15	-31 13 59	35.4 0.09	21.6 0.05	14.1 8.9	7.4 3.3
6	9 44 59	-31 13 47	17.9 0.06	7.7 0.03	5.2 6.8	
7	9 44 58	-31 9 59	9.4 0.06	3.4 0.03	4.7 7.9	
8	9 45 32	-30 57 51	477.6 0.06	302.1 0.04	192.1 7.5	210.6 3.5
9	9 44 46	-30 55 37	334.2 0.06	169.0 0.03	170.7 8.0	98.3 3.5
10	9 44 32	-30 58 46	35.1 0.06	23.3 0.03	25.3 7.3	22.8 3.5
11	9 45 49	-31 26 8	50.9 0.07	28.3 0.04	50.2 8.2	14.9 3.5
12	9 44 1	-30 52 40	564.3 0.07	233.5 0.03		
13	9 43 33	-30 51 54	180.6 0.06	104.9 0.04		
14	9 43 21	-30 59 1	49.5 0.06	33.6 0.04		
15	9 42 56	-31 17 40	563.2 0.07			
16	9 43 41	-31 26 1	159.3 0.07	103.4 0.04		
17	9 44 45	-31 24 21	68.8 0.32	29.9 0.07		
18	9 44 23	-31 34 52	16.0 0.05			
19	9 44 43	-31 40 41	606.1 0.08			
20	9 47 4	-31 8 51	21.8 0.07	9.5 0.04		
21	9 46 53	-31 5 15	13.8 0.06	17.8 0.06		
22	9 47 0	-31 3 16	152.8 0.08	81.9 0.05		
23	9 46 59	-31 2 1	55.7 0.06	39.8 0.04		
24	9 46 17	-30 54 6	113.1 0.10	86.8 0.07		
25	9 46 18	-30 50 47	38.0 0.07	34.4 0.04		
26	9 45 59	-30 48 5	10.7 0.05			
27	9 42 41	-31 34 3	151.8 0.08			
28	9 47 42	-31 31 42	81.0 0.07			
29	9 48 6	-31 32 4	55.5 0.07			
30	9 48 39	-31 37 7	316.7 0.09			
31	9 48 17	-31 6 38	22.7 0.06			
32	9 47 40	-30 56 54	43.0 0.09			
33	9 48 20	-30 50 0	44.0 0.07			
34	9 45 55	-30 36 10	57.4 0.06			
35	9 45 7	-30 31 44	109.0 0.07			

Table 4.11: NGC 4565 : Other sources in the primary field of view at 325 MHz

Source	RA(2000) $h\,m\,s$	DEC(2000) $^\circ\ '\ ''$	$S_{325\ MHz}$ (mJy)	$S_{610\ MHz}$ (mJy)	$S_{1280\ MHz}$ (mJy)	$S_{1.4}$ (mJy)
(1)	(2)	(3)	(4)	(5)	(6)	(7)
1	12 36 36	26 2 10	62.52 7.19	34.09 1.43	16.02 0.99	12.63 0.30
2	12 36 12	25 55 4	31.80 37.80	9.46 2.10	5.98 1.36	0.92 0.25
3	12 35 22	25 56 26	302.10 7.60	213.65 1.52	115.83 1.03	100.97 0.31
4	12 35 29	25 55 20	100.76 9.27	66.76 1.98	23.24 1.11	53.38 0.62
5	12 35 50	26 9 50	136.74 7.71	89.96 1.63	32.00 1.10	36.67 0.30
6	12 36 40	26 14 40	38.96 8.58	9.74 3.49		6.96 0.30
7	12 36 45	26 12 6	71.77 50.80	23.54 8.56	10.50 1.21	11.19 0.30
8	12 36 31	26 11 26	56.73 7.94	32.42 1.62	9.79 1.05	11.91 0.30
9	12 36 13	25 46 23	39.14 7.17	25.80 1.43	15.15 1.07	8.85 0.30
10	12 37 20	25 46 52	50.35 7.62	28.73 1.55		6.58 0.32
11	12 34 35	26 1 27	359.34 11.70	250.57 2.50		
12	12 34 15	26 6 21	77.54 8.78	61.11 1.57		
13	12 34 23	26 5 47	82.20 13.60	22.42 2.18		
14	12 37 34	26 18 38	83.68 12.60	52.67 2.58		
15	12 38 12	26 13 42	136.41 7.75	50.18 1.48		
16	12 38 6	26 7 32	170.12 7.91	91.00 1.51		
17	12 35 21	26 16 58	156.08 12.00	91.28 2.39		
18	12 36 1	25 33 49	107.93 8.13	62.75 1.45		
19	12 38 11	25 36 39	298.79 7.08			
20	12 33 37	26 10 43	287.77 11.40			
21	12 32 23	26 4 3	879.24 8.79			
22	12 32 25	26 8 36	1051.30 8.85			
23	12 32 9	26 13 35	178.90 7.99			
24	12 33 54	26 27 10	170.65 13.70			
25	12 34 4	26 38 21	312.38 16.60			
26	12 36 31	26 35 7	2666.40 9.87			
27	12 39 5	26 1 43	275.11 10.60			
28	12 36 52	25 7 53	1140.30 27.10			
29	12 40 10	25 55 1	233.89 20.20			
30	12 40 2	26 17 26	256.71 18.30			
31	12 38 25	26 33 34	315.05 21.20			
32	12 38 25	26 33 34	315.05 21.20			
33	12 35 43	26 46 40	186.31 19.10			
34	12 37 4	26 51 47	316.66 22.80			
35	12 37 14	24 57 58	2588.70 22.00			

Figure 4.11: The observed GMRT low-frequency radio spectra

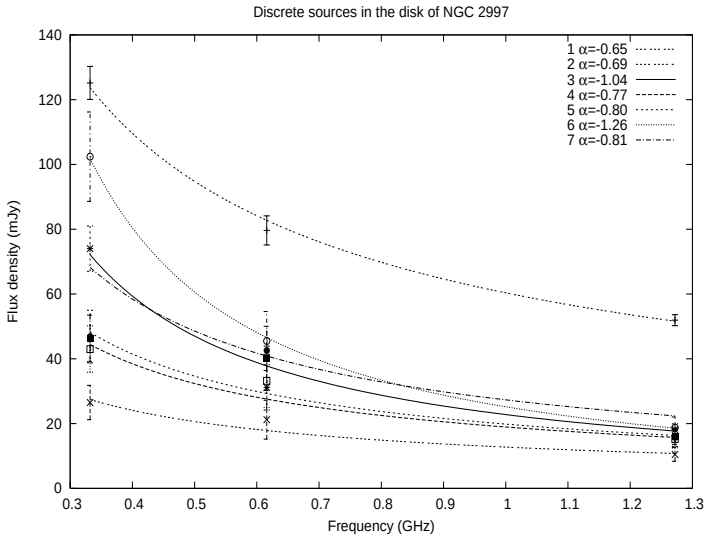

Figure 4.12: NGC 2997 : Other sources in the primary field of view at 325 MHz

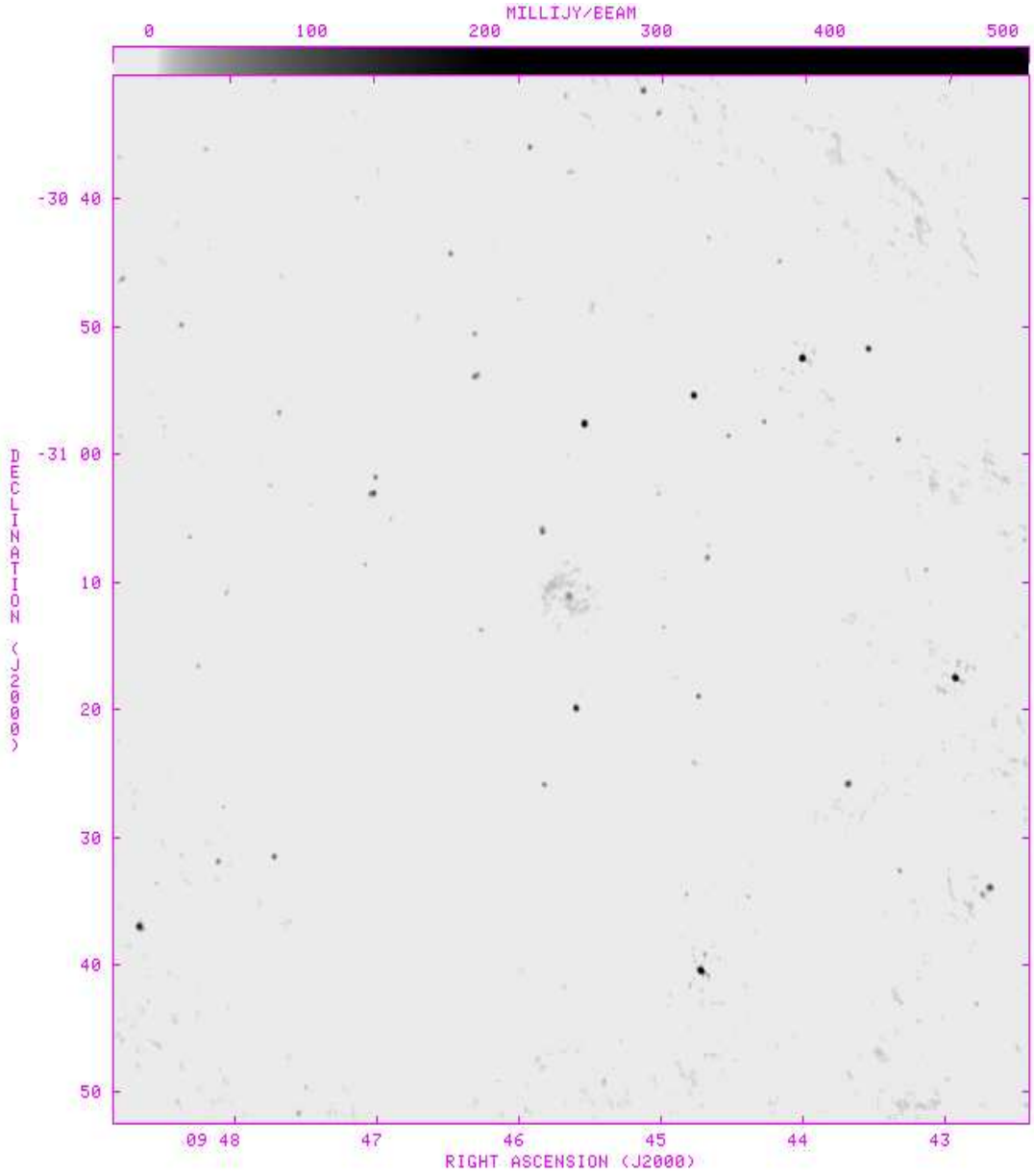

Figure 4.13: NGC 4565 : Other sources in the primary field of view at 325 MHz

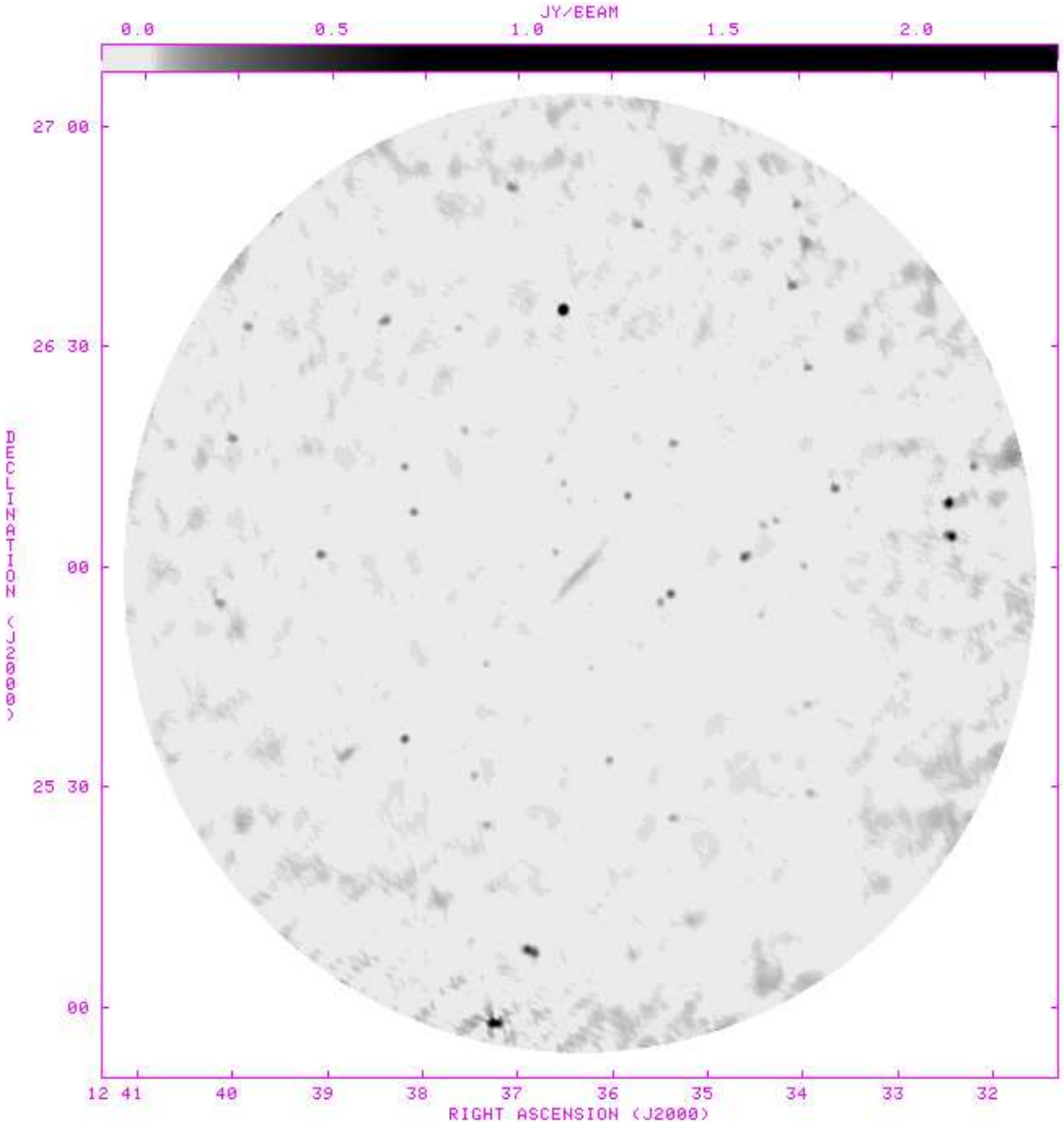

Chapter 5

Summary and Conclusions

In this thesis, we have presented the results of multi-frequency radio continuum observations of two nearby spiral galaxies NGC 2997 and NGC 4565 using the GMRT at three frequencies. This is the first time that NGC 2997 is being observed at low-frequencies i.e. 325, 610 and 1280 MHz. In the case of NGC 4565 higher resolution observations have been made at these frequencies for the first time. NGC 2997 and NGC 4565 are normal galaxies; in this work, we have described briefly, theory related to spiral galaxies, radio emission in such galaxies and their radio continuum structure. In the first half of the thesis, we have mainly adressed the observational details using the GMRT, describing the instrument from a radio continuum observation point of view, data reduction procedure followed using the AIPS and problems that occurred while imaging the low-surface brightness distribution of NGC 2997 and NGC 4565. We have studied the CLEAN and MEM deconvolution algorithms and their implementation in AIPS by mapping NGC 4565 at 610 MHz with a resolution of 12 arcsec. The image reconstructed by MEM is found to be smoother than the CLEAN. Most of the radio continuum features seen in the MEM image also appear in the CLEAN image, although both the methods use different deconvolution algorithms, showing high reliability of the derived images. While making the wide-field maps of NGC 2997 and NGC 4565 at low frequencies, we have discussed the non-coplanarity problem, and overview of possible solutions and the implemented method to reduce the *w-term* effect.

Our observational results give the total intensity maps of NGC 2997 and NGC 4565 over a variety of spatial resolutions. NGC 2997 maps with spatial resolutions of $8''$, $29''$, and $15''$ at each observing frequency reveal many radio continuum features. Also, the spectral index distribution maps obtained using the smoothed maps at a common resolution (18 arcsec) reveal the radio emission nature for several sources across the disk of the galaxy. Conclusions on NGC 2997 from our observations are summarized as follows :

(1) The radio emission distribution in the low-resolution image at each observing band covers an area of emission of about $\sim 6.5' \times 8.1'$.

(2) All total intensity maps show compact bright nucleus of less than 1.8 kpc ($0.5'$) in size, centered at, $\alpha_{2000} = 09^h45^m38.8^s$, $\delta_{2000} = -31°11'27''$. This position is consistent with the values given by de Vaucouleurs et al.(1991), Han (1999) and H.Men & Han

(2000). From the measured flux densites over a central region of $0.5'$ and from the spectral index distribution maps, the central region of NGC 2997 shows a flat spectrum at low-frequencies. The flatter values near the nucleus could be explained by considering that the young cosmic ray particles get accelerated in this region (Irwin et al.,2003) or that, thermal absorption by ionized gas occurs in massive-star clusters which are known to be present in the central region (Larsen et al. 1999).
(3) The radio continuum emission from the two spial arms were detected clearly and the structure of the spiral arm show Sc classification. The 610 MHz and 1280 MHz radio contour maps (fig. 4.2b & 4.3a) superimposed onto the optical image show the bifurcation feature of the southern arm into the third arm towards the west direction.
(4) All the total intensity maps of NGC 2997 show a gap of radio emission near the region $\alpha_{2000} = 09^h45^m32.8^s$, $\delta_{2000} = -31°10'$. This region in the optical image appears to be blue, possibly suggesting that there is an abscence of star-forming region or that the blue light is from the hottest stars. This gap is also seen in the VLA total intensity and polarized intensity maps at λ20 cm, λ18 cm, λ6 cm, and λ3 cm. (Han,1999; H.Men & Han,2005).
(5) The total intensity maps show a bright compact source towards the north of the galaxy ($\alpha_{2000} = 09^h45^m39.9^s$, $\delta_{2000} = -31°08'50.0''$). The optical counter-part of this source is absent in the optical image. The low-frequency spectrum from the observed flux densites for this source is found to be flatter towards 325 MHz.
(6) We found a bright compact source embeded in the ridge-component of the northern spiral arm which is located at the same position of the giant HII region detected by V. Firpo et al(2005). The spectral index value obtained from the observed flux densities suggests that emission from this source is nonthermal. This characteristic is similar to the observation of M83 spiral galaxy (S.Sukumar et al.,1987) at 327, 1465, and 4750 MHz. Also, a map of nonthermal continuum emission between λ21 cm and λ6 cm (H.Men & Han,2005) shows prominent nonthermal ridge component in the northern arm with the bright compact nonthermal emission source embeded in it. Hence, our low-frequency spectra confirm the nonthermal nature of the source embeded in the ridge component of the northern spiral arm.

The total intensity maps of NGC 4565 at each observing frequency are given in two sets. One of these set contains low resolution maps of $45''$ at three frequencies, and another set contains maps with a higher resolution of $20''$. The summary of the results obtained from our observations of NGC 4565 is given below :
(1) The low resolution total intensity maps overlaied on the optical image at 325 MHz and 610 MHz show mainly two components of radio emission distribution, one component concentrated along the principal plane of the galaxy representing the thin-disk and another smooth extended component parallel to the major-axis represeting emission from the thick disk. Low resolution maps at 325 MHz and 610 MHz show two sources along the major axis, one being the central source extending towards the south-west half of the galaxy and another source situated at a distance of $\sim 1.7'$ from the center of the galaxy.
(2) A dip has been observed between these two peak sources which is also seen in the high resolution map. The spectral index distribution between 325 MHz and 610

MHz along the major-axis using the high resolution maps shows that dip has a flat spectrum value $\alpha \approx -0.5$.
(3) The distribution of radio emission in the 325 MHz low-resolution map (fig. 4.6c) shows prominent deviation from the principal plane at the north-west end of the galaxy. This kind of warp has also been observed at 1410 MHz of WSRT (E. Hummel et al., 1984).
(4) The radio dimensions (FWHM) of NGC 4565 using the high resolution maps are found to be $\sim 395'' \times 37.7''$ and $370'' \times 37.9''$ at 325 MHz and 610 MHz respectively. These values are close to the radio dimensions (FWHM) measured at 1414 MHz (Broeils et al., 1985).
(5) Our high resolution maps (see fig.4.6) resolved the central extended source into three components reliably. The spectral index distribution shows that the central source 'A' and th source 'C' have flatter spectral indices at low frequencies. The spectral index distribution for source 'B' clearly indicates its nonthermal nature with a spectral index value around ~ -0.8.
(6) We identified two steep spectum sources ($\alpha \approx -1.0$) in the north-east side of the map and one southern source which has a flat spectrum ($\alpha \approx -0.3$).

We studied the global radio continuum properties of NGC 2997 and NGC 4565 which were given in table 4.2 and 4.5, respectively. The spectral power (in the units of $10^{21} W\, Hz^{-1}$) at our observing frequencies from 1280 MHz to 325 MHz are in the range of 6 to 18.5 for NGC 2997 and 1.5 to 8.5 for NGC 4565. It is found that NGC 2997 shows higher luminosity values than NGC 4565 The measured q parameter (logarithmic measure of the FIR/radio flux density ratio, Condon, 1992) for NGC 2997 at 1.272 GHz is 2.18. The $\hat{q}_{FIR}$ measured in the frequency bands 325 MHz and 610 MHz for NGC 2997 and NGC 4565 are found to be 2.19 and 2.37 respectively. These values are consistent with the average value of q for spiral galaxies at 1.4 GHz : $\langle q \rangle \approx 2.3 \pm 0.2$. The measured spectral power and FIR/radio flux density ratio of NGC2997 and NGC 4565 at our observing frequencies confirms that these are normal spiral galaxies.

We fitted a composite (thermal free-free plus synchrotron) as well as a single power law model to the total emission flux densities of NGC 2997 and NGC 4565 in the range of 10.5 GHz to 325 MHz. The best-fit value obtained from the single power-law model is $\alpha = -0.98 \pm 0.06$. In our case, the composite spectra did not fit properly for the NGC 2997 data. Using the observed total flux densities only in the GMRT bands, a simple non-thermal spectral index fit gives a value of $\alpha_{nt} = -0.80 \pm 0.07$. The composite spectra model is best fitted to NGC 4565 with the nonthermal spectral index $\alpha_{nt} = -1.19 \pm 0.16$. The non-thermal spectral index values obtained for NGC 2997 and NGC 4565 are steeper than the mean value $\langle \alpha_{nt} \rangle = -0.83 \pm 0.02$ obtained for a sample of 74 galaxies by Niklas et al.(1997). However, the values obtained by Hummel et al.(1985) and Dumke et al.(1988) are -0.93 ± 0.08 and -0.965 ± 0.002, respectively.
Using Condon & Yin equation (1990) and the spectral index value obtained from the GMRT total flux densities (see equation 1.6) the derived thermal fraction for NGC

2997 at 1272, 616, and 332 MHz is 10.33%, 6.08% and 3.58%, repectively, of the observed total flux density value. The thermal fraction of (S_{th}/S) 10.33% at 1272 MHz is found to be consistent with the upper limit set for the thermal fraction of normal spiral galaxies at 1.4 GHz (Condon, 1992). We have obtained flux density very similar flux density values (of about 40 mJy) for the thermal fraction in all our three observing bands. By fitting the composite spectral model to the NGC 4565 radio spectrum, we derived the thermal and nonthermal flux density, thermal fraction and the ratio of thermal to synchrotron flux density at each frequency (see table 4.7). Also, we estimated the thermal fraction at each frequency using the equation by Condon & Yin, 1990. The thermal fraction (S_{th}/S or T/(T+N)) for NGC 4565 at 1.4 GHz was found to be around 0.14.

Assuming that the observed flux densities are of non-thermal origin, the derived non-thermal luminosities for NGC 2997 and NGC 4565 were used to estimate the supernovae rate (yr^{-1}), the average star-formation rate ($SFR(M \gtrsim 5M_{\odot})$ and the production rate of the Lyman continuum photons (s^{-1}). These estimated parameters are given in table 4.8. The radio supernova rate for our Galaxy is 0.013 yr^{-1} (CasWell & Lerche, 1979) and Type-II supernova rate estimated by Tammann (1982) is $\nu_{SN} \sim 0.023\, yr^{-1}$. The radio supernova rate in NGC 4565 estimated by us to be $0.016\, yr^{-1}$ which is close to the values for our Galaxy. Our data suggest that the ν_{SN} in NGC 2997 is a factor of three to four times higher than that of our Galaxy. Lymann continuum photon production rate in NGC 4565 ($1.36 \times 10^{53}\, s^{-1}$) is 30% less than that of our Galaxy ($2 \times 10^{53}\, s^{-1}$). The derived star-formation rate in NGC 2997 and NGC 4565 suggest that these are normal galaxies with intermediate star-formation (SF) levels.

Han et al. (1999) made deep radio polarization observations of the NGC 2997 at λ18 cm, λ cm, and λ3 cm; their observation at λ20 cm could not detect polarization in NGC 2997. Their polarization observation revealed a regular spiral field in the central part (galactic radius R $\lesssim 0.5'$) of the galaxy. Dominating component of the linearly polarized emission is located at the *inner edge* of the optical spiral arms in the inner disk ($\lesssim 1.5'$). The vectors are well-aligned parallel to the spiral arms. Two magenetic spiral arms in the southeastern and northwestern parts of the outer disk detected clearly in their observation. S. Sukumar et al.(1991) observed the distribution of intensity and linear polarization of the two edge-on galaxies NGC 891 at λ6 cm and NGC 4565 at λ20 cm with a resolution of $20''$. They found that the polarized distribution is nearly symmetric in Z about the major axis for both the galaxies; a strong asymmetry is found about the minor axis of NGC 4565 where the polarized emission at 20 cm appears moslty on the east side of the nucleus.

The *polar mode* of GMRT has been released under the test mode recently, hence debugging and propoer calibration for the instrumental polarization of the GMRT antennas are required in order to detect linearly polarized emission from the observed galaxies described in this thesis.

Bibliography

[1] *A 1.49 GHz Atlas of Spiral Galaxies with $B_t < +12$ & declination ≤ -45 degree -J.J Condon*

The Astrophysical Journal Supplement Series,65:485-541,1987 December

[2] *Magnetic fields in the spiral galaxy NGC 2997*

J.L Han et al. [Astron. Astrophys. 348, 405-417 (1999)]

[3] *Images at 20cm and the Spectrum Index of NGC 2997*

Hui Men and Jin-Lin Han [Chin. J. Astron. Astrophys. Vol.5 (2005), No.1,49-56]

[4] *The spatial correlation between far-infrared and radio emission in galaxies - I. NGC 6946,M51,NGC 2997 and M83*

A.J.Fitt et al. [Mon. Not. R.astr. Soc.(1992)255,146-164]

[5] *New giant HII regions in the southern sky*

V.Firpo et al. [Mon. Not. R.astr. Soc.(2005)356,1357-1361]

[6] *Radio continuum observations of the edge-on spiral galaxies NGC 4244,4565 and 5907*

E.Hummel, R. Sancisi, and R.D. Ekers [Astron.Astrophys. 133,1-10 (1984)]

[7] *The "thick" radio disk of NGC 4565*

A.H.Broeils and R.Sancisi [Astron.Astrophys. 153,281-283 (1985)]

[8] *Polarized radio emission at 2.8cm from a selected sample of edge-on galaxies*

M. Dumke et al [Astron.Astrophys. 302,691-703 (1995)]

[9] *Polarized radio emission from the edge-on spiral galaxies NGC 891 and NGC 4565*

S.Sukumar and R.J. Allen [The Astrophysical Journal,382:100-107(1991,Nov.20)]

[10] *IRAS observations of three edge-on galaxies*

R.J. Wainscoat et al. [Astron. Astrophys. 181,225-236(1987)]

[11] *Radio Emission From Normal Galaxies*

J.J.Condon [Annu. Rev. Astron.Astrophys.1992.30:575-611]

[12] *Gaseous Halos of Late-Type Spiral Galaxies*

Michael Dahlem [Pub. of the Astronomical Society of the Pacific. 109,1298-1320(1997,Dec.)]

[13] *The Radio Continuum Morphology of Spiral Galaxies*
P.C. van der Kruit and R.J. Allen [Annual Review Inc.(1976ARA&A..14..417V)]

[14] *The Large-Scale Radio Continuum Structers of Spiral Galxies*
P.C. van der Kruit [1978IAUS...77...33V]

[15] *High frequency radio continuum investigation of M51*
C.Klein et al.[Astron.Astrophys.135,213-224(1984)]

[16] *Radio Observations of complete sample of spiral galaxies at 408 MHz*
M.GIOIA & L. GREGORINI [A & A Suppl. Ser 41,329-334 (1980)]

[17] *Radio Continuum Observations of the Edge-on Disk Galaxy NGC891*
R.J. Allen,J.E. Baldwin and R.Sancisi, Astron.Astrophys.62,397-409(1978)

[18] *The large-scale radio continuum structure of the Edge-on Spiral galaxy NGC 891*
E.Hummel,M.Dahlem,J.M.van der hulst, and S.Sukumar, Astron.Astrophys. 246,10-20(1991)

[19] *Multi-Frequency radio continuum observations of NGC 5236 (M83)*
S.Sukumar,U.klein, and R.Grave [Astron.Astrophys.184,71-78 (1987)]

[20] *GMRT Observations of NGC 3079*
Judith A. Irwin and D.J. Saikia. MNRAS,Sept.2003

[21] *The separation of synchrotron and bremsstrahlunng radio emission in spiral galaxies*
Nerojsa Duric et al., 1988AJ

[22] *Giant metrewave radio telescope (GMRT) – Scientific objectives and design aspects*
Swarup, et al. [Current Science, 1990]

[23] *Multi Colour Universe, eds B. Paul & R. Manchanda*
Ananthakrishnan S., Rao, A.P., 2002 [TIFR, India, p.223]

[24] *Online computer system of GMRT (Internal tech. report)*
C.R. Subramaniyam , Aug, 1990

[25] *Overview of the GMRT Online Computer System (Internal tech. report)*
A. Pramesh Rao , Dec 12^{th}, 1991

[26] *Astronomical Calibration of the GMRT Antenna Positions (Internal tech. report)*
Jayaram N. Chengalur & Sanjay Bhatnagar, Jan 15^{th}, 2001

[27] *Computation of Antenna Dependent Complex Gains (Internal tech. report)*
Sanjay Bhatnagar, 1999

[28] *J2000 co-ordinates in GMRT UV FITS Files (Internal tech. report)*
Jayaram N. Chengalur, Mar 27^{th}, 2003

[29] *Interferance and Cohernce theory*
B.G. Clark, NRAO (Scientific memorandum)

[30] *Radio interferometry and Synthesis Imaging*
T.S. Bastin, NRAO (Scientific memorandum)

[31] *Lecture Notes in Physics '353' (Evolution of galaxies, astronomical observation)*
Appenzellar, H.J. Habing, et al.

[32] *Radio Study of Galactic Supernova Remnants and the Interstellar Medium*
Sanjay Bhatnagar, (Ph.D. thesis, July 2001)

[33] *Low Frequency Radio Astronomy, Course Notes from a School, NCRA, 1999*
eds by Jayaram N. Chengalur, Yashwant Gupta, K.S. Dwarakanath, May 26^{th} ,2003

[34] *VLBI techniques and applications*
Felli and Ralph E. Spencer

[35] *Synthesis Imaging, Course Notes from an NRAO Summer School*
eds by Richard A. Perley, Fredric R. Schwab and Alan H. Bridle, Auguest, 1985